

Development of Graphene Oxide Membranes for Pervaporative Desalination

by

Mursal Ashrafi

A thesis
presented to the University of Waterloo
in fulfillment of the
thesis requirement for the degree of
Master of Applied Science
in
Chemical Engineering (Nanotechnology)

Waterloo, Ontario, Canada, 2018

© Mursal Ashrafi 2018

Author's Declaration

I hereby declare that I am the sole author of this thesis. This is a true copy of the thesis, including any required final revisions, as accepted by my examiners.

I understand that my thesis may be made electronically available to the public.

Abstract

Fresh water scarcity is quickly becoming a serious global challenge as populations grow and resources are depleted. Seawater, which makes up 97% of the water on Earth, can be a viable and sustainable source of usable water if energy-efficient, scalable, and cost-effective methods for desalination can be found. Based on molecular dynamic simulations, graphene-based materials used as desalination membranes can achieve nearly perfect salt rejection while maintaining orders of magnitude higher permeability than current commercial membranes. A new membrane-based separation technique called pervaporation (PV) has fundamental advantages over reverse osmosis (RO) and has potential to become a more energy-efficient technique compared to RO. In our work, we integrate graphene-based membranes with the PV technique for a scalable and high-performance desalination system.

Membranes based on graphene oxide (GO) are promising as a starting material for desalination membranes due to their scalable production, relative ease of processing and their multi-functional surface chemistry which can be beneficial for cross-linking and functionalizing the atomically thin sheets. Due to their unique structure of hydrophilic and hydrophobic domains, they are capable of selective water transport when stacked on top of each other to form thin or thick films.

In order to further enable the large-scale processing of GO into thin membranes, it is imperative to find solvents that meet the manufacturing requirements of high volatility and low toxicity which can also chemically and colloidally stabilize single layer dispersions. To this end, we study GO dispersions in a system of 1-alcohols in comparison to that of water which is conventionally used as a solvent. In this thesis, several unique phenomena are demonstrated that make a subset of these solvents ideal for processing and explore the benefits of casting membranes from these solvent systems using a variety of techniques for application in PV desalination.

In the first experimental chapter, the chemical and colloidal stability of GO was compared in both aqueous solvents and a series of 1-alcohols. The colloidal stability of these alcohol dispersions varies greatly compared to aqueous dispersion. As demonstrated by other groups, GO in water undergoes gelation around 1 wt% due to the strong electrostatic interaction between GO and water molecules, making it difficult to process. This does not occur in the alcohols, enabling us to achieve high dispersion concentrations of up to 8 wt%. This property was studied by simple centrifugation testing,

where GO was seen to settle more easily in the alcoholic media. Despite settling, we were able to show with AFM imaging that GO can maintain an exfoliated state of mostly single layers in all the 1-alcohols. We also confirmed liquid crystalline (LC) properties in all alcohol dispersions with the help of polarized light microscopy, which has shown to be useful in making better-performing GO architectures compared to the conventional non-LC GO.

In addition to the processing advantages, alcohol dispersions also have chemical advantages. In aqueous media, GO is known to continuously undergo chemical transformation due to water's nucleophilic nature. This chemical transformation causes a color change from yellow to dark brown, which suggests a more reduced nature of the material. This color change was observed to be inevitable in the aqueous dispersion but was accelerated in the alcohol dispersions when exposed to light. By quantifying these changes with UV-vis and FTIR spectroscopy, we study the evolution of the absorption coefficient of these dispersions at 230 nm, which is associated with the electronic transition of C=C bonds, and FTIR peaks at 1220 cm⁻¹ (C-O-C), 1300 cm⁻¹ and 1500 cm⁻¹, the latter two associated with carbon-carbon bonds. The absorption coefficient of aqueous GO dispersion at 230 nm was much higher than the alcohols, and it continues to increase with time regardless of conditions. However, all alcohol dispersions demonstrate a resistance to chemical transformation when stocks were sealed, but hexanol demonstrates resistance to chemical transformation even when the stock was continuously used. FTIR spectroscopy was used to support the chemical transformations indicated by UV-vis, suggesting loss of oxygen functionality and more carbon-carbon bonds as the dispersions were exposed to light. The trend with FTIR also suggested that hexanol provides some resistance to chemical transformation induced by light exposure while the other alcohols do not as much. Based on our AFM analysis, the flake sizes were much smaller in the water system compared to the alcohols. All these results indicate that GO in water undergoes chemical and physical changes, which may not be ideal for various applications that require a high oxygen functionality and larger flake sizes. This also suggests that GO is sensitive to light and should be stored away from light to lengthen lifetime.

Finally, we used the various dispersions to prepare vacuum-filtered GO membranes and compared the performance in PV desalination. We developed a custom-made PV module that required optimization of all components, including membrane module, fluid flow dynamics, condenser design, vacuum level, and permeate collection. We compared the performance of the system with a

commercial membrane and a commercial PV module, and observed a 5% difference, which we deemed acceptable.

Our data indicated that properties of the vacuum-filtered membranes differed based on the solvent. First off, the interlayer distance depended on the type of solvent, which ranged from 9 to 11 Å. Using the native GO membranes resulted in swelling and leakage, which was mitigated with a zinc crosslinking to enhance the mechanical properties of the membrane. Even with this zinc-enhancement, the water-based membranes were failing with more than a 50% failure rate, compared to the alcohols that were around 20%. To sum up, there were no conclusive differences between the flux and rejection of the different solvent systems, however the 1-propanol and 1-butanol consistently performed better. We also observed a big improvement in flux with more hydrophilic and more porous support membranes. When testing the membranes at a 3.5 wt% NaCl feed solution at 30 °C, we observed a flux of 18.6 L/m²h and >99.8% with the GO membrane from 1-propanol at a loading of 40 µg/cm², where the previous work done by another group achieved a flux of 14.3 L/m²h at the same loading. This improved performance may be due to a combination of effects of zinc enhancement, an optimal interlayer distance and using a better support membrane.

In addition to the work in the application of PV, we tested the capabilities of GO dispersions in 1-alcohols in other membrane preparation techniques, namely solution casting and Langmuir-Blodgett (LB) deposition. Here, we demonstrated successfully that we were able to achieve high-crystallinity GO membranes from 1-alcohol dispersions. We also demonstrate the use of these 1-alcohols dispersions for the high yield transfer of GO monolayers as LB films. Together, these novel methods can yield an inexpensive, reproducible, and most importantly scalable process for creating high performance graphene-based desalination membranes.

Acknowledgements

My sincerest appreciation goes to my supervisor, Dr. Michael Pope, for allowing me into his group as a Master's student and mentoring me. Thank you for my guiding me through the challenges and celebrating my victories, however small. Your guidance has been so valuable and has shaped me into a better researcher and a better person.

I would also like to acknowledge the wonderful group of researchers that I worked with during my time in the Pope group. Every one of you has contributed to my work with your advice and moral support. In particular, I want to thank Amanda Xu, Dilara Yilman Lenos, Irene Lau, and Gillian Hawes for their friendship and guidance especially during the difficult times.

I am especially grateful to Khalfan Almarzooqi for sharing ideas, providing valuable insight, and being a resource. Thank you for all your help with calibrating the PV module with me and running some of my experiments. I would also like to thank the undergrad facility for letting me use their equipment and to Elnaz for helping me with understanding PV better.

Thank you to Latifa and Zohlnar for always cheering me up with your silly jokes and delightful hugs. You two have been a constant ray of happiness in my life.

Finally, I would like to thank my family, especially my dad and my sisters for always believing in me and for making this possible. I would not be who I am or where I am without your struggle and dedication to make a better life for us. Last but certainly not least, I want to thank Ali for his unwavering love and support throughout my undergraduate and master's studies. Thank you for always being a pillar of strength in my life.

Dedication

Dedicated to my dad, for his endless love, support, and encouragement

Table of Contents

Author's Declaration.....	ii
Abstract.....	iii
Acknowledgements.....	vi
Dedication	vii
Table of Contents.....	viii
List of Figures	xi
List of Tables	xvi
List of Abbreviations	xvii
1 Introduction	1
1.1 Water Scarcity	1
1.1.1 Desalination Technologies	2
1.1.2 Membrane Materials for Desalination	5
1.1.3 Graphene Oxide Dispersions	6
1.2 Motivation for the Project	7
1.2.1 Objectives	8
1.3 Organization of Thesis.....	8
2 Background	10
2.1 Fundamentals of Pervaporation.....	10
2.1.1 Pore Flow Model	11
2.1.2 Solution-Diffusion Model	13
2.1.3 Transport Across Graphene Oxide	15
2.2 Membrane Materials	16
2.2.1 Graphene Oxide Membranes.....	19
2.3 Graphene Oxide Dispersions.....	22
3 Graphene Oxide Dispersions.....	26
3.1 Motivation	26

3.1.1	Objectives	27
3.2	Experimental Design	27
3.2.1	Graphene Oxide Synthesis	27
3.2.2	Graphene Oxide Colloidal Stability	28
3.2.3	Solvent-Dependent Chemical Transformation of Graphene Oxide.....	31
3.3	Results and Discussion.....	34
3.3.1	Solution Processibility of Graphene Oxide Aqueous and 1-Alcohols Media.....	34
3.3.2	Graphene Oxide Colloidal Stability	35
3.3.2.1	Liquid Crystalline Graphene Oxide	37
3.3.3	Solvent-Dependent Chemical Transformation of Graphene Oxide.....	42
3.3.3.1	UV-Vis Analysis of Graphene Oxide Dispersions.....	43
3.3.3.2	FTIR Analysis of Graphene Oxide Dispersions.....	46
3.3.3.3	Study of Other Aspects of Graphene Oxide Dispersions.....	48
3.3.4	GO Aging Model.....	52
3.4	Conclusions.....	53
4	PV Module and Membrane Design.....	54
4.1	Introduction.....	54
4.2	Pervaporation Module Optimization	55
4.2.1	Iterations of the Membrane Module.....	55
4.2.2	Permeate Collection Optimization.....	62
4.2.3	Peripheral Components Optimization	67
4.3	Graphene Oxide Membranes	67
4.4	Conclusions.....	76
5	Expanding on Graphene Oxide Membrane Preparation	78
5.1	Solution Casting.....	78
5.2	GO Cast Membranes.....	78

5.2.1	Low-Temperature Reduction.....	80
5.2.2	High-Temperature Reduction.....	83
5.3	Langmuir-Blodgett Monolayers	86
5.3.1	LB Deposition.....	87
5.3.2	Extending LB Depositions to Polymeric Substrates.....	91
5.4	Conclusions.....	93
6	Conclusions and Future Work	95
6.1	Summary of Main Findings	95
6.2	Recommendations for Future Work	96
7	References	97

List of Figures

Figure 1.1: Water scarcity indices in countries around the world from 2004. Color scale indicator for level of water stress [4].	1
Figure 1.2: Breakdown of desalination technologies into two categories: thermal-based desalination (left branch) and membrane-based desalination (right branch).....	2
Figure 1.3: RO efficiency over the last four decades [2], [3]. The dashed line marks the thermodynamic minimum.....	3
Figure 1.4: Scheme of PV process, where membrane module is connected to the feed on one side and condenser and vacuum on the other side [16].	4
Figure 1.5: a) NPG membrane, b) stacked GO multilayer membrane, c) GO microstructure, including the interlayer gallery, surface pores, edges and wrinkles [24], [25].....	5
Figure 2.1: Schematic diagram of PV module [48].....	10
Figure 2.2: a) The principle of pore flow model, showing a flow across a membrane pore, and b) schematic of the driving force profiles across the membrane layer [50, 51].	11
Figure 2.3: The principle of solution-diffusion model, showing an asymmetric membrane with a dense barrier layer [18], and b) schematic of the driving force profiles inside the dense barrier layer [50]. ..	13
Figure 2.4: Illustration of water transport mechanism across GO nanochannels in PV mode [56]... <td>16</td>	16
Figure 2.5: a-b) Isotropic membranes made from a) phase inversion, and b) extrusion and stretching. c-d) Anisotropic membranes with c) uniform composition and non-uniform morphology, and b) non-uniform composition and morphology.....	17
Figure 2.6: Range of nominal pore sizes based on membrane technologies [50].	18
Figure 2.7: Lerf-Klinowski GO structural model [62].	19
Figure 2.8: Schematic illustration of water flow models between a) pristine graphene sheets, b) GO sheets, and c) GO flakes that are composed of both pristine graphene and oxidized channels [25].	20
Figure 2.9: Summary of PV desalination studies with polymeric, ceramic, and graphene oxide membranes, presenting water flux vs. salt rejection.....	22
Figure 2.10: Schematic of reaction between graphite oxide and water, to show the compositional change that occurs as a result of water exposure [64].	23
Figure 2.11: Interaction energy between two parallel GO sheets in different solvents in the absence of electrostatic forces but presence of solvation forces [75].....	24
Figure 3.1: Zeta potential cells for a) aqueous media and b) organic solvents [82].....	29

Figure 3.2: a) Schematic depiction of formation of highly aligned 2D platelet structures as a function of increasing concentration [62]. b) Graphene oxide liquid crystal phase diagram: transition from isotropic to nematic is strongly dependent on dispersion concentration and aspect ratio of GO flakes [84].	30
Figure 3.3: a) Custom-made polarized light imaging setup with cross-axis polarizers. Graphene oxide dispersion in 1-butanol b) without polarizers and c) with polarizers. Direction of cross-polarizers axes marked by the arrows.	30
Figure 3.4: a) Variation of I_D/I_G ratio with respect to L_a , and b) schematic depiction of influences on Raman spectra [86].	33
Figure 3.5: Graphene oxide dispersions in respective solvents a) before and b) after centrifugation at 3500 rpm for 30 minutes. Solvents (left to right): water, ethanol, 1-propanol, 1-butanol, 1-hexanol.	34
Figure 3.6: Colloidal stability depicted at a) 0.01 wt% and b) 0.05 wt%. Solvents (left to right): water, ethanol, 1-propanol, 1-butanol, 1-hexanol.	36
Figure 3.7: Aggregation of graphene oxide in water a) in dispersion and b) in dried state under optical microscope.	37
Figure 3.8: Observation of liquid crystalline phases in water and 1-alcohols as a function of concentration under cross-polarizers. Direction of cross-polarizers axes marked by the arrows.	38
Figure 3.9: Observation of liquid crystalline phases in 1-hexanol with a) some settling and b) after mild shaking. Cross-polarizers axes marked by the arrows.	39
Figure 3.10: a) Spray dried graphene oxide dispersed in ethanol (tip sonicated for 15 minutes), dispersion b) without cross-polarizers, and c) with cross-polarizers. Direction of cross-polarizers axes marked by the arrows.	40
Figure 3.11: AFM micrographs of graphene oxide flakes from different solvent systems spin-coated on Si wafers: a) water, b) ethanol, c) 1-propanol, d) 1-butanol, e) 1-hexanol, and f) spray-dried graphene oxide.	41
Figure 3.12: a,c,e) Graphene oxide dispersions in water and 1-alcohols at t=0. b) Dispersions at t=2 months, covered in aluminum foil to avoid light exposure, d) dispersions at t=2 weeks, under direct lamp light, f) dispersions at t=10 months, slight exposure to light (i.e. on the shelf in a box without aluminum foil). Solvents (left to right): water, ethanol, 1-propanol, 1-butanol, 1-hexanol.	42
Figure 3.13: UV-Vis spectrum of modified Hummer's graphene oxide.	43

Figure 3.14: a) Absorbance vs. wavelength spectra of graphene oxide in ethanol at varying concentrations, b) absorbance values at 230 nm with respect to concentration, the slope is the absorption coefficient.....	44
Figure 3.15: a) UV-Vis spectra of graphene oxide in water and 1-alcohols, and b) calculated absorption coefficients of sealed and continuously used stocks.....	45
Figure 3.16: a) Full IR spectrum of fresh GO in water, and b) zoomed-in ($2000 - 1000 \text{ cm}^{-1}$) spectra of fresh GO from water and 1-alcohols systems.....	46
Figure 3.17: FTIR spectra of a) 10-months-old sealed dispersions b) 2-weeks-old dispersions under direct light exposure.....	47
Figure 3.18: Peak ratios of graphene oxide dispersions in three different states: i) fresh, ii) sealed (for 10 months) and iii) light exposure (for 2 weeks).	47
Figure 3.19: Raman spectra of GO-butanol system with I_D/I_G ratios calculated using a) peak heights, and b) using a two-gaussian fit	49
Figure 3.20: Thermal analysis of all solvents with a) weight loss and b) rate of weight loss, with respect to temperature.....	50
Figure 3.21: XRD diffractograms of a) peak evolution of GO-ethanol slurry with respect to time, and b) interlayer spacing of dried GO from respective solvent dispersions.....	51
Figure 4.1: PV and membrane optimization cycle.....	54
Figure 4.2: a) Schematic of our PV module, with a parallel condenser layout, and b) layout of the membrane inside the membrane module, with liquid feed in contact with the GO face and vapor permeate through the membrane support.....	55
Figure 4.3: a) Schematic of Sterlitech CF042A cross-flow acrylic cell [91], b) cross-sectional design of our acrylic PV module, and c) module fully assembled for PV testing.....	56
Figure 4.4: a) Feed reservoir with saltwater solution and GO membrane, b) permeate side of the module with the mesh support and vapor outlet, c) partial condensation observed in the permeate side after switching condensers, d) salt crystallization due to a major membrane leak, with the inset showing crystallized salt deposited on acrylic wall.	57
Figure 4.5: a) GO-vacuum filtered membrane with surface defects marked by methylene blue deposition, b) SEM image of surface cracks.	58
Figure 4.6: Second iteration of our membrane module made from stainless steel, similar to the acrylic design, containing a feed reservoir, and similar layout for feed inlet and outlet and permeate outlet.	
<i>Figure made by Khalfan Almarzooqi.</i>	58

Figure 4.7: a) Membranes used for validation tests: copper (top), TFC (bottom), b) permeate amount with respect to time for the two membranes, with the calculated flux for TFC membrane, and c) tabulated flux results for a commercial PV module and our stainless steel PV module.....	59
Figure 4.8: a) Temperature profile in orange as outputted by the thermocouple and flux as measured by our PV, b) tabulated flux and standard deviation for temperatures of 30 °C and 60 °C.....	60
Figure 4.9: Cross-section of a) iteration 1 with the acrylic module, b) iteration 2 with stainless steel module, and c) iteration 3 with the top acrylic and bottom stainless steel module.....	60
Figure 4.10: a) Side view, and b) top view of membrane module iteration 3, with TFC membrane..	61
Figure 4.11: a) Membranes used for validation tests: copper (top), TFC (bottom), b) permeate amount with respect to time for copper and TFC membranes, with the calculated flux for TFC membrane, and c) tabulated flux results for a commercial PV module and our half acrylic and half stainless steel PV module.....	62
Figure 4.12: Types of condensers a) cold finger [88], b) large [89] and c) smaller [90] dry ice traps.	62
Figure 4.13: Condensers used for sampling times and condenser capacity testing, where A and B were type 1, and C and D were type 2 [89, 90].....	63
Figure 4.14: Permeate overflow (%) as a function of sampling time and type of condenser.	64
Figure 4.15: Capacity measurements of a) condenser A, and b) condenser B, as a function of sampling time.....	65
Figure 4.16: Relationship between flux ratio as a function of vacuum level and flux fraction at 600 and 758 mmHg using a) solution-diffusion model and b) pore-flow model.	66
Figure 4.17: a) Vacuum-filtered GO membrane submerged in water for 30 minutes, squares of GO membrane b) without and c) with Zn ²⁺ enhancement for 24 hours.....	68
Figure 4.18: a) XRD diffractograms of vacuum-filtered GO membranes from each solvent, and b) corresponding d-spacing of each membrane.	69
Figure 4.19: Photos of vacuum-filtered GO membranes in each solvent and their corresponding SEM micrographs showcasing the cross-sectional morphology.	70
Figure 4.20: Bar graphs of flux and rejection of vacuum-filtered membranes of each solvent system at 30 °C at a) 160 µg/cm ² , and b) 40 µg/cm ²	71
Figure 4.21: Bar graph of PV failure rates with respect to vacuum-filtered membranes from each solvent.....	72
Figure 4.22: a) Arrhenius plots of water, 1-butanol and 1-hexanol membranes, and b) corresponding activation energy of permeation flux E_J and permeation E_P	73

Figure 4.23: a) Flux vs. time series of PP, GO-ethanol on PP and PES at a loading of 80 $\mu\text{g}/\text{cm}^2$ at 30 °C, and b) flux vs. time series of GO-butanol on PES and NC at a loading of 80 $\mu\text{g}/\text{cm}^2$ and of GO-water on PES and NC at a loading of 160 $\mu\text{g}/\text{cm}^2$ at 30 °C.....	74
Figure 4.24: Schematic of water permeation across a) less porosity membrane, such as PP, and b) high porosity membrane, such as PES and NC.....	75
Figure 5.1: GO cast membranes from aqueous dispersion on a) untreated PP surface, and b) treated PP surface.....	79
Figure 5.2: GO cast membranes from all solvent dispersions right after casting (top view) and once dried (bottom row).....	79
Figure 5.3: GO cast membrane before and after low-temperature reduction at 75 °C for 16 hours.	80
Figure 5.4: GO-ethanol cast membrane a) before reduction, and b) after reduction.....	81
Figure 5.5: XRD diffractogram of GO-ethanol cast membrane before and after low-temperature reduction.....	82
Figure 5.6: a) GO-water membrane reduced at 200 °C for an hour, and b) GO-ethanol membrane before and after reduction at 250 °C for an hour. c) FTIR, e) XRD, and g) Raman analysis of GO-water membrane, and d) FTIR, f) XRD, and h) Raman analysis of GO-ethanol membrane.....	85
Figure 5.7: Teflon trough before deposition a) top-view, and b) side-view.	87
Figure 5.8: AFM micrographs of LB-deposited films from a) ethanol, b) 1-propanol, c) 1-butanol, and d) 1-hexanol with measured height profiles of flakes.	88
Figure 5.9: Histograms of lateral sheet size distribution of GO flakes as a function of solvent dispersion and deposition technique (i.e., LB or spin-coating).	90
Figure 5.10: LB trough loaded with PP porous membrane (red rectangle).....	91
Figure 5.11: LB-deposited films of GO on PP at a) higher magnification and b) lower magnification, c-d) after chemical reduction with 50 mM NaBH ₄ at 50 °C for 15 minutes.	92
Figure 5.12: Raman spectra of a) PP and b) LB-deposited monolayer GO on PP.	92
Figure 5.13: Cross-sectional SEM of cast membrane, with thickness ranging from 25 to 40 μm .	93

List of Tables

Table 2.1: Relevant solvent properties of water and 1-alcohols for graphene oxide dispersions.....	24
Table 3.1: Maximum GO slurry concentration achievable by centrifugation in respective solvent systems	35
Table 3.2: Zeta potential values of graphene oxide dispersions in respective solvents	36
Table 3.3: DLS measurement data of average graphene oxide flake sizes in respective solvents	38
Table 3.4: Absorption coefficient of all solvent stocks in sealed and continuously used conditions.	45
Table 3.5: EDS-based C/O ratios of fresh and 2-weeks-old light exposure stocks.....	48
Table 3.6: I_D/I_G ratios of all fresh and 2-weeks-old GO dispersions using peak heights and gaussian fits	49
Table 3.7: TGA weight loss of all fresh GO dispersions at 180 °C and 450 °C.....	50
Table 3.8: XRD measured peak values and corresponding interlayer spacing for each GO dispersion	51
Table 4.1: Surface area of condensers in cm^2	63
Table 4.2: Summary of properties of support membrane material.....	75
Table 5.1: I_D/I_G ratios of GO cast membranes before and after reduction	81
Table 5.2: Summary of XRD data of GO cast membranes before and after reduction at 75 °C	82
Table 5.3: C/O ratios of GO cast membranes before and after reduction at 75 °C	82
Table 5.4: Summary of Raman and XRD data of membranes reduced at high temperature	84
Table 5.5: Average and standard deviation in the measurement of lateral sheet sizes with spin-coating and LB GO films.....	89

List of Abbreviations

AFM	Atomic Force Microscopy
ATR	Attenuated Total Reflectance
CO ₂ Laser	Carbon Dioxide Laser
CP	Concentration Polarization
CV	Coefficient of Variation (%)
CVD	Chemical Vapor Deposition
DCE	1,2-Dichloroethane
DLS	Dynamic Light Scattering
DLVO	Derjaguin, Landau, Verwey, and Overbeek
DMF	Dimethylformamide
DMSO	Dimethyl Sulfoxide
EDS	Energy Dispersive X-ray Spectroscopy
EL	Electrostatic
FO	Forward Osmosis
FTIR	Fourier-Transform Infrared
GO	Graphene Oxide
H ₂ O ₂	Hydrogen Peroxide
H ₂ SO ₄	Sulfuric Acid
H ₃ PO ₄	Phosphoric Acid
KMnO ₄	Potassium Permanganate
LB	Langmuir-Blodgett
LC	Liquid Crystallinity
LCGO	Liquid Crystalline Graphene Oxide
MED	Multi-Effect Distillation
MMMs	Mixed Matrix Membranes
MSF	Multi-Stage Flash
NaBH ₄	Sodium Borohydride
NC	Nitrocellulose
NMP	N-methyl-2-pyrrolidone
NPG	Nanoporous Graphene

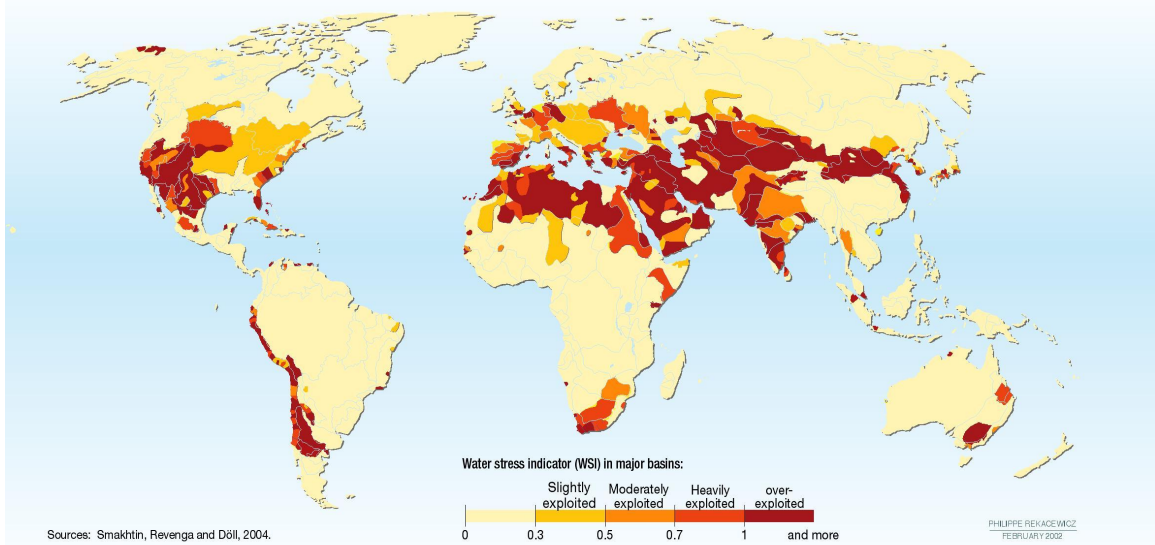
PES	Polyethersulfone
PLM	Polarized Light Imaging
PP	Polypropylene
PV	Pervaporation
RO	Reverse Osmosis
SEM	Scanning Energy Microscopy
TFC	Thin Film Composite
TGA	Thermogravimetric Analysis
UV-Vis	Ultraviolet-Visible Spectroscopy
vdW	van der Waals
XRD	X-ray Diffraction

*“Read in the Name of Allah, who has created you from a clod
and a drop of water and is the teacher of all men”.*

1 Introduction

1.1 Water Scarcity

Fresh water scarcity is quickly becoming a serious global challenge as populations grow and resources are depleted. Access to clean water is a bigger problem than hunger in over-exploited and under-industrialized areas [1]. By 2025, two-thirds of the world's population is predicted to be living in water-stressed countries [2][3]. **Figure 1.1** presents the water scarcity indices of the countries around the world from 2002, showing many countries with over-exploited water resources [4]. Seawater, which makes up 97.5% of the water on Earth, can be a viable and sustainable source of usable water via desalination. More than 300 million people around the world rely on desalinated water for some or all their needs [5]. Experts in the field agree that “the holy grail for water researchers and engineers is a desalination process that is energy-efficient, environmentally friendly and relatively cheap” [6].



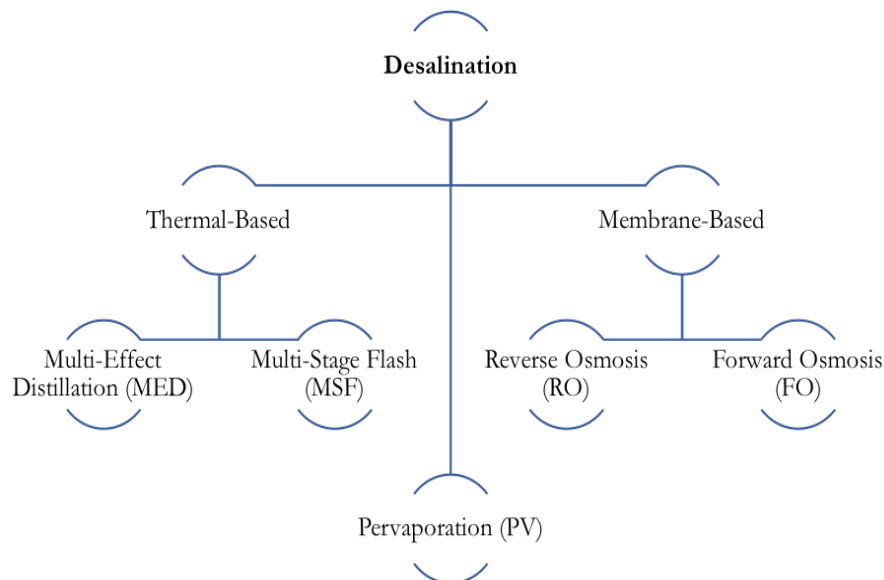
The process of desalination uses either thermal routes to volatilize and condense water, or the more efficient route of using a physical barrier, such as a membrane, that only allows water molecules through and retains salt ions. Several factors are important in determining energy efficiency of a desalination process.

1.1.1 Desalination Technologies

Desalination has a minimum energy requirement irrespective of the technology or process used. This minimum is a thermodynamic energy barrier required to separate salt ions from water molecules. In the case of a perfect system, the amount of energy required for this separation is equivalent to Gibbs free energy of mixing (ΔG_{mixing}) based on second law of thermodynamics [2][3][7]–[10]. However, practically, there is always additional energy required due to inefficiencies of the system. The separation energy efficiency of a desalination process can be divided into technology-independent (i.e. thermodynamic minimum) and technology-dependent (i.e. additional work) factors, according to the Eq. 1 below:

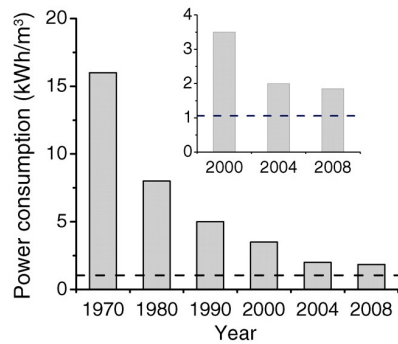
$$\eta_E = \frac{\Delta G_{\text{unmixing}}}{\Delta G_{\text{unmixing}} + W_{\text{additional}}} = \frac{E_{\text{thermodynamic min}}}{E_{\text{thermodynamic min}} + W_{\text{additional}}} \quad \text{Eq. 1}$$

The technology-independent factor (i.e., the thermodynamic minimum energy requirement) is a constant value, equal to approximately 1 kWh/m³ of water [2][3]. Technology-dependent factors include additional work to account for energy losses incurred during the process of inputting the thermodynamic minimum energy into the salt-water system. This additional work term includes inefficiencies of the membrane, membrane module, pumps and overall system design. Along with energy efficiency, environmental effects and cost are important characteristics of a real-world

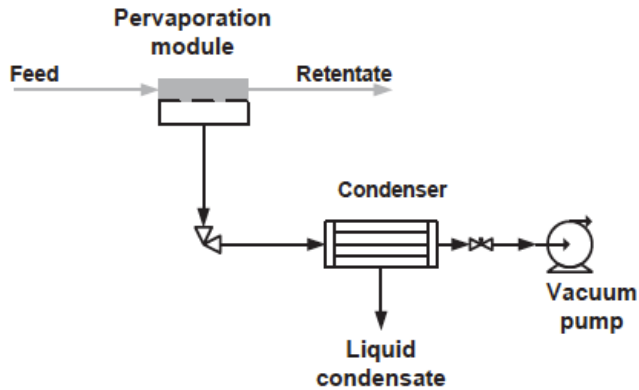


desalination process. **Figure 1.2** presents the main technologies that have been used for desalination. Desalination technologies can be categorized as either thermal desalination or membrane-based desalination. Early large-scale desalination plants, mostly in countries of the Persian Gulf, were based on thermal desalination, which involved boiling large volumes of water and subsequently condensing the vapor and collecting freshwater [1][3]. The advantages of this method are that the system does not require frequent maintenance and the resulting condensate is potable water quality [11]. However, these thermal desalination plants consume substantial amounts of thermal and electrical energy, which result in emission of greenhouse gases [3]. In attempts to make thermal desalination energy-efficient and cost-effective, multi-effect distillation (MED) and multi-stage flash (MSF) have been developed, which partially reuse the energy from the process to heat up the feed [12]. Energy consumption of thermal desalination processes reach up to 650 kWh/m^3 , which may be reduced if energy is reused, as in MED [13].

Despite efforts to make the process more energy-efficient and environmentally friendly, thermal desalination is still inefficient and not a scalable technology for the future. Most of the desalination plants constructed in the past two decades are based on reverse osmosis (RO) technology, where saltwater is pressurized against a semipermeable membrane that lets water molecules through but retains salt ions. RO requires extremely high-pressure hydraulic pumps to overcome the osmotic pressure as the salinity increases, because the osmotic pressure gets exponentially larger with increasing salt concentration [14]. New generations of RO technology have provided substantial reductions in energy consumption over the last two decades, with improvements attributed to higher-permeability membranes, use of energy-recovery devices, and the use of higher-efficiency pumps [15]. Energy consumption in RO has dropped significantly over the last four decades, bringing it down to $\sim 2 \text{ kWh/m}^3$ [15], as plotted in **Figure 1.3**, reproduced from [3].



Most recently, pervaporation (PV) has surfaced as a potential technology for desalination. PV can be thought of as a hybrid of thermal and membrane desalination technology, where the feed is a liquid mixture and the permeate is recovered as a vapor [16]. The PV module is depicted in **Figure 1.4**, as reproduced from [16]. PV has been well-known in other applications, such as dehydration of organic solvents, evaporation of volatile organic compounds from aqueous solutions, and separation of mixed anhydrous organic mixtures [17][18]. Integrating distillation and PV (i.e. use of a selective membrane) increases the separation efficiency of azeotropic mixtures, which are extremely difficult to separate by distillation alone [19]. The use of a membrane which is selective reduces the energy barrier to vaporization to the more selective species, resulting in preferential vaporization.

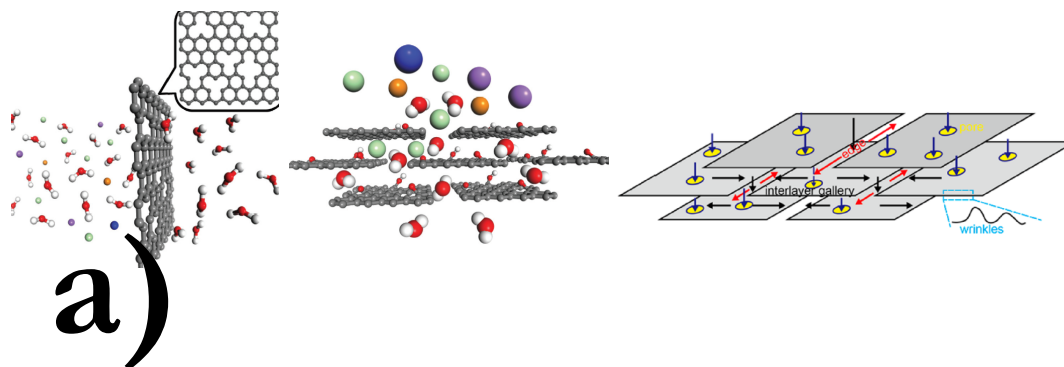


For PV desalination, the use of a selective membrane is key. Unlike thermal distillation, water in PV can vaporize at temperatures as low as 30 °C because of the use of the membrane, which reduces the vaporization energy barrier. And unlike RO, PV is not limited by the osmotic pressure, which means PV can easily handle much higher salinity solutions without additional energy consumption [20][21]. PV becomes more economically viable when low-grade heat, such as solar energy, geothermal energy or waste heat from industry can be used as the power source [2][3][8][20]. Using renewable energy sources can also minimize greenhouse gas emissions, making PV a more environmentally friendly technology.

1.1.2 Membrane Materials for Desalination

Membrane-based separation processes have gained considerable importance in industry due to merits such as high separation efficiency, potential energy savings compared with the traditional distillation techniques [2][19] in addition to ease of integration and control [13][22]. Chemical and physical compatibility of the membrane with the permeating species are crucial for a selective performance. Common membrane materials include polymeric, inorganic and mixed matrix (i.e. hybrid of the first two). Polymeric membranes are extensively used industrially because of the wide range of materials and properties available. Polymeric membranes are mechanically stable and easily tunable for surface structure and morphology. Polymers are also abundant and inexpensive [24]. Drawbacks of polymeric membranes include their moderate permeability and selectivity capabilities as well as low chemical and thermal resistance [24]. State-of-the-art membranes for RO include composite polymeric membranes, which can achieve a flux of 21 L/m²/hour and a salt rejection of 99.6% [23], but these composite membranes are chemically unstable and need to be replaced frequently.

Despite being more developed and researched, the performance of polymeric membranes as well as inorganic membranes are comparable to preliminary performance of graphene-based materials. nanoporous graphene (NPG) and multilayer graphene oxide (GO) membranes, as depicted in **Figure 1.5** [24][25], have shown significant promise for desalination [24][26]. Since its discovery, graphene – an atomically thin layer of sp² hybridized carbon - has gained a lot of interest with its superior electrical, thermal, and mechanical properties. It has shown potential in areas as diverse as composite materials, energy storage and conversion, sensors, drug delivery, field emission devices and nanoscale electronic



components, and molecular separation [27][28][29][30]. However, mass production and processing is the bottleneck to realize the full potential of these graphene-based materials on any large-scale

commercial level [31][32]. Methods that produce pristine graphene, such as CVD and micromechanical exfoliation, are not compatible with mass production processes and are costly [32]. Most commonly, NPG membranes are obtained via CVD making this technology expensive due to the high cost of capital, slow growth rates and the inability to create defect-free coatings over large areas. The novelty behind GO is that it combines the exceptional capabilities of ceramics while maintaining the ease of manufacturing and low cost of polymers [51][52][58]. Similar to NPG membranes, GO membranes have high chemical, thermal, and mechanical stability, as well as high permeability and selectivity [33]. GO membranes have shown promising performance in desalination, with potential for a development of an inexpensive high flux and high rejection membrane.

1.1.3 Graphene Oxide Dispersions

Solution processing may be the answer to large-scale manufacturing architectures of graphene-based materials due to its versatility, low cost, and high throughput [34]. Graphene has shown very limited dispersibility in common solvents. Researchers have achieved stable graphene dispersions in few organic solvents, such as N-methyl-2-pyrrolidone (NMP), dimethyl sulfoxide (DMSO) and N,N dimethylformamide (DMF) [31], but all these high boiling point organic solvents are difficult to remove during processing, which can cause problems [35]. Graphene dispersion can also be achieved in water and other low boiling point solvents, but only with the use of stabilizers, such as surfactants and polymers to provide electrostatic or steric stability. However, for many applications, the presence of surfactants and polymers is not desirable [31][35][36]. To date, from the manufacturing perspective, the challenge remains to find dispersing solvents that are volatile, less toxic, and environmentally friendly, i.e. alcohols and water [32][37].

Graphene oxide offers many advantages over graphene, such as affordable large-scale production, ease of functionalizability, and solution-processable capabilities [31][38][39], therefore, researchers have put in a lot of effort in achieving stable dispersions of graphene oxide in solvents. Researchers are trying to expand the range of solvents that can host stable dispersions of graphene oxide for solution processing, and thus, for any applications of graphene-based materials.

1.2 Motivation for the Project

The main motivation for this project is to advance research into membrane materials and technologies for more efficient desalination. Current state-of-the-art RO technology with polymeric thin-film composite membrane (TFC) achieves a flux of 21 L/m²/hour with a salt rejection of 99.6% [23], however, these membranes have extremely limited chloride resistance, which causes the membrane to dissolve within seconds [40]. There has been slight improvement to the performance of these membranes as well as their stability [41]. However, the pursuit has now moved towards other materials. Novel nanomaterials, such as graphene oxide, with its high chemical stability, have shown to be a promising replacement. Along with issues of TFC membranes, RO technology itself has inefficiencies and limitations, which has resulted in a search for new technologies, such as forward osmosis (FO) and PV [42][43]. PV desalination has not reached its full potential as it is relatively new to the field, but recent literature and developments from the academic community have shown that it can become a viable technology for large-scale desalination [44]. It has been argued that increasing membrane permeability beyond a certain point will not result in significant energy savings, especially at a cost of lowered salt rejection [45]. However, finding membranes with high permeability and excellent salt rejection (~100%) can reduce or eliminate second-pass operations, which can lessen capital costs. In addition, novel membrane materials can enable surface modification to reduce membrane fouling and chemical cleaning, which can lessen operational costs in terms of pre-treatment and higher feed pressures [46].

In this thesis, we investigate the use of graphene oxide, a promising nanomaterial, in PV desalination, with the aim of developing an inexpensive desalination system that can achieve high flux and high rejection. Our work follows and extends trends in the field, and this document describes all aspects of the project, including the design and production of membrane materials, processing of graphene oxide solutions and films, and the development of a lab-scale PV desalination testing system. My work also explores some of the challenges of solution processing of graphene oxide, for a step towards large-scale commercial application.

1.2.1 Objectives

The main objective of our project is to develop an efficient graphene oxide membrane with high flux and high rejection in a PV system. In addition, we also aim to find better ways to process graphene oxide dispersions in a more scalable way. More specifically, we aim to:

- Study graphene oxide dispersions and membranes fabricated from aqueous and non-aqueous solvents: Generally, graphene oxide membranes for desalination are prepared from graphene oxide dispersions, which can dictate the morphology, interlayer spacing, and chemistry of the membranes. Having a better understanding of graphene oxide dispersion properties better equips us for performance optimization of our membranes for PV.
- Design a PV module, including the membrane cell, condenser design, vacuum and other peripheral components: Commercial PV modules are expensive and not compatible with our membrane requirements, therefore, developing a custom PV module designed for our requirements is an important objective. The PV module and the peripheral components will need to be validated and optimized.
- Test GO membranes in the context of PV desalination: GO membranes have been used for PV desalination. However, the performance of the membranes has not been extensively studied. Here, we aim to get a better understanding of transport mechanism, stability and other factors of the membrane.
- Study alternative methods for making ultrathin and scalable graphene oxide membranes: Most GO membranes used for filtration are prepared via vacuum filtration, which is a technique that is not scalable. Here, we look at extending membrane preparation techniques to alternatives that are more easily scalable, can produce ultrathin membranes, and are reproducible.

1.3 Organization of Thesis

This thesis covers a comprehensive design and development of graphene oxide membranes and PV module for a lab-scale desalination testing system, in addition to advancing the work of graphene oxide dispersions for solution processing capabilities.

Chapter 2 starts off with specific background and fundamentals of PV in the context of desalination, including transport phenomena and models used for predicting transport across the membranes. Then, a brief background on the membrane materials is provided, which includes polymers, ceramic and hybrids as well as graphene-based materials. A background on graphene oxide dispersions is also provided, where we set the stage for the next chapter.

Chapter 3 presents our objectives for the study of graphene oxide dispersions in more detail and discusses our findings, in terms of dispersion properties, graphene oxide solvent-dependent transformation, and a speculative model for this chemical transformation.

In chapter 4, we present our detailed experimental design of PV technology, our setup optimization and results. We discuss the various iterations of the PV module designs as well as validation tests that were carried out to compare performance to a commercial module. We also present the GO membrane performance results and discussion. In this part, we present the vacuum-filtered GO membranes from water and 1-alcohol dispersions and discuss the different ways to improve PV flux and rejection.

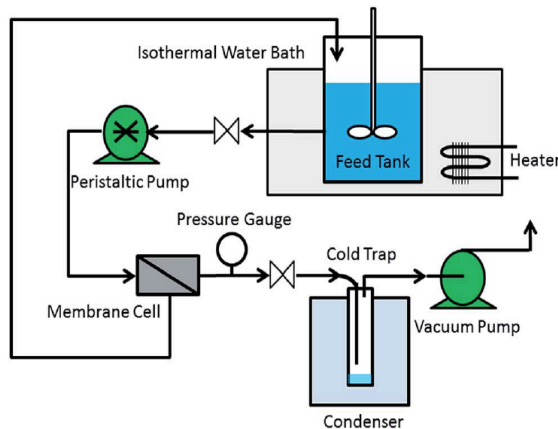
Chapter 5 is an extension of the previous chapter, where we look into other techniques of producing graphene oxide membranes, such as casting and Langmuir-Blodgett (LB) techniques. Here, we briefly look at the properties of freestanding GO films and the effects of thermal reduction.

The final chapter contains conclusions and directions for future work.

2 Background

2.1 Fundamentals of Pervaporation

As mentioned earlier, PV is new to the field of desalination, however it has been extensively used in replacement or enhancement of distillation [19][47]. The driving force for transport in PV is a chemical potential gradient across the membrane that is controlled by the feed temperature and the vacuum level. The properties of the membrane are crucial to the separation performance. With the use of a highly selective membrane, the energy barrier to vaporization is greatly reduced, which results in increased flux at the same operating temperatures. The overall setup of lab-scale pervaporation is shown in **Figure 2.1**, reproduced from [48]. A saltwater feed is circulated to the membrane cell using a peristaltic pump. On the permeant side of the membrane cell, a vacuum pump connects to a condenser to collect the permeate, and a vacuum gauge is used to measure the vacuum level.



The principle of PV, as illustrated in **Figure 2.2** and **Figure 2.3**, includes a liquid saltwater mixture on the feed side of a membrane cell, separated from a vapour phase on the permeate side by a semi-permeable membrane. Water molecules are removed from the feed and brought into the vapour phase due to a chemical potential gradient driving force [16]. Performance of a PV process is characterized by water flux and salt rejection. Experimentally, the water flux J [$\text{kg}/\text{m}^2\text{h}$] and salt rejection R [%] can be obtained by Eq. 2 and Eq. 3, respectively:

$$J = \frac{M}{A \cdot t} \quad \text{Eq. 2}$$

$$R = \frac{C_f - C_p}{C_f} \times 100\% \quad \text{Eq. 3}$$

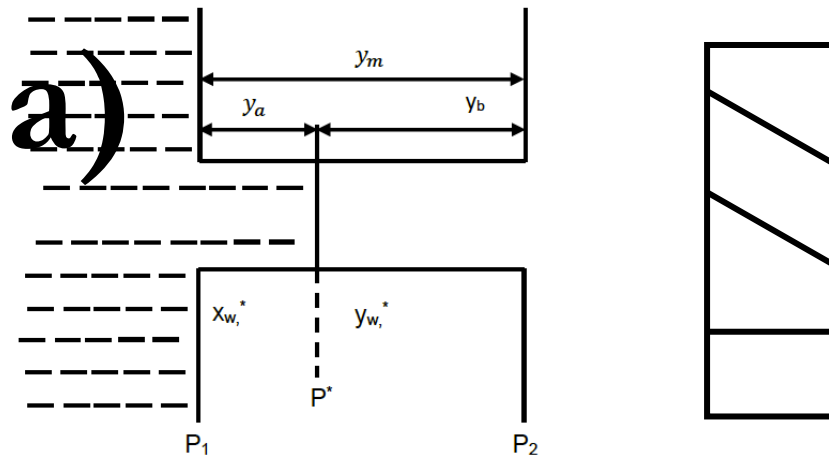
where M [kg] is the mass of permeate, A [m^2] is the effective membrane area, t [h] is the collection time, and C_f and C_p are the salt concentrations in the feed and permeate, respectively [49]. Flux is proportional to the driving force, which can be modelled with two commonly accepted mass transport models: i) the pore flow model and ii) the solution-diffusion model, both to be briefly discussed here.

2.1.1 Pore Flow Model

The pore flow model is based on the assumptions that:

- Part of the pore is initially filled with liquid, where liquid phase transport takes place
- Liquid changes into vapour inside the pore at the phase boundary (P^*)
- The permeant is then transported as a vapour to the permeate side

The pore flow assumes perfectly cylindrical pores penetrating the entire membrane, as depicted in **Figure 2.2a** reproduced from [50], [51]. The membrane pressures denoted by P_1 and P_2 , where P_1 and P_2 are the pressures of feed liquid and permeate vapor, respectively. P^* at the phase boundary is the saturation vapor pressure of feed component. **Figure 2.2a** is only valid if $P_2 < P^*$. If $P_2 > P^*$, the entire pore is filled with liquid.



The molar flux of component i across the pore, in liquid and vapor phases, as described by T. Okada *et al.* is as follows [52], [53]:

$$Q_{total} = \frac{A_{mix}}{y_a} (P_1 - P^*) + \frac{B_i}{y_b} (P_{i,*}^2 - P_{i,2}^2) + \frac{B_j}{y_b} (P_{j,*}^2 - P_{j,2}^2) \quad \text{Eq. 4}$$

$$A_{mix} = \frac{\pi r^4 \rho N_t}{8\eta M} \quad \text{Eq. 5}$$

$$B = \frac{\pi(2rt-t^2)^2 t N_t}{8r} \frac{RT}{\mu} (k'_H)^2 \quad \text{Eq. 6}$$

where Q_{total} [mol/m²s] is the total flux of liquid and vapor flow, A_{mix} is a pore-flow model coefficient of the liquid mixture as described in Eq. 5, r is the pore radius, ρ [kg/m³] is the liquid density, N_t is the total number of pores per effective area, η [Pa.s] is liquid viscosity, M is molecular weight of mixture, y_m [m] is the full pore length, y_a and y_b are fractions of the liquid-filled and vapor-filled portions of the pore, respectively. B_i and B_j are also coefficients as described in Eq. 6, for the i^{th} and j^{th} component, respectively, t [m] is the thickness of adsorbed monolayer of gas, R [m³bar/Kmol] is the ideal gas constant, T [K] is temperature, and k'_H [mol/m³bar] is the product of the weight of the membrane/volume of adsorbed gas molecules and Henry's constant.

Eq. 4 for molar flux through the pores can be seen as a superposition of three components: liquid phase transport of the mixed feed (i.e. salt and water), and vapor transport of each component separately. Since salt cannot be vaporized, the third term regarding component j in Eq. 4 can be disregarded. As seen in the formulas, the driving force for liquid transport comes from the pressure difference across the membrane, which produces a chemical potential gradient, as shown in **Figure 2.2b**. This is different from the solution-diffusion model, in which the membrane is portrayed as a dense layer, with a concentration gradient across, which produces the chemical potential gradient driving the transport. In the two models, the derivation differs based on how the membrane is portrayed.

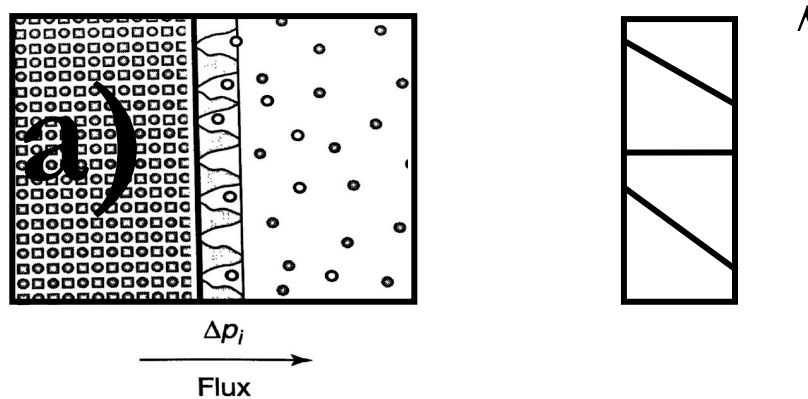
For vapor transport, an assumption is made. As seen in Eq. 6, the thickness of the adsorbed monolayer gas is taken into account, which is to assume that the pore is exactly the size for vapour to adsorb onto the pore wall, occupying the entire space, thus the transport happens via surface flow mechanism, a common gas flow model [50]. If the pore is too large to accommodate Knudsen flow, this model becomes inapplicable, setting an upper pore size limit of 1-10 Å [50].

The pore flow model has a few limitations that affect its applicability. For instance, the assumption of the perfect cylindrical pores is poorly justified because it is unlikely to develop membranes with a perfect pore size distribution in the range of 1-10 Å [51].

2.1.2 Solution-Diffusion Model

The solution-diffusion model has been widely accepted for current applications of PV, depicted in **Figure 2.3** reproduced from [18], [49], [54]. Based on this model, water molecules preferentially adsorb and diffuse through the membrane, while hydrated salt ions are rejected. Salt rejection is generally very high in PV since salt ions cannot evaporate [49]. This model of mass transport through dense polymeric membranes assumes three key stages in transport of vapor:

- Selective sorption of the feed mixture onto the membrane surface
- Diffusion of the adsorbed species through the membrane under a concentration gradient
- Desorption of the permeant as vapour on the permeate side



The first two steps are dominant contributors for separation. The third step, i.e. desorption, of the permeant under vacuum is thought to be very fast and does not offer significant resistance to the transport. The flux of component i in relation to the overall driving force as described by Fick's second law is as follows:

$$J_i = -D_i \frac{dc_i}{dx} = \frac{D_i(c_{if(m)} - c_{ip(m)})}{l} \quad \text{Eq. 7}$$

where D_i [m^2/s] is the diffusivity of component i in the membrane, $c_{if(m)}$ and $c_{ip(m)}$ [kg/m^3] are the feed and permeate concentrations of compound i , and l [m] is the membrane thickness. Flux can also be expressed in terms of the vapour pressures of component i on the feed and permeate sides of membrane, as follows:

$$J_i = \frac{P_i}{l} (X_i \gamma_i p_i^{sat} - Y_i p_{ip}) \quad \text{Eq. 8}$$

where P_i is the permeability coefficient, X_i , γ_i and p_i^{sat} are the mass fraction, activity coefficient, and saturation vapour pressure, of component i in the feed, Y_i and p_{ip} are the mass fraction and vapour pressure of component i in the permeate side [89]. The permeability coefficient is related to diffusivity (D) and solubility (S) coefficients as follows:

$$P_i = D_i S_i \quad \text{Eq. 9}$$

The permeability and selectivity of PV are governed by the solubility and diffusivity of species in the membrane. Solubility of a component within the membrane polymer depends on their relative solubility parameter values. The solubility parameter measures the strength of the intermolecular forces (cohesive energy) holding molecules together in the liquid phase [55]. PV involves not only mass transport through the membrane but also heat transfer. Similarly, the energy required for a change in the physical state of liquid water to vapour (enthalpy of vaporization) can be understood in this context. The total energy of vaporization of liquid consists of intermolecular interactions that need to be overcome [55]. In the case of desalination, there exist hydrogen-bonding, ion-dipole bonding, and/or ion-ion interactions between the salt ions, water molecules, and the membrane [49], [55]. Selective sorption and vaporization of water molecules by the membrane is complex and is not completely understood. However, based on research with PV of organic compounds, solubility parameter values of the membrane polymer and desired component to be separated should be of comparable polarity; this will result in preferential sorption. Solubility coefficients are not constant but depend strongly on the concentration and operating conditions, such as feed temperature and permeate pressure.

Preferential permeability of component i depends equally on the solubility coefficient (thermodynamic parameter) and the diffusivity (kinetic parameter) [55]. Diffusivity of a component in the membrane is a strong function of the size and shape of the permeant [21][51]. However, sorption has a strong effect on diffusion. Higher sorption always results in higher rates of diffusion [51]:

- An increase in the concentration of the permeant in the polymer swells it, resulting in lower activation energy for diffusion
- Once swelling occurs, more free volume becomes available for permeation

As mentioned previously, preferential sorption does not guarantee preferential permeability because once preferential sorption occurs, the polymer swells and the diffusion rates for both components increase, resulting in “reverse selectivity” [51]. Similar to the solubility coefficient, the diffusivity is usually not constant and depends heavily on composition, feed temperature and permeate pressure [21][51]. Transport through a dense polymer may be considered as an activated process, which can be represented as an Arrhenius type of equation [21]. Thus, the diffusion and solubility coefficient can be expressed as:

$$D_i = D_0 e^{(-\frac{E_d}{RT})} \quad \text{Eq. 10}$$

$$K_i = K_0 e^{(-\frac{\Delta H_s}{RT})} \quad \text{Eq. 11}$$

where E_d is the activation energy for diffusion, ΔH_s is the heat of solution, and D_0 and K_0 are temperature-independent constants. Based on the relationship shown in Eq. 14, the permeability coefficient then becomes:

$$P_i = P_0 e^{(-\frac{E_p}{RT})} \quad \text{Eq. 12}$$

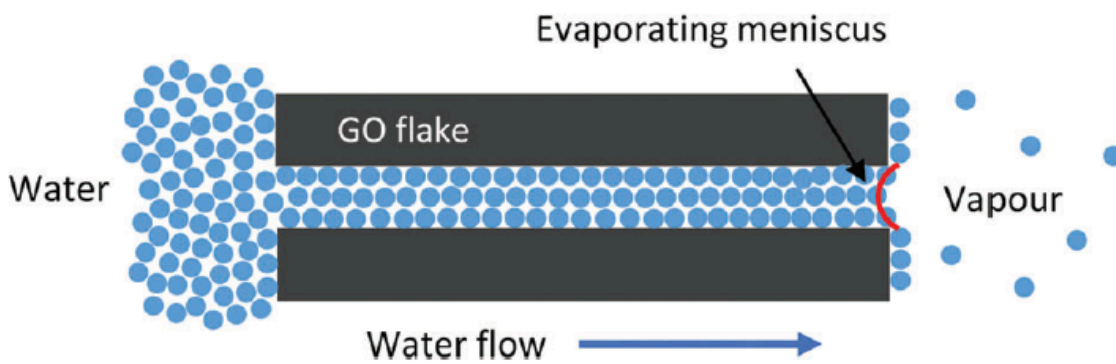
where $E_p = (E_d + \Delta H_s)$ is the activation energy of permeation. P_0 is a constant, equal to the product of D_0 and K_0 . These activation energy barriers can be experimentally found.

2.1.3 Transport Across Graphene Oxide

Most commonly, the transport mechanism to explain PV performance of the membranes is done by the solution-diffusion model, where the water molecules solubilize on the surface and diffuse across the dense membrane based on their solubility and diffusivity coefficients. However, with the unique structure of multilayer GO membrane and the approximate pore size of 3.5 Å and an interlayer spacing of 6.9 Å, the pore-flow model may be applicable in explaining the performance of GO membranes in PV desalination [61].

The pore flow model was recently used in explaining transport phenomena of water across GO membranes in PV. In this work, Chong *et al.* hypothesized based on MD simulation results of GO that the transport of water occurs through the graphitic domains of GO membranes [56]. MD simulations showed that water may permeate across the interlayer space in a bulk phase with one to three layers of water. Bulk phase transport of water cannot be explained by solution-diffusion model, which also fails to explain the high permeation of water through GO.

Chong *et al.* believe that the rate-determining step should be the mass transfer step on the permeate side, which is different from the solution-diffusion model, where desorption is assumed to be very a low resistance process. Chong *et al.* propose that water permeates as a liquid across the entire nanochannel and evaporates as it exits the GO membrane, as shown in **Figure 2.4**.

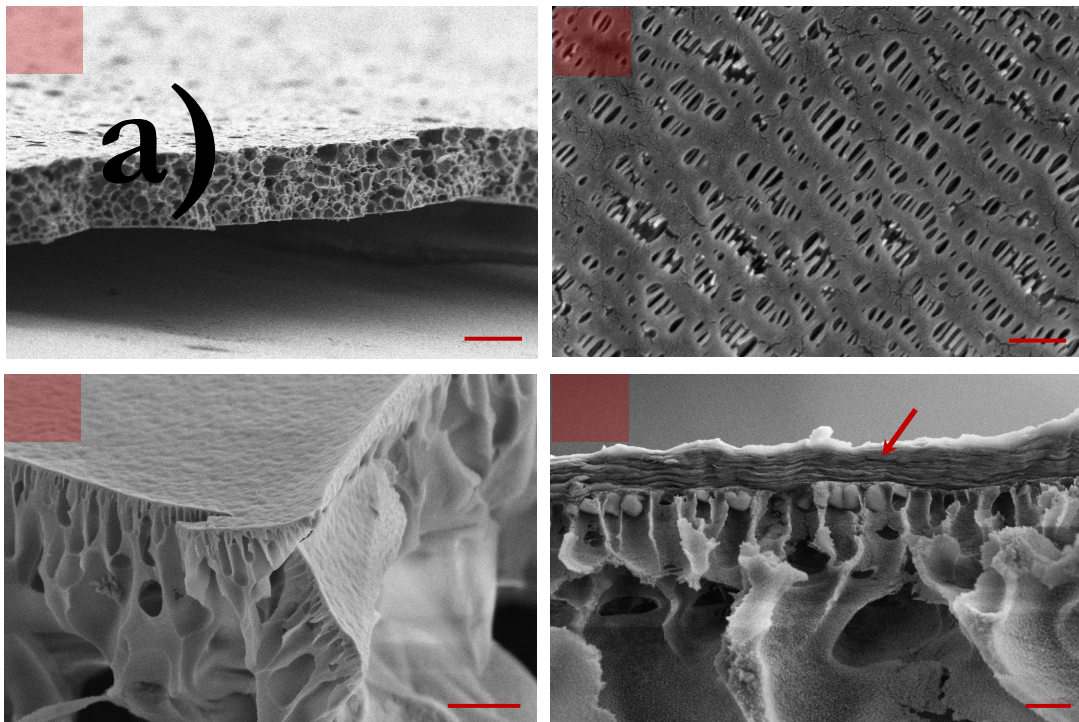


We believe that the above work from Chong *et al.* and pore-flow model explain the behaviour of our GO membranes. Here in this thesis, the pore flow model is used to explain the transport across GO membranes.

2.2 Membrane Materials

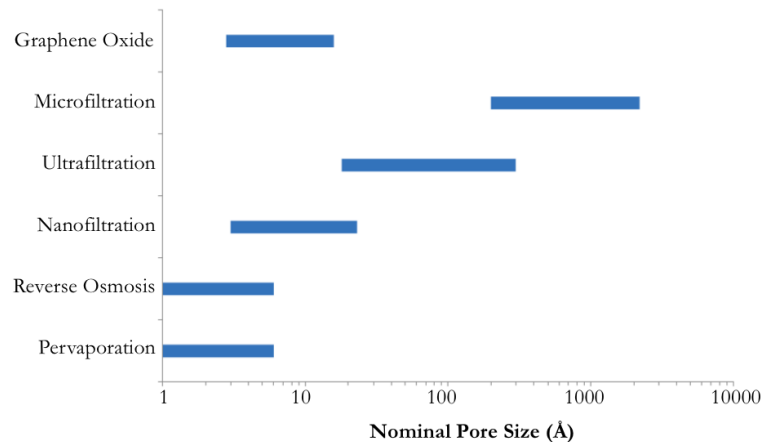
PV membranes must be developed with three criteria in mind: selectivity, productivity, and stability [24]. In the context of desalination, selectivity and productivity refer to the salt rejection and permeation flux of the membrane, respectively. Stability of the membrane is crucial for long-term and reliable performance.

Membranes can be generally characterized into two categories: isotropic and anisotropic. Isotropic membranes have a uniform composition and morphology across the membrane while anisotropic membranes may have a non-uniform composition or morphology [57]. Isotropic membranes are usually microporous and have symmetric pores across the membrane as well as a uniform composition. These membranes are usually prepared by phase inversion process, which has enabled the polymeric membrane industry's progress. The idea is to cast a film from a solution of polymer and solvent and immerse the cast film in a non-solvent of the polymer. A requirement of successful phase inversion process is partial miscibility of non-solvent with solvent. At the immersion of the cast film, the mixing of solvents resulting in non-solvent inflow and solvent outflow causes the precipitation of the polymer. The phase inversion process is extremely versatile and has been extensively studied. The morphology of the phase inverted membranes can be improved with the optimization of the tertiary system of solvent, non-solvent and polymer, in addition to other additives. **Figure 2.5a** presents a type of isotropic membrane obtained from phase inversion. The polysulfone (PSF) cast solution was prepared at 15 wt% of PSF and NMP, with water as the non-solvent. A less common method to prepare isotropic membranes is a combination of extrusion and stretching technique, where a crystalline polymer is extruded near its melting point, followed by cooling, annealing and stretching.



This stretching creates slit-like pores, as shown in **Figure 2.5b**, which is a commercial polypropylene (PP) membrane typically used as a battery separator. Phase inversion can also be used to achieve anisotropic membranes, which are identified by their defining feature of a thin nonporous layer and larger finger-like pores across the membrane, as shown in **Figure 2.5c**. Here, the composition of the membrane across the membrane is uniform, but the morphology is not. A common anisotropic membrane with a combination of compositional and morphological non-uniformity is TFC membranes used for RO. These TFC membranes are essentially a phase inverted PSF membrane with finger-like pores across the membrane, with a thin nonporous layer of polyamide, introduced by interfacial polymerization. **Figure 2.5d** is an SEM micrograph of our GO membrane on a PSF support, which is similar to TFC membranes.

The type of membrane used is based on the separation requirements. As presented in **Figure 2.6** (reproduced from [50]), membrane pore sizes decrease in the order of microfiltration (MF), ultrafiltration (UF) and nanofiltration (NF). RO membranes are essentially considered nonporous (i.e. dense) and exclude particles and low molar mass species, such as salt ions. PV and gas separation have similar requirements as RO. The nominal pore size of graphene oxide membranes between from 5-10 Å are in the right range for PV and RO.



Membrane separation is dominated by polymeric membranes for industrial use, due to their versatility, low cost, ease of manufacturing, and the maturity of the technology. However, there are also inorganic membranes, which include ceramics. Ceramic membranes have exceptional permeability and

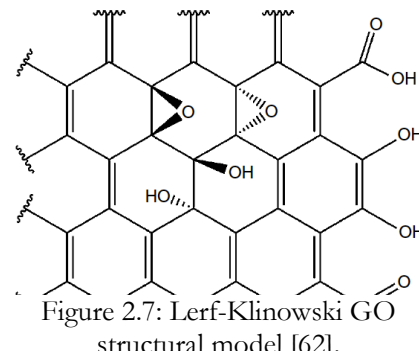
selectivity in addition to chemical and thermal stability. However, their mechanical instability and high cost as well as difficult manufacturing processes make them inapplicable for large-scale use.

Hybrid or mixed matrix membranes (MMMs) are mostly researched on a lab-scale, which are prepared by adding an inorganic filler in a polymeric matrix. Fillers such as zeolites, carbon nanotubes, silica nanoparticles, and graphene oxide have been widely researched [58][59][60][61]. The preparation techniques are similar to polymeric membranes with an additional complication of uniformly distributing the filler material in the matrix to maximize the performance. To avoid confusion, adding graphene oxide as a filler in a polymeric matrix is completely different from using graphene oxide as an active layer portrayed in **Figure 2.5d**.

2.2.1 Graphene Oxide Membranes

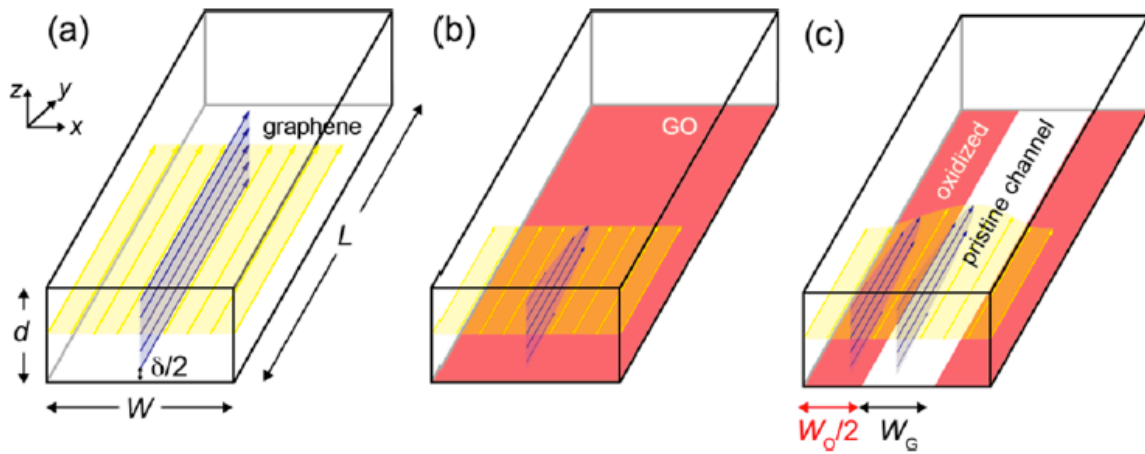
Multilayer graphene oxide membranes have gained considerable interest for water desalination based on their excellent permeability of two to three orders of magnitude larger than current state-of-the-art RO membranes, as well as excellent molecular separation capabilities, based on molecular dynamic (MD) simulations [25][33]. MD simulations help to characterize the atomistic mechanism of water permeation and ion rejection, which is difficult to do with experimental approaches. MD also sheds light on the effects of interlayer spacing, oxygen functionality, and applied pressures on the performance of GO membranes, which guide the way in our optimization [33].

GO is a 2D material that is derived from a graphene backbone with oxygen functionalities on the basal plane as well as edges. A commonly accepted model for the proposed chemical structure of GO is the Lerf-Klinowski model, as shown in **Figure 2.7**, where GO flakes contain epoxides and tertiary alcohol groups on the basal plane and carboxyl and hydroxyl groups on the edges [62][63].



The ratio of the oxygen functionalized and graphitic domains (i.e., C/O ratio) of GO depends heavily on the synthesis and purification process. Dimiev *et al.* showed that they were able to achieve extremely oxidized GO, which is white in color, compared to the conventional GO that is brown, where the color indicates the conjugation of the π -system [64].

Therefore, GO membranes can be considered as two parts: the pristine graphene region and the oxidized region [65]. Similar to CNTs, water molecules can achieve ultrafast permeation across the nanochannels of GO through the pristine graphene region due to the frictionless hydrophobic walls [66]. As shown in schematic in **Figure 2.8**, Wei *et al.* proposed water transport models across graphene and oxidized domains of the GO membrane, where the pristine graphene channel is observed to have a higher permeability and a flatter velocity profile (**Figure 2.8a**) due to the significant boundary slip [25]. The oxidized regions of the GO membrane interact strongly with the water molecules, thus hindering their permeation, as shown by their reduced permeability shown in **Figure 2.8b-c**. However, these oxygenated groups have shown to enhance the rejection ability due to the increase intermolecular interaction [67]. Based on the aforementioned simulation results, GO membranes can be partially reduced to increase the graphene domains and increase the water permeation. It is also observed that compared with the first layer of water, the transport of a second layer of water molecules is more energy-favorable, where the first layer of water minimizes the permeation barrier for the second layer of water [66].

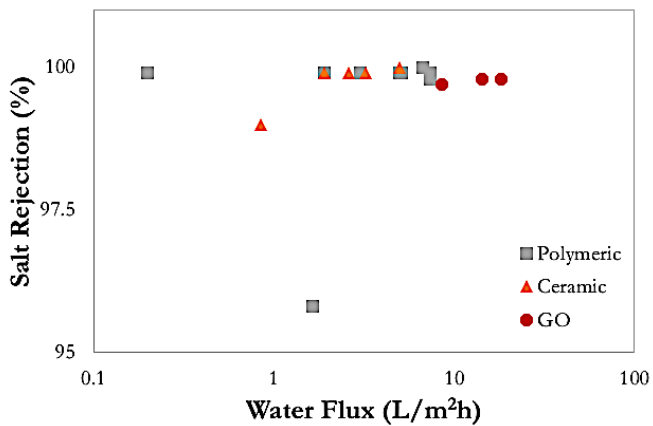


Selective transport of water across the GO membrane is thought to be due to a combination of size exclusion and affinity. Salt rejection capabilities of GO membrane is dependent on the interlayer

distance as well as the type of ions. According to MD simulations, an interlayer distance smaller than 7 Å reduces water flux while distances larger than 8.5 Å lowers rejection [33]. Salt ions, such as Na^+ , K^+ , Mg^{2+} and Ca^{2+} have different permeabilities through the membrane because of their hydrated shells and diffusion coefficients. It is seen that these ions have two solvation shells; the inner one that is more rigid and the outer one that is weakly connected [67]. With the outer shell weakly connected, these ions can easily move across smaller gaps by adjusting. At the nominal interlayer distance of 7.5 Å, the effect of applied pressure on the GO membrane is very linear; increasing the pressure increases permeation while decreasing salt rejection. However, at smaller interlayer distances, such as 4.5 Å, the membrane is impermeable even at high pressures.

The aforementioned MD simulation studies help us gain more insight about transmembrane process of GO. However, it does not consider the issue of swelling. Many groups have tested GO in a RO setting. Unfortunately, due to its hydrophilicity, the membrane swells upon immersion, thus expanding the interlayer distance and losing all separation capabilities [24][26][59]. To overcome this challenge, GO can be either chemically or mechanically confined to minimize swelling. Hu *et al.* attempted to stabilize GO by cross-linking the GO sheets with 1,3,5-benzenetricarbonyl trichloride (TMC), but they were still not able to achieve more than 40% of NaCl rejection [68]. Physical confinement of GO has also been attempted in order to decrease the swelling effect. Abraham *et al.* were able to minimize the swelling effect of GO by embedding GO laminates in epoxy, which resulted in increased rejection of 97%, but with extremely low permeation [69]. In addition, the method is tedious and not scalable to large-scale applications.

However, based on preliminary studies, GO membranes have performed noticeably better in PV compared to RO, as well as compared to polymeric and ceramic membranes in PV [49][70][71][72][73], which is compiled in **Figure 2.9**. This may be due to the fact that the membrane contacts water on only one side and thus ameliorates swelling. Therefore, GO membranes have potential to be further developed. The salt rejection of GO membranes were always ~99.8% while the flux changed from 8 to 18 L/m²h, due to differences in membrane support and chemistry. The flux can be optimized even further, and with the right set of parameters (i.e. membrane support, interlayer distance, oxygen functionality), GO membranes can have high flux and high rejection.

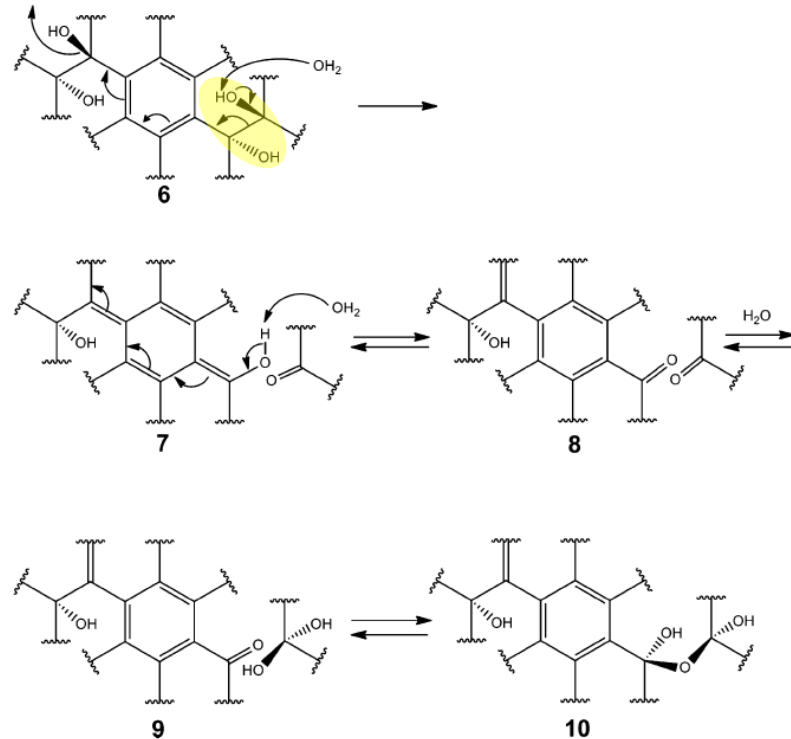


2.3 Graphene Oxide Dispersions

Graphene oxide membranes used for PV are most commonly obtained from vacuum filtration, which are prepared from graphene oxide dispersions. There are two ways of achieving graphene oxide dispersions: through direct exfoliation of graphite oxide in polar aprotic solvents [36][74], and through solvent exchange of Hummer's graphite oxide [75][76]. The process of direct exfoliation of graphite oxide is only limited to polar aprotic solvents and water, which are capable of spontaneous exfoliation of graphite sheets due to their nucleophilic nature [74]. As reproduced from [64], **Figure 2.10** shows a schematic of the chemical transformation induced by the reaction between graphite oxide and water, which is a polar protic solvent. Water is the only exception because of its highly polar nature. Polar aprotic solvents that can exfoliate graphite oxide include NMP, and DMF [35].

Water ionizes one of the 1,2-diol functional group of graphene oxide (highlighted in structure 6), which eventually results in the formation of an additional C=C bond (structure 8) [64][74]. This reaction mechanism explains two experimental observations: extension of conjugated aromatic areas, and the graphene oxide acidic properties by conversion of tertiary acids into ketones [64]. Similar observations of chemical transformation have been made of graphene oxide in NMP and DMF systems. Since this chemical transformation affects the composition of graphene oxide, resulting in an obvious color change from yellow to dark brown, it is undesirable for research and long-term storage of graphene oxide because the properties of the material are unknown and dynamic [64][74][77]. This

drives the motivation to procure solvents that do not force this chemical transformation. Generally, the solvents required to form stable dispersions of graphene oxide would have to be polar since non-polar solvents cause aggregation [35]. There are two types of polar solvents; protic and aprotic. A polar protic solvent contains a labile H⁺ that can be easily donated, while an aprotic solvent does not have this H⁺ group. As observed experimentally, aprotic solvents cause the chemical transformation.



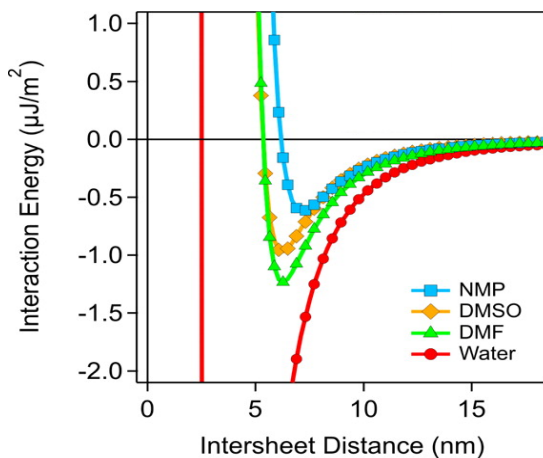
Thus, one of our objectives is to find polar protic solvents that can form stable dispersions. Alcohols fall in the category of polar protic solvents that are unable to exfoliate graphite oxide, thus it cannot induce chemical transformation on its own. It is widely accepted that a stable dispersion is achieved from graphene oxide in water due to strong electrostatic interactions [78]. However, there is some disagreement as to whether the alcohols provide the same dispersion stability [28][36]. For example, J. Paredes *et al.* [36] and Khan *et al.* [28] show that ethanol and 1-propanol do not achieve stable dispersions based on their UV-vis spectroscopy analysis, which will be discussed in detail later. However, R. Jalili *et al.* [79] is able to achieve a good dispersion of graphene oxide in methanol and ethanol.

The quality of a dispersion, whether a good dispersion is achieved, is dictated by colloidal stability. The origin of the colloidal stabilization of graphene oxide in aqueous medium has been studied and explained. Classical DLVO theory sufficiently captures the colloidal properties of graphene oxide in water, where the essence of the theory is that the total interaction forces equals the sum of van der Waals (vdW) and electrostatic (EL) forces [75]. In a system of identical particles, such as graphene oxide flakes, vdW is always attractive and EL is always repulsive, thus in simple terms, EL forces need to overcome vdW forces in order to ensure no aggregation. However, in organic solvents, the simple DLVO theory is not sufficient in explaining the experimental observations. Based on M. Gudarzi's work [75], another set of forces that affect the stability is solvation forces. The parameters that affect solvation properties are the dielectric constant, refractive index, and the molecular size of the solvent [76][80]. All these properties are listed in **Table 2.1**, for referencing.

Table 2.1: Relevant solvent properties of water and 1-alcohols for graphene oxide dispersions

Solvent	Dipole Moment	Dielectric Constant (F/m)	Refractive Index	Molecular Size (Å)	Boiling Point (°C)	Viscosity (cP)
Water	1.85 D	80.10	1.333	2.75	100	0.89
Ethanol	1.69 D	24.5	1.361	4.4	78	1.07
1-Propanol	1.68 D	20.1	1.387	5.2	97	1.96
1-Butanol	1.66 D	17.8	1.399	6.5	117	2.57
1-Hexanol	1.65 D	13.3	1.418	8.9	158	4.59

M. Gudarzi implemented the solvent properties and predicted the energy minimums for a few common solvents for graphene oxide, as depicted in **Figure 2.11**, reproduced from [70].



The energy minimum for NMP, DMSO, and DMF are 20-40 times lower than the case of water, which means the solvation forces from water are not strong enough to overcome vdW forces, thus aggregation is expected. The colloidal stability in organic solvents is also due to the larger molecular size (compared to water) and also due to higher refractive index (compared to water) – since vdW interactions are screened in solvents with higher refractive indices, resulting in vdW interactions 2 times lower in organic solvents compared to aqueous system. Another important parameter is the polarity of the solvent, which is measured by the dielectric constant. Based on experimental data, there is a limit to “good solvents”, which means dielectric constants below 24 are not able to host stable colloids of graphene oxide [74][75], so the expectation is that the 1-alcohols do not form a stable dispersion.

There are controversial experimental data about the quality of graphene oxide dispersions in alcohols. V. Neklyudov *et al.* [78] performed theoretical simulations and experiments to offer some understanding of solubility factors of graphene oxide in solvents. He suggested based on simulation results that solubility of graphene oxide in solvents is a function of the chemical structure of graphene oxide and the solvent interface. Specifically, he studied the water, methanol and ethanol systems. He suggested that solubility of graphene oxide is afforded by the hydrogen bonding between solvent molecules and graphene oxide, which occurs through the tertiary alcohol functional groups. The strength of hydrogen bonds is highest in water, followed by methanol, then ethanol. In alcoholic graphene oxide solutions prepared by gradual solvent exchange, the solvent molecules do not interact directly with GO functionalities, but with the water molecules constituting the first coordination layer (i.e. the residual water from the washing procedure). Based on this finding, V. Neklyudov found that methanol and ethanol form stable dispersions.

3 Graphene Oxide Dispersions

3.1 Motivation

Based on the recently found chemical instability of graphene oxide in water, we look for alternative solvent systems for use in graphene oxide applications. The search for appropriate solvents that can enable large-scale commercial processibility of graphene oxide while preserving the native graphene oxide properties. The following are the solvent requirements:

- Low boiling point (i.e. high volatility)
- Low cost
- Low toxicity
- Inert chemical nature (i.e. no nucleophilicity)
- Stable dispersion for a large range of concentration (higher concentrations desirable) [32]
- Stable dispersion for a reasonable period of time [32]
- Able to maintain fully exfoliated state of graphene oxide (i.e. <5 layers)
- Able to maintain chemical integrity of GO, unlike GO in water

Alcohols meet most the requirements based on their properties; they are highly volatile, inexpensive, non-toxic, and inert. Researchers have briefly looked at alcohol systems for graphene oxide, but there was no consensus on the results. Thus, here we perform a systematic study into the family of low-molecular weight 1-alcohol solvents, namely ethanol, 1-propanol, 1-butanol and 1-hexanol, and compare these alcohol systems with the aqueous system to get a better understanding. **Table 2.1** provides the important properties dictating the polarity, thus dispersion stability, of these solvents. This will be a study first of its kind to look at the effects of the length of solvent in dispersion quality of graphene oxide. Based on this work, large scale commercial processibility of graphene oxide may be a step closer.

3.1.1 Objectives

The main objective of this study is to investigate the low-molecular weight 1-alcohol solvents as dispersing media for graphene oxide and characterize the resulting dispersions. More specifically, we aim to:

- Investigate processibility of graphene oxide in these solvent systems as a function of sedimentation and redispersion for a better understanding of large-scale processing capabilities
- Understand the solute-solvent interactions in the colloidal dispersion
- Inspect graphene oxide composition as a function of solvent system for a better understanding of chemical transformation in water and 1-alcohols

3.2 Experimental Design

3.2.1 Graphene Oxide Synthesis

The graphene oxide used in all the experiments was synthesized via the modified Hummer's method. In a typical reaction, 2 g of graphite (Alfa Aesar, -10 mesh, 99.9%) is added into a mixture of 240 mL of H₂SO₄ (Sigma-Aldrich, 95 – 98%), and 27 mL of H₃PO₄ (Sigma-Aldrich, extra pure, 85% solution in water) in a flask and stirred at room temperature. Then, 12 g of KMnO₄ (Sigma-Aldrich) is slowly added. Then, the mixture is transferred into an oil bath for an overnight reaction. After stirring for 16 h at 45 °C, the graphene oxide mixture is taken off the oil bath and cooled down to room temperature. Following, the mixture is transferred into 200 mL of water in an ice bath with slow stirring. Once temperature reaches 15 °C, 3-5 mL of 30% H₂O₂ (Sigma-Aldrich) is slowly pipetted into the beaker while stirring. Consequently, the color of the solution turns from dark brown to golden. The resulting mixture is centrifuged, supernatant removed, and the pellet re-dispersed in 10% HCl (Sigma-Aldrich) and centrifuged again. This process is repeated once more, followed by four washes through centrifugation with ethanol (Fisher Scientific) to remove the acids. For each run, the dispersion is centrifuged at 3500 rpm for 30 minutes. After the final ethanol centrifuge, the process of solvent exchange is initiated. The graphene oxide batch is divided into five parts, each part dispersed in a different solvent. The five solvents used for the solvent exchange are: water, ethanol, 1-propanol, 1-butanol, and 1-hexanol. The solvent exchange process consists of three iterations of centrifugation at 3500 rpm for 30 minutes. After the final centrifugation, the supernatant is discarded and replaced with

fresh solvent. These stocks are stirred before aliquoted for concentration measurements, which are measured in weight percent (wt%).

3.2.2 Graphene Oxide Colloidal Stability

Here, we want to distinguish between solubility and dispersibility of GO. GO dispersions are colloidal suspensions, where the GO particles are suspended in a solvent for a certain time span. GO cannot be solubilized in any solvents. Therefore, going forward, a GO dispersion refers to a colloidal suspension of GO in a solvent system. Dispersions in their true nature are thermodynamically unstable, however, they can be kinetically stable for a long time. Destabilization of dispersions result in creaming and sedimentation, where the difference in the density causes the dispersed state to rise or fall, respectively, as well as flocculation and coalescence, where the particle aggregates (i.e. increased particles sizes) reversibly or irreversibly, respectively [81]. By this definition, coalescence would cause the restacking of single layers of GO into multilayer structures.

To study colloidal stability means to understand the kinetic parameters of GO dispersions and to observe the destabilization mechanism. As mentioned earlier, dispersion properties like settling and aggregation depend on the overall interaction energy of each solvent system with GO particles (i.e. EL repulsion and vdW forces). Macroscopic properties of solvents, such as density and viscosity, also need to be considered for dispersion stability. Thus, we require our solvents to meet the following requirements regarding GO dispersions:

- Maintain stability for a reasonable period of time
- Maintain GO particle size, i.e. exfoliation state
- Reversible destabilization, such as sedimentation and flocculation are preferred over irreversible aggregation

The most important parameter for measuring dispersion stability is measuring the exfoliation state of GO; the ability to maintain a high percentage of single-layer GO flakes is imperative. In terms of destabilization mechanisms, we prefer sedimentation and flocculation over coalescence, since the former are reversible and can be easily dealt with.

To quantify stability of our GO dispersions in water and 1-alcohols, we use zeta (ζ) potential and liquid crystallinity properties of these dispersions. ζ -potential measures a kinetic parameter of colloidal stability, based on which we can get insight on stability time periods. Generally, zeta potential (ζ) of 0–10 mV suggests that the dispersion will be unstable, 10–30 mV will be slightly to moderately stable, 30–60 mV will have good stability, and <60 mV will have excellent stability for electrostatically repelling particles [32]. GO in water has a ζ -potential of -64 mV in water [34]. However, sterically stabilized particles can be stable without large ζ -potentials, like in the case of 1-alcohols. ζ -potentials of the organic GO dispersions have not been measured before.

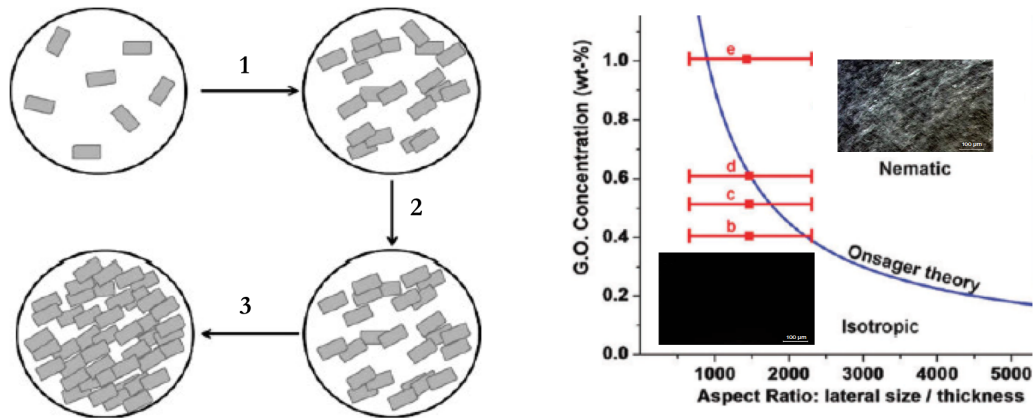
There are two types of cells, as shown below in **Figure 3.1**, reproduced from [82]. Here, ζ -potential measurement of aqueous samples is carried out in disposable capillary cells (**Figure 3.1a**) and approximated by the Smoluchowski model, while the measurements of non-aqueous media are carried out in the dip cell (**Figure 3.1b**) and approximated by the Hückel model [83]. The disposable capillary cell electrodes are farther apart, which helps to avoid electrolysis and bubbles during measurements of high conductivity samples (i.e. water). However, in non-aqueous samples, bubbles from electrolysis and Joule heating effects are less likely, thus having the cell electrodes closer helps to avoid applying large electric fields to get a good measurement. Thus, the dip cell is good for solvents with low dielectric constants (i.e. organics).



b

Dispersion stability can also be studied through an interesting property of GO dispersion, which is a macroscale alignment of the 2D GO flakes resulting in a liquid crystalline phase. This property is based on Onsager's theory, which predicts that colloidal dispersions of 1D rod-like and 2D plate-like

particles with high aspect ratios could go from an isotropic (disordered) phase to a nematic (ordered) phase when the dispersion reaches a critical concentration. As depicted in **Figure 3.2a**, when the concentration is low, there is no interaction between the particles and they can rotate freely [62]. With increasing concentration, the rotation of the particles is restricted due to the exclusion of free volume, thus the particles are forced to orient and align themselves [62]. This critical concentration required for the onset of liquid crystalline (LC) GO is strongly dependent on the aspect ratio of the platelets, as predicted by the Onsager theory (**Figure 3.2b**) [84]. LC phases are observed in aqueous and organic dispersions of GO which have added opportunities for designing 1D, 2D, and 3D highly crystalline microstructures, such as fibers, films and aerogels [74][79][80]. The LC GO structures have shown to outperform those obtained from non-LC GO dispersions [34].



Good colloidal stability of GO dispersion is critical for the formation of LC phases [62], thus the presence of LC phases imply dispersion stability. The transition from an isotropic to a nematic phase is evidenced by the appearance of birefringence under polarized light. Birefringence is a property of a



highly anisotropic material (such as aligned GO flakes) that refracts light in two directions. In **Figure 3.2b**, the insets show micrographs of GO dispersion under polarized light at low concentration (isotropic phase), where birefringence is absent, and at high concentration (nematic phase), where birefringence is observed. In a simple design with a pair of cross-polarizers, a regular torch light, and a webcam, set up as shown in **Figure 3.3a**, we created a platform to perform polarized light imaging (PLM) [85]. We used a white light torch to shine the light from behind. We have two polarizers placed on a cross-axis, with the GO dispersion placed in between. On the other end, we have a camera to capture the images. **Figure 3.3b** shows GO dispersion in 1-butanol without polarizers, and **Figure 3.3c** shows the dispersion with polarizers, where the shimmer that is observed are the liquid crystals. We utilize all the aforementioned experimental methods to verify stability of our GO dispersions in the following sections.

3.2.3 Solvent-Dependent Chemical Transformation of Graphene Oxide

Another important property of our 1-alcohol dispersions is to compare the solvent-dependent chemical transformation to compare to our aqueous dispersion. We observed the dispersions over time to see if there were any solvent-dependent changes. The various techniques that we used for characterization our dispersions before and after aging were: UV-vis absorption spectroscopy, Fourier transform infrared (FTIR) spectroscopy, thermogravimetric analysis (TGA), Raman spectroscopy, X-ray diffraction (XRD), and energy dispersive spectroscopy (EDS).

UV-vis absorption spectroscopy is commonly used to characterize GO dispersion quality in various solvents. UV-vis spectroscopy measures the absorbance of particular electronic transitions of GO in the ultraviolet and visible light regions. We utilize the Beer-Lambert Law to measure the absorption coefficient of GO dispersions based on the assumption that the conditions below are met:

- Low analyte concentration
- No light scattering from the attenuating medium

Low analyte concentration is required to ensure there is minimum solute-solute interactions, thus minimizing chemical deviation from the Law. Relatively low concentration is also required to ensure that the absorbance of light is below 90% (i.e. less than 1 on the absorbance scale) to ensure precise

measurement. Before each sample run, a blank run measures the background, which can be subtracted from sample run to get sample absorbance. Based on the Beer-Lambert Law, as follows:

$$A = \varepsilon lc \quad \text{Eq. 13}$$

where absorbance relates to the concentration of the analyte through a constant called the absorption coefficient, ε [mL of solvent/mg of GO/m or mg of solvent/mg of GO/m], and the cell pathlength, l [cm], set at 1cm for all the experiments here. The absorption coefficient is a characteristic property of the analyte in the respective attenuating medium tested in.

Similar to UV-vis spectroscopy, FTIR spectroscopy is a very common technique to characterize GO. IR spectroscopy is based on the fundamental properties of atoms joined by chemical bonds to absorb electromagnetic radiation in the $4000 - 400 \text{ cm}^{-1}$ frequency region [62]. Since GO has a complex mix of functional groups, the IR spectrum can get very convoluted. The peak assignments in the fingerprint region from $1000 - 400 \text{ cm}^{-1}$ is ambiguous. However, the peaks from $2000 - 1000 \text{ cm}^{-1}$ are well-known. FTIR can be done via two sampling techniques: transmission mode with a KBr pellet and attenuated total reflection (ATR). We used the former technique with the KBr pellets.

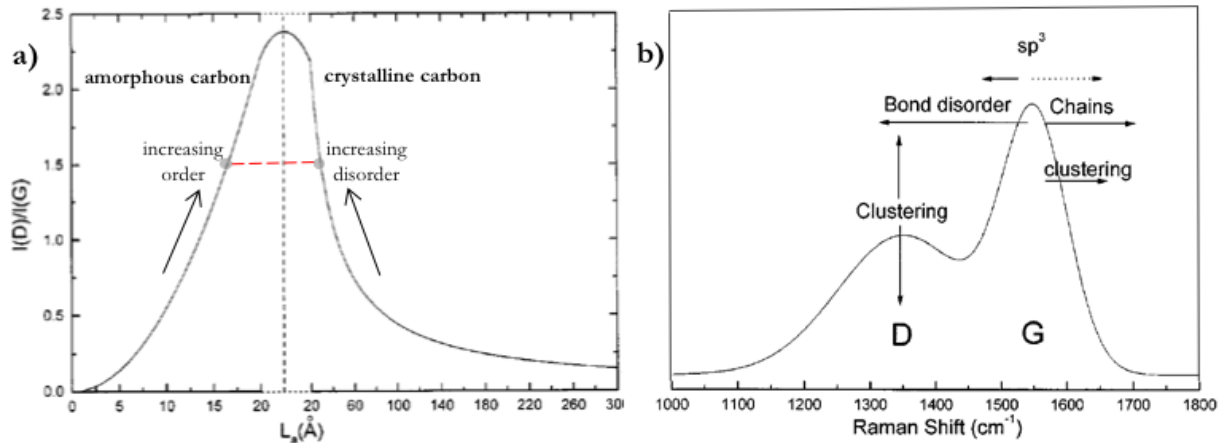
TGA is a method of thermal analysis in which physical and chemical properties of a material is tested as a function of temperature. In the case of GO, TGA provides quantitative information about thermal stability. With a high percentage of oxygen functionalities of GO, TGA should be run in an inert gas environment to ensure no re-oxidation. Here, TGA runs were carried out in a nitrogen atmosphere, with the following temperature profile:

- Ramp up to $100 \text{ }^{\circ}\text{C}$ at $10\text{ }^{\circ}\text{C}/\text{min}$
- Isothermal for 5 minutes at $100 \text{ }^{\circ}\text{C}$
- Ramp up from $100 \text{ }^{\circ}\text{C}$ to $450 \text{ }^{\circ}\text{C}$ at $10\text{ }^{\circ}\text{C}/\text{min}$

The isothermal step is to remove the adsorbed water from GO.

Raman spectroscopy is widely used with GO to characterize the level of disorder in the carbon lattice from the oxygen functionalities. In GO Raman spectrum, there are two prominent peaks, the D and G peaks at 1350 cm^{-1} and 1580 cm^{-1} , respectively. Our Raman spectra were obtained using a 532 nm laser from $400-3000 \text{ cm}^{-1}$. A common parameter used to characterize quality of GO is the I_D/I_G ratios. The relationship between the D and G peak is explained by Ferrari *et al.*, where they observe that the

ratio is dependent on the graphitic cluster sizes (L_a), and the sp^2/sp^3 content ratio [86]. As shown in **Figure 3.4a** reproduced from [86], the I_D/I_G ratio is a non-monotonic function of the graphitic cluster sizes, with the smaller cluster sizes (i.e., left side of peak) representing an amorphous or disordered carbon lattice, and the larger cluster sizes representing a more crystalline carbon lattice, such as graphite. The D peak arises from disorder in the aromatic rings, therefore in the case of graphite, with increasing disorder, the I_D/I_G ratio increases. With more disorder in the sp^2 lattice, the I_D/I_G ratio further increases, until the cluster sizes are so small that the ratio starts to decrease again. With an amorphous carbon material with smaller L_a , the D peak is proportional to the graphitic cluster size, so with increasing graphitic nature, the D peak increases. With an amorphous carbon lattice, such as GO, we can achieve smaller I_D/I_G ratios with thermal reduction or annealing. The G peak is related to the sp^2 hybridization of the lattice, which can shift due to introduced sp^3 hybridization and other types of bond disordered, as shown in **Figure 3.4b**. Generally, the I_D/I_G ratio of GO is low, due to a combination of high oxygen functionalities and smaller L_a , which means the lattice is mostly sp^3 hybridized.



XRD was used to characterize the crystallinity of our GO using concentrated slurries, and EDS was used to quantify the C/O ratio of GO as well as impurity content before and after aging.

3.3 Results and Discussion

3.3.1 Solution Processibility of Graphene Oxide Aqueous and 1-Alcohols Media



GO has a very complicated rheological response in aqueous media [87]. It is well known that GO gels in water due to the strong electrostatic interaction with water. This was evident during the solvent exchange process, where the centrifugation of GO in water became increasingly difficult after consecutive runs. **Figure 3.5** shows the GO dispersions in the dispersed state and centrifuged state. As seen in **Figure 3.5a**, the dispersed state of GO in water and 1-alcohols look similar, except for the darker color of aqueous dispersion. However, **Figure 3.5b** shows that in the centrifuged state, GO in the 1-alcohol systems have formed a concentrated pellet at the bottom of the tube, while in the water system, most of the GO is still dispersed in solution. This is due to the strong electrostatic interaction of graphene oxide in water, causing both long-range repulsion and gelation, which increases the viscosity of the dispersion and slows sedimentation. This gelation property implies a lower practical concentration for graphene oxide aqueous dispersions, which is not ideal for applications that require more concentrated graphene oxide slurries. Y. Shim *et al.* [80] noticed that GO dispersion in water turns gel-like around 1 wt%, so they added polymers that retard this transition and widen the working concentration. Adding polymers to the system creates an additional difficulty for when GO needs to be extracted or used for an actual application. The 1-alcohol solvent systems are not limited by this property, thus achieving concentrations as high as 8 wt% without gelation. The maximum concentration attainable for water in our experiments was 2.35 wt%. Maximum concentration achievable by centrifugation for each solvent is tabulated in **Table 3.1**.

Table 3.1: Maximum GO slurry concentration achievable by centrifugation in respective solvent systems

Solvent System	Concentration (wt%)
Water	2.35
Ethanol	7.28
1-Propanol	5.46
1-Butanol	7.28
1-Hexanol	8.24

For a GO dispersion to be useful, these essential criteria must be met: the GO must disperse in a solvent appropriate to the application, at a useful concentration, and remain dispersed over a reasonable period of time [32]. We have shown that 1-alcohols have capabilities for a larger range of workable concentration compared to water. Now, we study the colloidal stability of GO as a function of solvent.

3.3.2 Graphene Oxide Colloidal Stability

Based on the low dielectric constants, the 1-alcohol systems were theorized to not create stable dispersions [69], [70]. However, we observed dispersion stability in the 1-alcohols despite the low dielectric constants (Error! Reference source not found.) with 15 minutes of tip sonication at 75 mW of power. We observe stability in water and the 1-alcohol systems, except in 1-hexanol, where there is settling. The stability of GO colloids in the other 1-alcohols can be explained by a combination of factors: molecular size, dielectric constant, and the refractive index. The molecular size and refractive index are increasing with increasing 1-alcohol chain length while the dielectric constant is decreasing. Based on our observations, despite having the largest molecular size and refractive index, 1-hexanol is not able to host a stable colloid. This may be because 1-hexanol is not as polar as the other 1-alcohols. Dispersion stability of graphene oxide in water and 1-alcohols is shown in **Figure 3.6** at different concentrations: 0.01 wt% (**Figure 3.6a**) and 0.05 wt% (**Figure 3.6b**) after 24 hours of sitting.



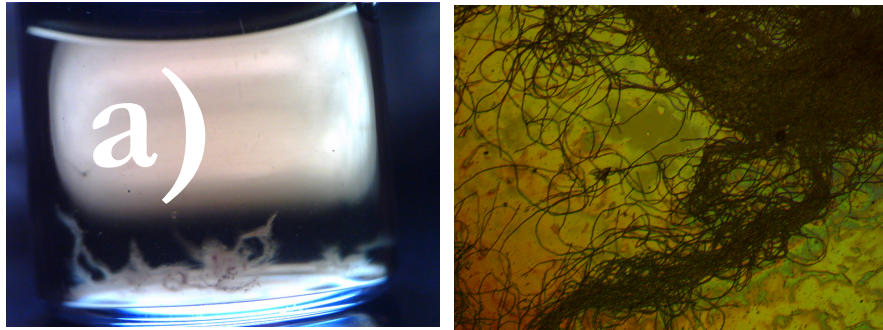
Based on our results as tabulated in **Table 3.2**, we observed similar ζ -potential for freshly sonicated aqueous GO dispersion of -62 mV, showing excellent stability. With the 1-alcohols systems, we observed on average that the ζ -potential values were lower than the aqueous system, ranging from -28 mV to -42 mV. However, the data had large standard deviation, which was probably due to the low mobility of GO in the organic solvents.

Table 3.2: Zeta potential values of graphene oxide dispersions in respective solvents

Solvent System	Zeta Potential (mV)	Standard Deviation
Water	-62	2
Ethanol	-32	21
1-Propanol	-42	31
1-Butanol	-28	29
1-Hexanol	-30	27

Even though freshly sonicated aqueous GO dispersions are extremely stable over short times, but as mentioned earlier, the solvation forces in water are not as strong, so irreversible aggregation is expected and observed over longer times, as shown in **Figure 3.7**. This type of aggregation is not reversible by mild agitation, like in the case of 1-hexanol, but could be reversed with stronger agitation, i.e. tip sonication. GO in 1-alcohols are stable for a reasonable amount of time and the destabilization is easily reversible, unlike in the case of water.

Figure 3.6: Colloidal stability water,

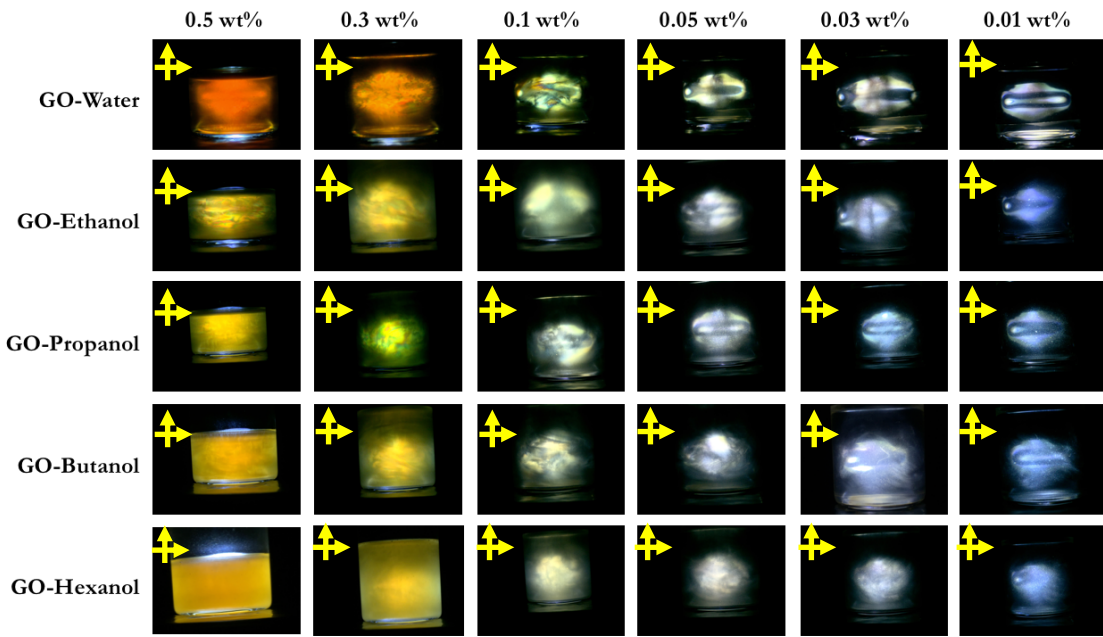


3.3.2.1 Liquid Crystalline Graphene Oxide

We tested a set of concentrations in all the solvent systems to determine the onset of LC phases as well as to look at the dispersion quality under the cross-polarizers. **Figure 3.8** shows the LC phases in each solvent, going from 0.5 wt% to 0.01 wt%.

We observed liquid crystals in all the solvents at all concentrations, except for the 0.01 wt% graphene oxide dispersion in water. Based on the Onsager theory, this would mean that the aspect ratio of the graphene oxide particles is smaller in aqueous dispersion, compared to the 1-alcohol systems. We ran dynamic light scattering (DLS) measurements with dispersions at 0.01 wt%, which were tip sonicated for 1 minute to ensure no large aggregated particles. DLS results (Table 3.3) confirmed that the graphene oxide flakes in water are smaller compared to the 1-alcohols. To remove solvent bias, we created a 0.01 wt% dispersion of aqueous graphene oxide flakes in ethanol, tip sonicated for 1 minute, and repeated DLS in ethanol, which gave the same result.

Figure 3.7: Aggregation of dried s

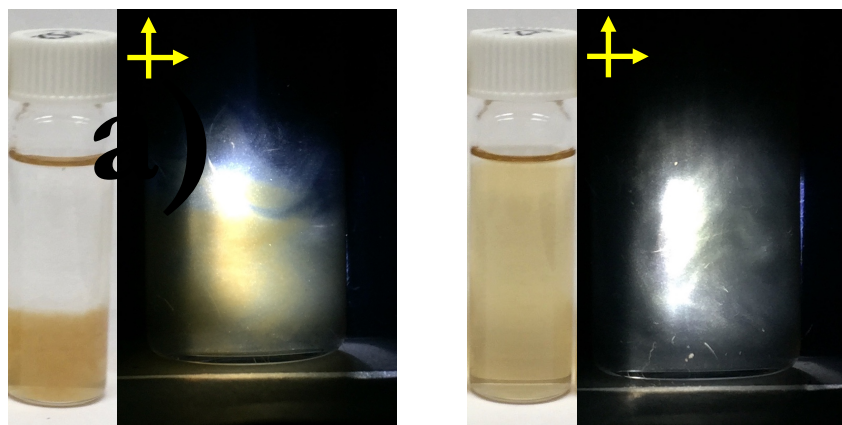


This size reduction has not been reported before, and we believe this is because of the chemical transformation induced by the water, which results in cleavage of larger flakes into smaller flakes over time. Smaller flakes have a lower aspect ratio, which pushes the onset of LC phases to higher concentrations, as observed in our polarized light imaging results. As a result, the onset of LC phase for water is observed at 0.03 wt% while for the 1-alcohols, it is observed at 0.01 wt%.

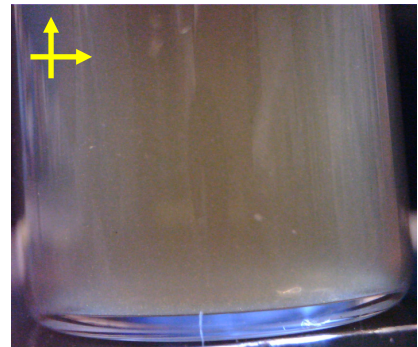
Table 3.3: DLS measurement data of average graphene oxide flake sizes in respective solvents

Solvent System	DLS (μm)
Water	0.4
Ethanol	3.6
1-Propanol	5.9
1-Butanol	3.3
1-Hexanol	3.5
Water in Ethanol	0.6

Another interesting observation was made in the case of 1-hexanol, where we witnessed some settling of graphene oxide in dispersion. Looking at the settled graphene oxide under cross-polarizers, LC phases were still present (**Figure 3.9a**), which is evidence that even though graphene oxide has settled, it is not aggregated, crumpled or wrinkled [88]. This observation further demonstrates the point that 1-alcohols are good solvents as they do not cause graphene oxide aggregation. Graphene oxide may settle, but with mild shaking, we observe that the dispersion looks the same as before. **Figure 3.9b** shows 1-hexanol dispersion after mild shaking, where we still observe LC phases. This shows that the destabilization mechanism in 1-hexanol is reversible, therefore it may either be flocculation or sedimentation.



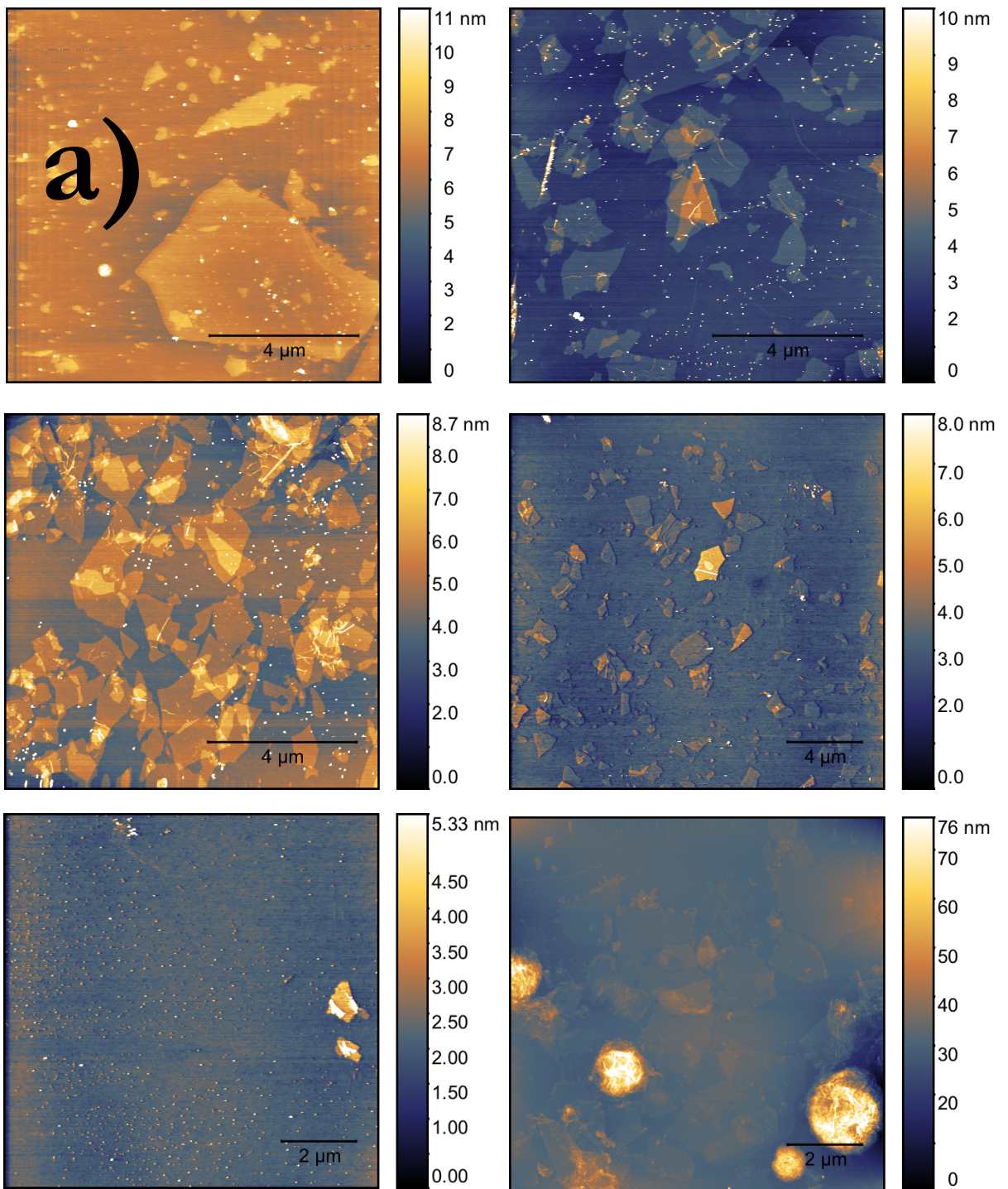
For comparison, we also looked at spray dried graphene oxide, which is different from our solvent exchanged graphene oxide. The spray dried graphene oxide has been characterized to be highly crumpled, due to the spray drying mechanism [89]. The expectation is that under the cross-polarizers, even at high concentration, the LC phases will be absent. **Figure 3.10a** shows spray dried graphene oxide freshly dispersed and sonicated in ethanol. **Figure 3.10b** shows the dispersion without the cross-polarizers, and **Figure 3.10c** with the cross-polarizers. As expected, the spray dried dispersion looks cloudy, not shimmery. Therefore, the liquid crystals were absent in the crumpled graphene oxide dispersions.



b)

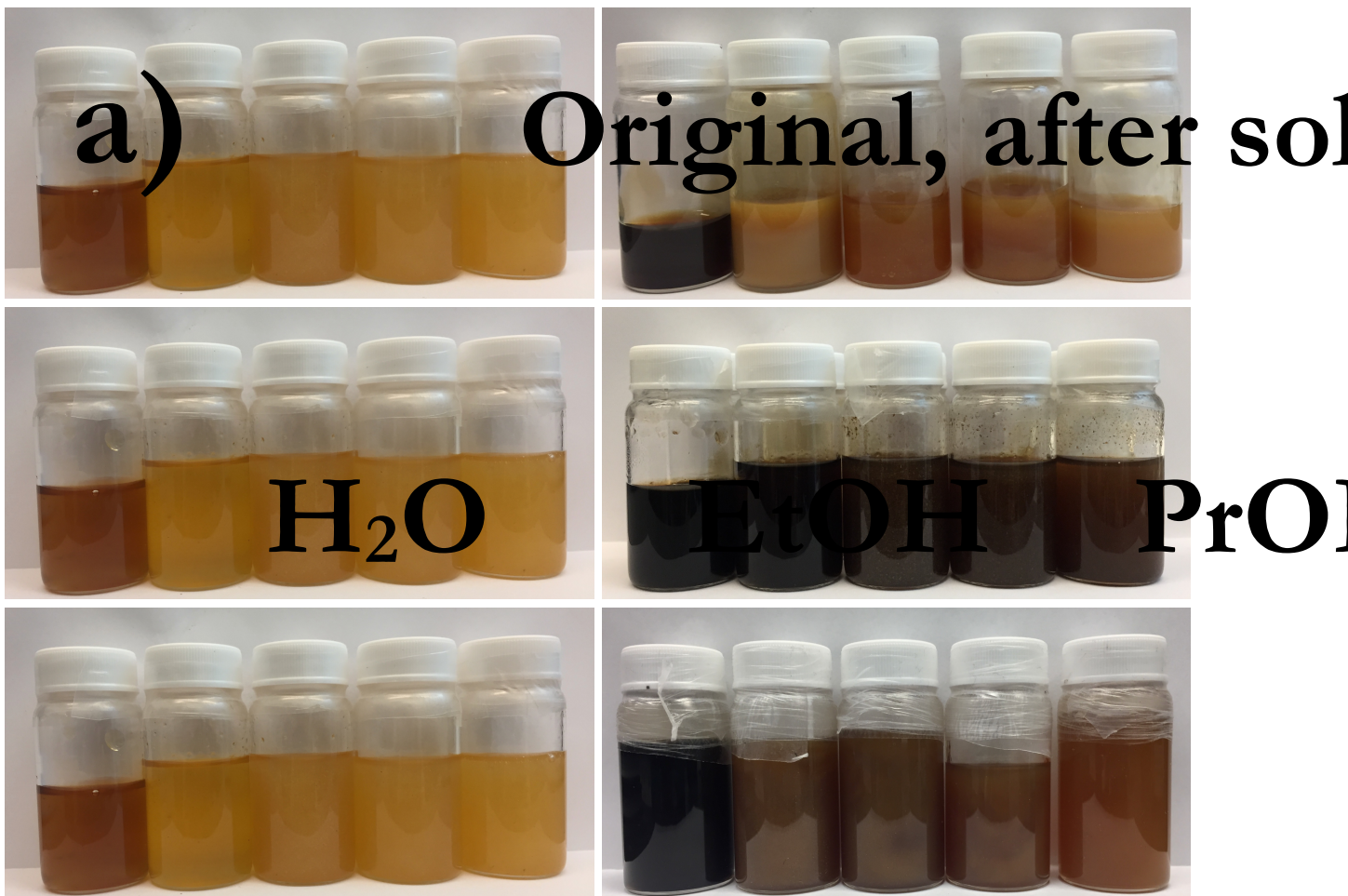
We also collected atomic force microscopy (AFM) micrographs to look at the exfoliation state of graphene oxide sheets in water and 1-alcohols and compare it to the spray dried graphene oxide system. Based on the AFM micrographs (**Figure 3.11a-e**), we observed most of the flakes in the water and 1-alcohol systems are flat, uncrumpled, and single layer with a thickness of 1 nm. In the case of spray dried graphene oxide (**Figure 3.11f**), we observe a mix of crumpled graphene oxide balls and flat sheets. The samples were prepared by spin-coating dilute dispersions on ozone-treated silicon wafers. As observed in **Figure 3.11e**, the spin-coated sample from 1-hexanol is not as dense as the other films produced from other 1-alcohols. This is due to the wettability issue of 1-hexanol and the silicon wafer. All the results with zeta potential, polarized light imaging, and AFM show that the 1-alcohols are good solvents for graphene oxide, and should be further studied.

Figure 3.10: a) Spray dried gra
without cross-polarizers, an⁴⁰



3.3.3 Solvent-Dependent Chemical Transformation of Graphene Oxide

Water, like other polar aprotic solvents spontaneously exfoliate graphite oxide and induce chemical transformation of GO, which results in an obvious color change from orange to dark brown, as shown in Error! Reference source not found.. There are two factors that affect the color change; water exposure and light exposure. The images in the left column (**Figure 3.12a,c,e**) show the color of dispersion at the end of the solvent exchange process after washing (i.e. the starting point of the dispersion).

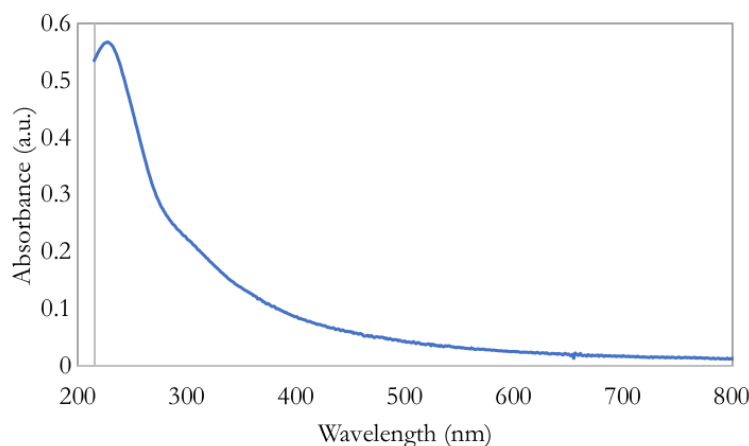


Even at this point, the chemical transformation of graphene oxide in water has begun and already changed the dispersion color. The images in the right column (**Figure 3.12b,d,f**) show the dispersions at different times and settings. **Figure 3.12b** is of the stocks covered in aluminum foil for 2 months,

which shows that the aqueous dispersion darkened considerably while the 1-alcohols maintained the same color. This demonstrates that GO in water continues to react and undergo chemical transformation. **Figure 3.12d** is of the stocks that were exposed to direct light for 2 weeks, which shows a color change in all the solvents. This illustrates that graphene oxide can undergo chemical transformation even in polar protic solvents, when exposed to light. **Figure 3.12f** is of the stocks that were sitting on the shelf in a box for 10 months with slight exposure to light. Here, we observe that the aqueous dispersion changed as it did in the previous cases, however, the 1-alcohol dispersions changed in color only slightly. We attempt to quantify these changes with UV-Vis spectroscopy and FTIR spectroscopy.

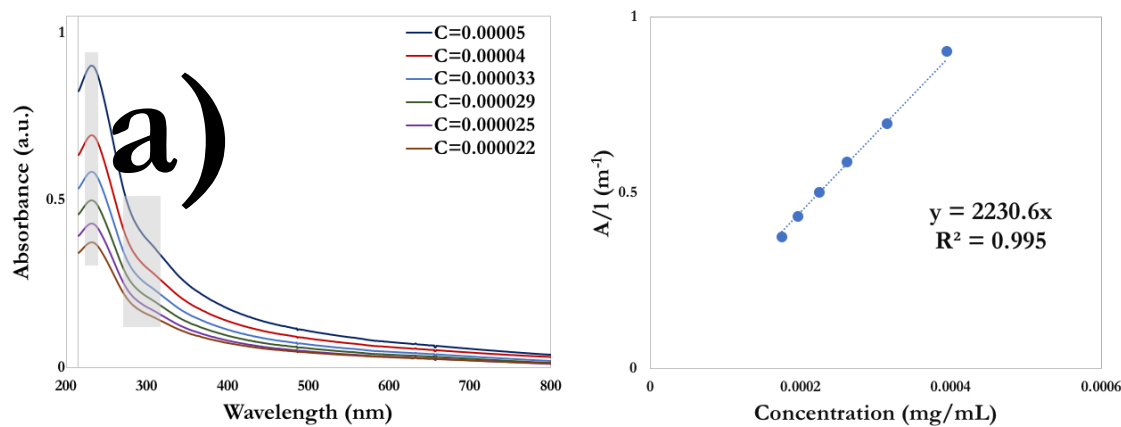
3.3.3.1 UV-Vis Analysis of Graphene Oxide Dispersions

The most prominent feature in the UV-vis spectrum of GO is a $\pi \rightarrow \pi^*$ electronic transition common for aromatic C=C bonds, which occurs around 230 nm [62]. In addition to the main peak at 230 nm, there appears a shoulder around 300 nm in the spectrum of GO prepared by modified Hummer's method, as shown in **Figure 3.13**. This peak is attributed to the $n \rightarrow \pi^*$ transition in the C=O bonds of oxygen-containing functional groups.

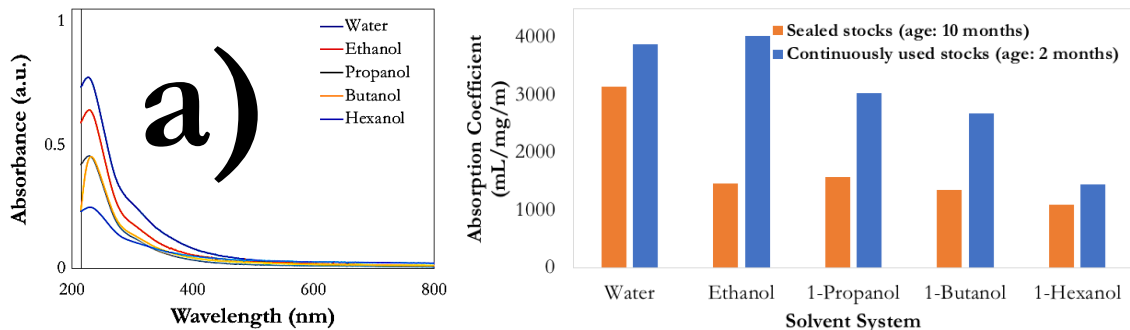


We performed a concentration study with all the solvents to tabulate the absorption coefficient of GO in the respective solvent systems. Using UV-vis spectroscopy, we can get insight on the relative dispersibility of GO in solvents by looking at the peak absorbance values. Solvents with higher GO dispersibility (i.e. better dispersion) have a higher absorbance value at the same concentration. Based

on Beer Lambert Law, higher absorbance means higher number of moieties in solution responsible for the absorbance. **Figure 3.14a** shows absorbance vs. wavelength spectra of GO in ethanol as a function of concentration, the 230 nm peak and 300 nm shoulder are highlighted. The absorbance values at 230 nm were plotted with respect to concentration to get the absorption coefficient at 230nm (**Figure 3.14b**). The absorption coefficient is different at different wavelengths and can be easily calculated using the same absorbance vs. wavelength curves. In this example, the absorption coefficient of graphene oxide in ethanol at 230 nm is calculated to be 2230.6 mL/mg of GO/m. The absorption coefficients of GO dispersions in water and 1-alcohols have not been measured, the closest data available in the literature is of graphene oxide dispersed in NMP, which has an absorption coefficient of 2460 mL/mg/m at 660 nm [90].



Based on our experiments, we observed the same characteristic spectrum in all the solvents, as shown in **Figure 3.15a**. The presence of the peak at 230 nm in the absorbance spectra is evidence of dispersion capabilities of all solvents, which again proves that 1-alcohols are able to disperse graphene oxide to an extent. When measured at the same concentration, the absorbance values go from highest to lowest in the following order: water, ethanol, 1-propanol, 1-butanol, 1-hexanol. This trend suggests that water has the highest dispersibility, while 1-hexanol has the lowest. The absorption coefficient depends on the wavelength of light, the solvent, and GO aging. **Figure 3.15b** shows a bar graph of absorption coefficients at 230 nm of each solvent system in two conditions; the orange set is of the sealed stock (**Figure 3.12f**), and the blue is of the stocks that were continuously used. The continuously used stocks have a higher absorption coefficient compared to the dispersions that were sealed.



All the sealed 1-alcohols have similar absorption coefficient, except for water. This illustrates the same observation about water continually reacting with and transforming GO even when sealed. Regarding the 1-alcohols sealed stocks, 1-propanol has the highest absorption coefficient and 1-hexanol is the lowest. However, with continuous use, the absorption coefficients of the 1-alcohol systems change. These changes seem to be a function of water-miscibility of the solvent, i.e. the more water-miscible solvents undergo a larger change. For example, the largest change is observed in ethanol, in which the absorption coefficient goes from 1458 mL/mg/m (sealed) to 4020 mL/mg/m (used), whereas the 1-hexanol only changes from 1100 mL/mg/m (sealed) to 1452 mL/mg/m (used). Water-miscibility decreases as the alcohol length increases, making the longer 1-alcohols less affected by moisture in air when the stocks are open and in use. **Table 3.4** presents the absorption coefficients of each set of stocks.

Table 3.4: Absorption coefficient of all solvent stocks in sealed and continuously used conditions

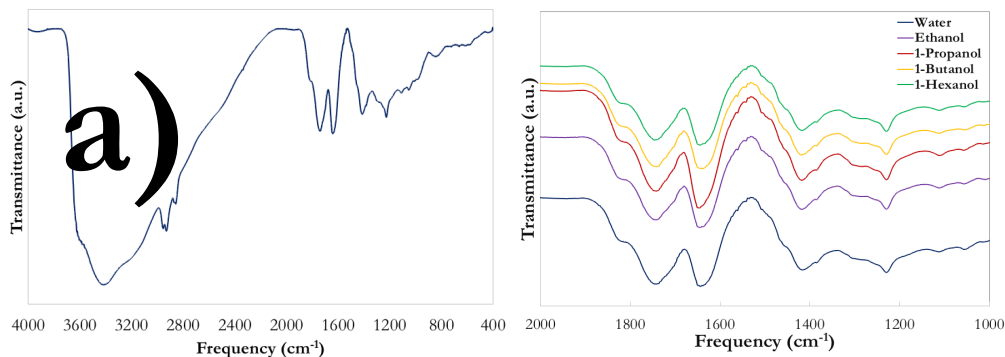
Solvent	Sealed Stocks	Continuously Used Stocks
Water	3151	3877
Ethanol	1458	4020
1-Propanol	1575	3038
1-Butanol	1358	2682
1-Hexanol	1100	1452

As expected, GO in water has a much higher absorption coefficient in both sealed and continuously used stocks, because water constantly reacts with GO and induces chemical transformation despite minimal light and moisture exposure.

Figure 3.15: a) UV-Vis s
absorption

3.3.3.2 FTIR Analysis of Graphene Oxide Dispersions

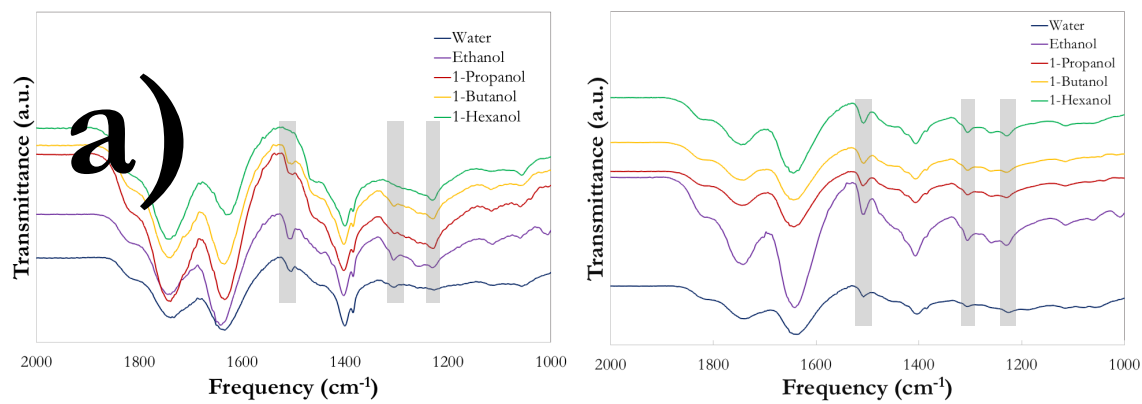
Figure 3.16a shows the full IR spectrum of graphene oxide in water, the largest peak in the $3600 - 2400 \text{ cm}^{-1}$ originating from the stretching of O-H groups; from graphene oxide tertiary alcohols as well as from the adsorbed water molecules [62]. The prominent IR peaks for graphene oxide in the $2000 - 1000 \text{ cm}^{-1}$ are: 1750 cm^{-1} , 1650 cm^{-1} , 1420 cm^{-1} , and 1227 cm^{-1} , which are attributed to C=O, C=C, deformation of C-OH and C-O-C, respectively. **Figure 3.16b** shows magnified spectra of the water and 1-alcohol systems, pointing out the four main peaks in the $2000 - 1000 \text{ cm}^{-1}$ region. As mentioned before, a gradual change in the graphene oxide composition that correlates with the UV-vis changes is observed in the FTIR spectra. Basically, the chemical aging is evident from the following changes: the peak at 1227 cm^{-1} starts to disappear, which indicates that the first functional groups to



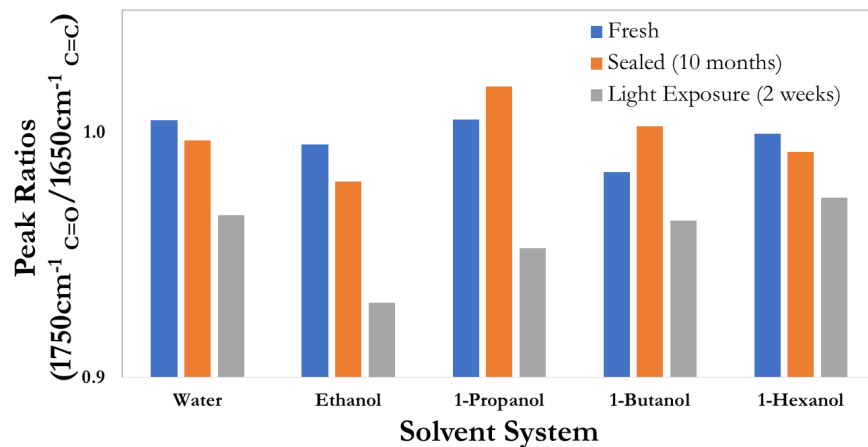
leave are the epoxides, and two new peaks emerge at 1500 cm^{-1} and 1300 cm^{-1} . Both of these emerging peaks are indicative of more graphitic structure (C=C), as predicted in **Figure 2.10** by the reaction mechanism.

Figure 3.17a show the spectra of the 10-months-old sealed stocks (**Figure 3.12f**) that display the 1500 cm^{-1} and 1300 cm^{-1} in water, ethanol, 1-propanol, and 1-butanol, but not at all in 1-hexanol. Similarly, the peak at 1227 cm^{-1} in water has disappeared, but it is still present in the 1-alcohols. At this stage, the water has achieved a significant chemical transformation, while the ethanol, 1-propanol, and 1-butanol have begun to change due to the light exposure. However, 1-hexanol has maintained its native properties. These observations are in agreement with the UV-vis data. After 2 weeks of exposure to light, the water and 1-alcohol stocks (**Figure 3.12d**) all experience the same extent of chemical transformation, which also supports the UV-vis findings. As seen in **Figure 3.17b**, water and 1-

alcohols all have the 1500 cm^{-1} and 1300 cm^{-1} peaks present, while the 1227 cm^{-1} has begun to disappear.



FTIR is almost purely qualitative. However, we can draw some semi-quantitative conclusions from peak ratios of each sample if compared to itself. Based on the analysis, we observe an interesting trend with the ratio of the peaks at 1750 cm^{-1} and 1650 cm^{-1} , which correspond to C=O and C=C bonds, respectively. As displayed in **Figure 3.18**, the ratios are approximately around 1 with fresh graphene oxide in all solvents. However, with the chemical transformation induced by solvent and light exposure, the ratio of $1750\text{ cm}^{-1}/1650\text{ cm}^{-1}$ decreases, which indicates that either the number of C=C bonds are increasing or the number of C=O bonds are decreasing. This, as predicted by the chemical transformation reaction, means either an extension of conjugated aromatic areas or conversion of tertiary alcohols into ketones, or both.



3.3.3.3 Study of Other Aspects of Graphene Oxide Dispersions

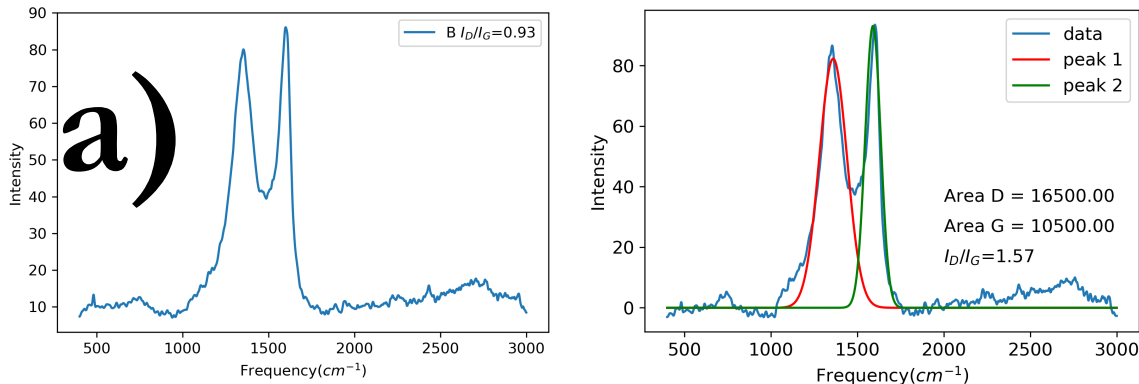
EDS was used to look the C/O ratio of GO as well as impurity content. **Table 3.5** presents the elemental atomic wt% and C/O ratio of GO obtained from freshly made stocks at 10kV of acceleration voltage. The table also presents the C/O ratio of samples that were exposed to light for 2 weeks. We observe that GO samples start off with a lower C/O ratio, which increases after the 2 weeks of light exposure. This data is also in agreement with our previous findings, where we observe a higher carbon content. On average, the C/O ratio of fresh samples were around 1.8, which went up to 2. All GO stocks contain about 1 wt% of elemental sulfur, which is expected from modified Hummer's GO, due to covalent bonding of sulfur from sulfuric acid during synthesis that is very difficult to remove by washing [72].

Table 3.5: EDS-based C/O ratios of fresh and 2-weeks-old light exposure stocks

Solvent	Fresh – Atomic Weight (%)			C/O Ratio	
	C	O	S	Fresh	2-Weeks-Old
Water	64.4±0.7	34.3±0.7	1.3±0.3	1.88	1.96
Ethanol	65.9±1	33.1±1	1.0±0.1	1.99	1.87
1-Propanol	64.0±0.3	35.4±0.5	0.7±0.1	1.81	1.94
1-Butanol	63.4±0.6	35.7±0.4	1.0±0.1	1.77	1.82
1-Hexanol	65.9	33.3	0.8	1.8	2

We used Raman spectroscopy to characterize the level of disorder in the carbon lattice from the oxygen functionalities. As mentioned earlier, the ratio between the D and G peaks at 1350 cm^{-1} and 1580 cm^{-1} , respectively, gives more insight into the structure of the carbon. I_D/I_G ratios can be obtained either by taking peak intensity values or peak area. Raman spectrum of GO in 1-butanol is shown in **Figure 3.19**, with I_D/I_G ratios calculated using the peak heights (**Figure 3.19a**) and by deconvoluting the peaks using two gaussians (**Figure 3.19b**).

I_D/I_G ratio obtained by taking the peak max values gives 0.93 and the peak areas gives 1.57. We believe the peak integral values provide more information, because it takes the width of the peak into account, which is sensitive to the number of different types of defects and oxygen functionalities, which each slightly change the peak positions and contribution to peak breadth. **Table 3.6** presents the I_D/I_G ratios of fresh GO dispersions and GO that was exposed to light for 2 weeks. Our results indicate



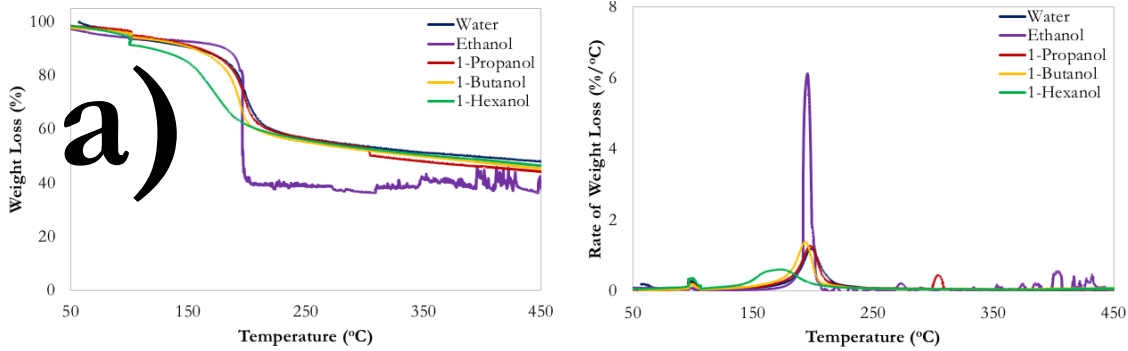
that the 2 weeks of light exposure increases the I_D/I_G ratio. The average I_D/I_G ratio of fresh GO is 1.5, which goes up to 1.9 after 2 weeks of light exposure. As was illustrated in **Figure 3.4a**, when L_a is smaller than 2 nm, which is likely the case for fresh GO where every 1.5 carbon is bonded to an oxygen, an increase in the ID/IG ratio reflects an increase in the size of the aromatic domains (i.e., L_a).

Table 3.6: I_D/I_G ratios of all fresh and 2-weeks-old GO dispersions using peak heights and gaussian fits

Solvent	Fresh		2-Weeks-Old	
	Height Ratio	Area Ratio	Height Ratio	Area Ratio
Water	0.94	1.63	0.93	1.92
Ethanol	0.92	1.48	0.96	2.02
1-Propanol	0.91	1.48	0.98	2.07
1-Butanol	0.93	1.57	0.93	1.78
1-Hexanol	0.95	1.58	0.95	1.81

TGA and XRD were used to examine the thermal stability and crystallinity of GO dispersions. These techniques were not sensitive to the aging, thus we only present data for the fresh GO. The TGA runs followed the temperature profile discussed in 3.2.3. As shown in **Figure 3.20**, the 1-alcohols and water GO dispersions have similar thermal stability, where two peaks of mass loss are observed, the first at 100 °C due to the loss of adsorbed water and the second around 150-200 °C due to the decomposition of oxygen-containing functional groups [38].

Figure 3.19: Raman spectra



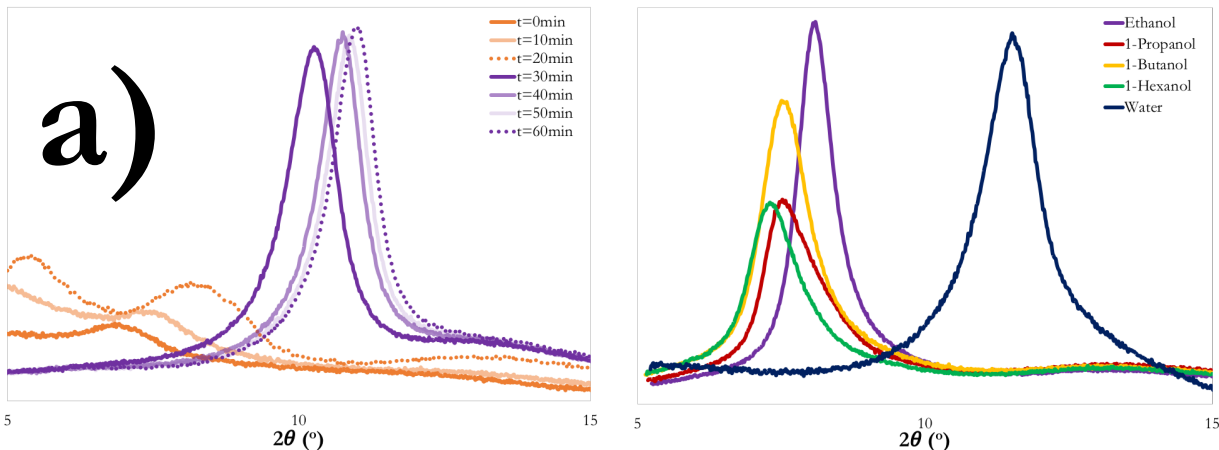
We observed that there were slight differences in the thermal stability of the various solvent systems. At 180 °C, GO from water had the least weight loss, followed by 1-propanol, 1-butanol and 1-hexanol, as calculated and presented in **Table 3.7**. The onset of the highest rate of weight loss was earlier in the case of 1-hexanol, suggesting that 1-hexanol has the least thermal stability. This may be due to the higher oxygen content in 1-hexanol compared to others in addition to the solvent properties.

Table 3.7: TGA weight loss of all fresh GO dispersions at 180 °C and 450 °C

Solvent	Residue at 180 °C (%)	Residue at 450 °C (%)
Water	85.99	45.8
Ethanol	90.51	38.81
1-Propanol	85.53	41.77
1-Butanol	82.98	42.7
1-Hexanol	68.81	43.88

XRD was used to characterize the crystallinity of our fresh dispersions using concentrated slurries. An interesting property of the water and 1-alcohol dispersion systems was observed with XRD during drying the GO slurries. For example, in the ethanol slurry, we observed that the GO peak around 10° did not show up until the slurry had dried and became more concentrated (i.e. t=30 minutes of drying), as shown in **Figure 3.21a**. At lower concentrations of the slurry, we observed peaks at lower angles, indicating a looser crystalline structure, where ethanol is still adsorbed on the surface of GO, and only after sufficient drying, the GO restacked. The final interlayer spacing from each solvent system was measured after the GO peak stopped shifting (i.e. fully dried state). At this state, we still observed a difference in the interlayer spacing of GO, indicating some adsorbed solvent molecules that are difficult to remove, even after 3 days of drying in the vacuum oven with no heat.

Figure 3.20: Thermal analysis



As shown in Figure 3.21b, GO dried from water has a much smaller interlayer spacing compared to the 1-alcohols. Interlayer spacing of GO from 1-alcohols increase based on the length of the 1-alcohol solvent, as tabulated in Table 3.8. 1-Propanol and 1-butanol systems have approximately the same interlayer spacing. This has been observed with water, methanol, and ethanol, where films dried from ethanol have a larger d-spacing compared to methanol. This is because the water and alcohol molecules interact with the GO functional groups and a layer of these solvent molecules strongly adhere onto the surface. Even in the fully dried state, the GO membrane has a layer of solvent molecules in between each flake, causing a difference in the d-spacing.

Table 3.8: XRD measured peak values and corresponding interlayer spacing for each GO dispersion

Solvent	Peak 2θ Value (°)	D-Spacing (Å)
Water	11.28	7.84
Ethanol	8.09	10.93
1-Propanol	7.51	11.76
1-Butanol	7.50	11.78
1-Hexanol	7.31	12.09

These XRD data prove that the resulting GO films from the different solvent systems will have a different interlayer spacing. The simplest way to tune our membrane interlayer spacing is to form vacuum-filtered films from these various dispersion systems, which are discussed later.

3.3.4 GO Aging Model

Based on all the properties of GO dispersions discussed in this chapter, we come up with a systematic model of GO aging as a function of starting material, dispersion solvent, and moisture and light exposure.

From our UV-vis and FTIR data, we observed that water adsorption and light exposure have a coupled effect on GO aging. In terms of properties, aging refers to a change of dispersion color from yellow to brown, an increase in the UV-vis absorption coefficient at 230 nm (presence of more C=C bonds), loss of oxygen functionalities (1227 cm^{-1} peak) and emergence of more graphitic structure (1500 cm^{-1} and 1300 cm^{-1} peaks).

Based on our results, we believe that aging of GO occurs via two routes: water exposure, and light exposure, both of which result in similar chemical changes. First off, in the case of GO dispersed in water and 1-alcohols, we observe a similar $1750\text{ cm}^{-1}/1650\text{ cm}^{-1}$ ratio of approximately 1. This, in addition with the overall FTIR spectra, suggests a similar starting point for all GO dispersions. With the sealed 10-months-old stocks, we observe that the absorption coefficient of GO-water is much higher than the 1-alcohols, and the $1750\text{ cm}^{-1}/1650\text{ cm}^{-1}$ ratio has decreased. This suggests that we have more graphitic structure in water compared to 1-alcohol dispersions that are of the same age. This is further established with the DLS and AFM data, where we observe smaller flake sizes in GO-water compared to all other systems. This development implies that the reaction between GO and water molecules result in cleaving GO flakes. With the water exposure, since the longer-chain alcohols are more water-immiscible, GO in 1-hexanol, for example, is seen to age less, based on the absorption coefficient values and the FTIR spectra. We observed that ethanol had aged the most, followed by 1-propanol, 1-butanol, and 1-hexanol. Some of the oxygen functionalities had disappeared in ethanol, but they were still present in 1-hexanol. However, with the light exposure, GO aging seems to be about the same in all 1-alcohols solvents. Therefore, when comparing the two competing factors, light has a stronger and more sudden effect compared to water exposure.

3.4 Conclusions

In this chapter, we have performed a comprehensive study of graphene oxide dispersion properties in aqueous and 1-alcohols systems. First, we showed with our centrifugation results that separation (i.e., sedimentation) of GO in 1-alcohols is not an issue as it is in water. With this, we prove an advantage of the alcohol system over aqueous system when it comes to solution processing of GO.

We also investigated colloidal stability of these dispersions by means of zeta potential and observation of liquid crystalline phases. We observed that GO is stable in water, however, due to the lowered solvent screening as predicted by the smaller energy minimum, GO flakes started to aggregate irreversibly. We observed in the 1-alcohols systems that GO is stable without any noticeable aggregation, however, some settling was observed in 1-hexanol, which was easily reversed with mild shaking. For the first time, we also observed LC phases in the 1-alcohols systems, which signifies that the GO flakes are not crumpled or wrinkled. This observation was confirmed with the use of AFM.

In our experiments, we confirmed the chemical transformation of aqueous media and were able to quantify this chemical transformation with UV-vis and FTIR. We showed that exposure to moisture and light can trigger a similar chemical transformation in the 1-alcohols systems. However, the 1-alcohol dispersions, once sealed and placed in a dark cupboard, maintain their native state, unlike aqueous dispersions, which are observed to undergo continuous transformation.

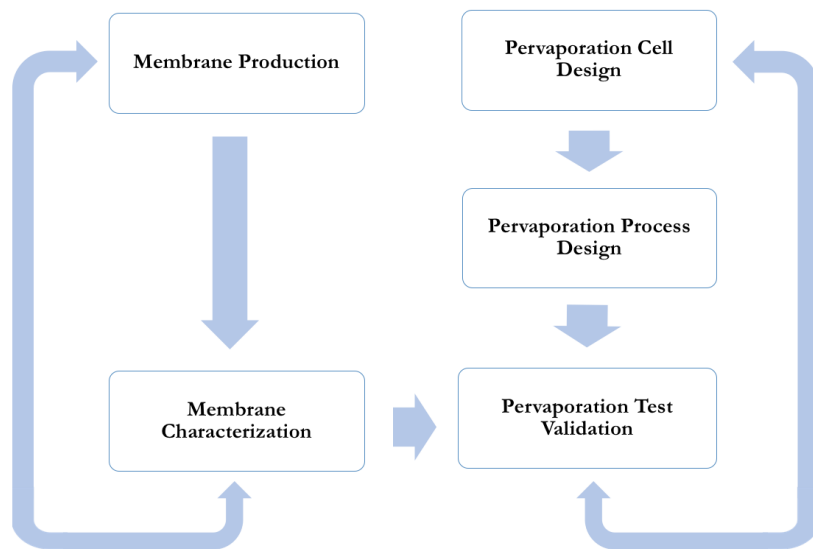
Overall, we have successfully shown that low-molecular-weight 1-alcohols are suitable media for dispersing graphene oxide. In doing so, we have improved the possibility of solution processing of graphene oxide for large-scale commercial applications.

4 PV Module and Membrane Design

4.1 Introduction

In a membrane-based separation process like PV, there are two fundamental parts of the research: i) membrane and ii) PV module, which are both studied in this thesis. Both aspects of the research underwent iterations following **Figure 4.1**, in order to properly optimize the entire system to get reliable results.

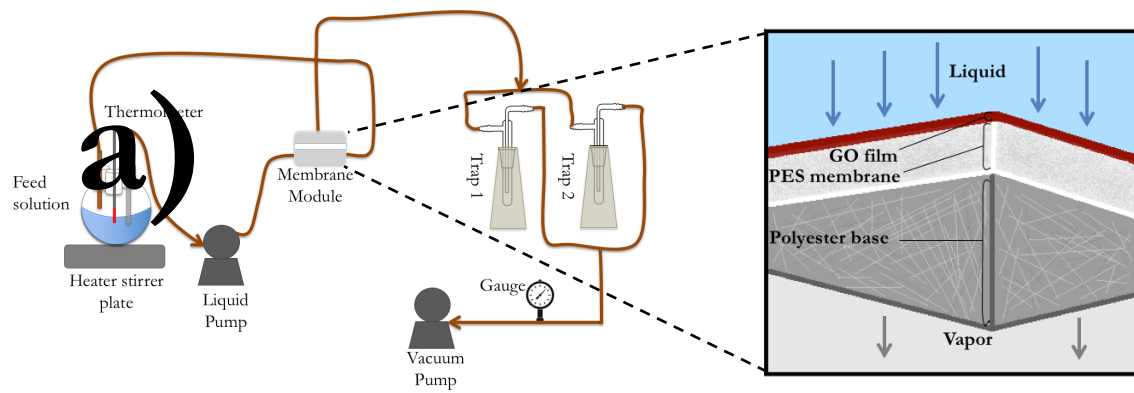
With regards to the PV module, we designed the membrane cell followed by designing the entire process, which includes other components, such as feed pump, condensers, and vacuum pump, etc. Membrane production was done simultaneously, which was used to validate the PV module. Based on the test results, the membrane, the membrane module and the entire process design were optimized and re-validated.



In this chapter, we will discuss the design of the PV module and validation tests as well membrane performance and optimization.

4.2 Pervaporation Module Optimization

In PV, the important parts of the setup include: a peristaltic pump to flow the feed across the membrane, a membrane module to hold the membrane, a vacuum pump, vacuum gauge, and condensers for permeate collection. In our optimization process, we ran multiple iterations of our setup and found ideal conditions for the heating of the feed, maintaining the temperature, sampling time, condenser capacities, and vacuum levels, etc. Optimization of the membrane module and vacuum levels were extremely crucial in obtaining reliable data from our setup. **Figure 4.2a** shows the



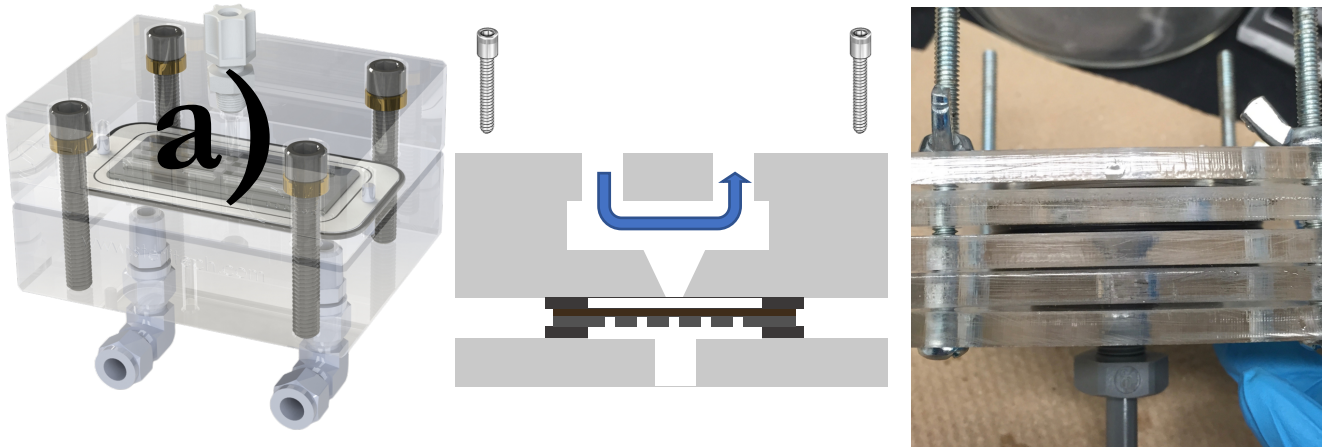
PV setup with parallel condenser layout, and **Figure 4.2b** shows inside the membrane module, where the membrane is contact with the liquid feed on one side and the vacuum on the other side.

4.2.1 Iterations of the Membrane Module

As shown in **Figure 4.2b**, the membrane module holds the membrane, where the feed is in contact with the active layer side of the membrane, and the vacuum is connected to the opposite end. The feed flows across the face of the membrane with the use of the peristaltic pump. The peristaltic pump is required to be circulating the feed at a fast-enough speed so that the temperature is maintained at the membrane surface.

Our first membrane module design was based on the Sterlitech CF042A cross-flow cell made from clear cast acrylic, as shown in **Figure 4.3a** with the appropriate membrane sizes [91]. We designed and built our homemade version using a CO₂ laser to cut pieces and the machine shop for machining

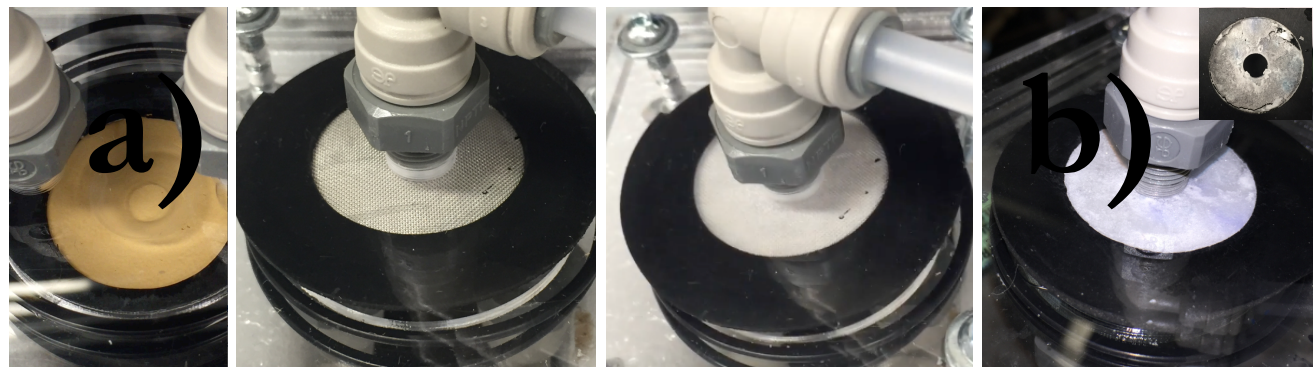
parts. Each piece of acrylic is sealed with O-rings and tightened using screws. This is sufficient for getting a good seal because PV operates under low pressures. The only requirement for this setup is for it to maintain a high vacuum level, which can be ensured with the use of a good vacuum pump and O-rings. The cross-section of the module can be seen in **Figure 4.3b**, the inlet (feed) and outlet (retentate) of the liquid feed at the top, the feed reservoir inside the module, the cone to guide the flow onto the membrane. The membrane is sandwiched between two gaskets and a metal mesh support. The fully assembled cell with a GO membrane is shown in **Figure 4.3c**.



Having a clear acrylic module helped us to get a better understanding of PV dynamics. On the feed side, we learned about the flow dynamics and on the permeant side, we learned more about membrane and permeate dynamics. The feed and permeant side are depicted in **Figure 4.4a** and **Figure 4.4b**, respectively, where the GO active layer faces the feed flow, and a metal mesh support is used on the permeant side to provide mechanical support against the vacuum.

With the use of clear acrylic cell, we observed that with the combination of low-pressure flow and the conic design, there is limited feed circulation on the membrane, which could potentially result in concentration polarization. In addition to that, we observed air bubbles on the membrane as the feed was being pumped into the membrane module. Air bubbles on the surface of the membrane are not desirable because it hinders permeation and results in unwanted fluctuations in flux.

On the permeate side, issues that were observed were condensation and leakage. Early stage condensation looks like fog on the clear acrylic, as shown in **Figure 4.4c** (comparing to **Figure 4.4b** as the no condensation state). This was observed when the vacuum valve was shut for longer than 30 seconds. With the vacuum valve shut, the water vapor on the permeant side cannot escape, thus starts to condense on the acrylic wall. If this condensation is not taken care of immediately by reopening the vacuum valve, the pressure drops across the membrane and the permeate start condensing inside the membrane. This exposes liquid water to the vacuum side of the membrane and can cause the GO membrane to swell and leak. Once the membrane is fully wetted, the selectivity of the membrane goes

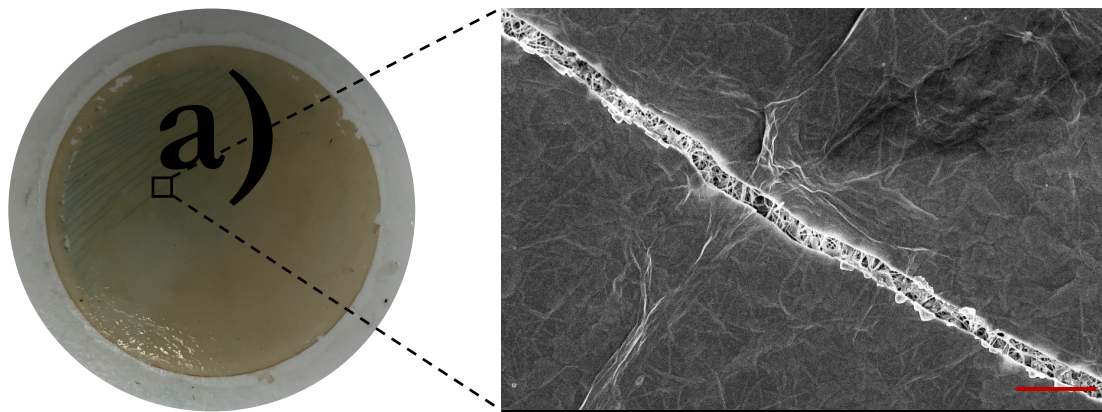


down and water and salt permeate through the membrane. This was observed in the acrylic cell as shown in **Figure 4.4d**, where the permeant side of the acrylic cell is completely covered in crystallized salt. The salt accumulates on the permeant side as the leaked water continues to evaporate due to vacuum. The inset on **Figure 4.4d** shows the crystallized salt on the permeant side after the setup was taken apart.

Concentration polarization (CP) refers to the gradient of concentration from the bulk feed solution to the membrane feed surface, which usually occurs gradually as the concentration of the non-permeating component increases at the surface [22]. Since the feed flow rate is not high in PV, CP is not an issue, unless the membrane is too selective. The way to resolve CP is to introduce some convection near the membrane surface in order to reduce the boundary layer [14], [22]. In PV, temperature polarization is more heard of, due to the evaporation of water molecules near the membrane surface, which as mentioned before, requires energy. The heat of vaporization is provided

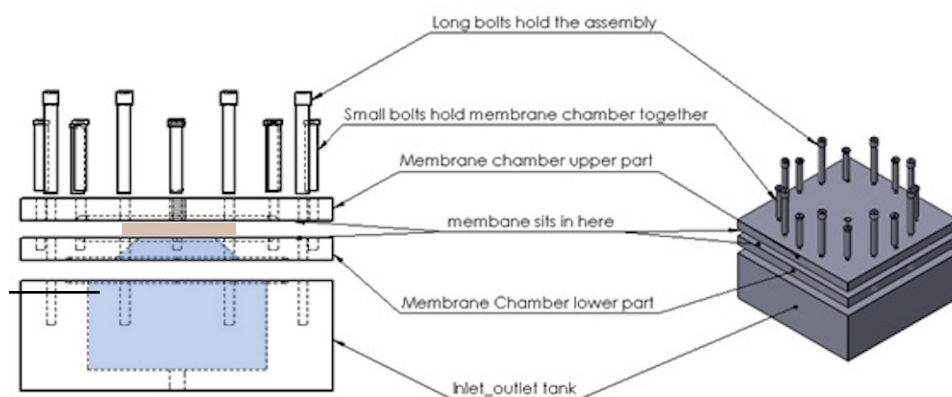
by the feed, which reduces the temperature at the membrane surface, affecting the driving force and thus the flux. Considerations must be given to these aspects of PV in order to maintain performance of the membranes.

We added trace amounts of methylene blue to our saltwater feed to look at the flow dynamics. With the addition of methylene blue, we observed that there were surface defects on the vacuum filtered



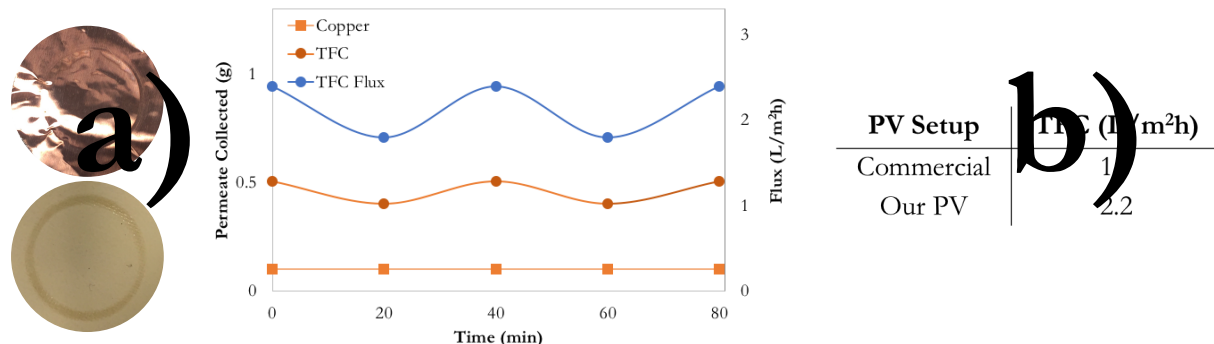
membranes as shown in **Figure 4.5**, which would definitely cause a leakage. This helped us to improve our vacuum filtration process, in addition to optimizing the design of our flow dynamics.

The clear acrylic cell helped us to understand our PV membrane better, however, we were not able to test our membranes at higher temperatures (e.g., near 100 °C required for some application such as



filtration steam reformed process water). Therefore, we upgraded to stainless steel for the second iteration of the membrane module. As depicted in **Figure 4.6**, the module has three pieces; the first one is the feed reservoir, the second one designed with a cone to focus the flow on the membrane, and the final piece is the vacuum outlet. The membrane is sandwiched between the second and third piece, with a mesh support. The stainless-steel cell has a very similar layout as the acrylic, thus similar flow dynamics. We also installed a thermocouple in the first piece to measure the temperature inside the module at all times during the run.

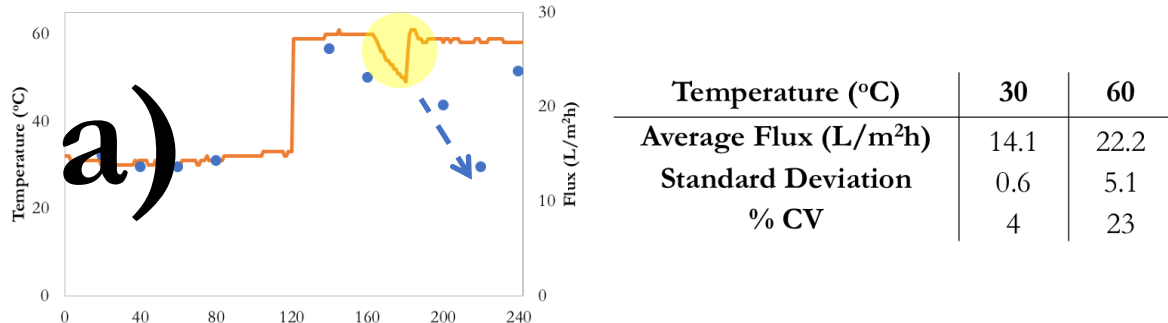
We ran two tests to validate our stainless-steel setup, the data for which is shown in **Figure 4.7**. First, we ran the PV module at 30 °C with a copper foil in place of the membrane. The purpose of this test was to quantify amount of water collected due to tubing leaks. Based on this experiment, we observed that we collected about 0.1 g of water every 20 minutes. This is a systematic error in our flux measurements, which we corrected for in our flux values. We also ran another validation test with a TFC commercial membrane at 30 °C to compare the performance of our PV setup with a commercial one through our collaborators in Professor Xianshe Feng's lab. Based on the results, we observed a deviation of 14%, between our two labs PV cells, which is acceptable, considering the variability in balance readings and other setup differences.



After validating our PV, we tested the setup with our membranes to optimize other aspects of the process. We were observing unstable flux at higher temperatures (i.e., 60 °C) in comparison to observations at 30 °C, as shown in **Figure 4.8**. We calculated the coefficient of variation (CV), which is expressed as a percentage and defined as the ratio of standard deviation to the average. It measures

the extent of variability in relation to the average. %CV in the flux reached ~25% at 60 °C while being around 5% at 30 °C. Since we could not see inside the stainless-steel cell, the addition of the thermocouple gave us more insight about the PV parameters and what is required to get steady and reliable flux readings.

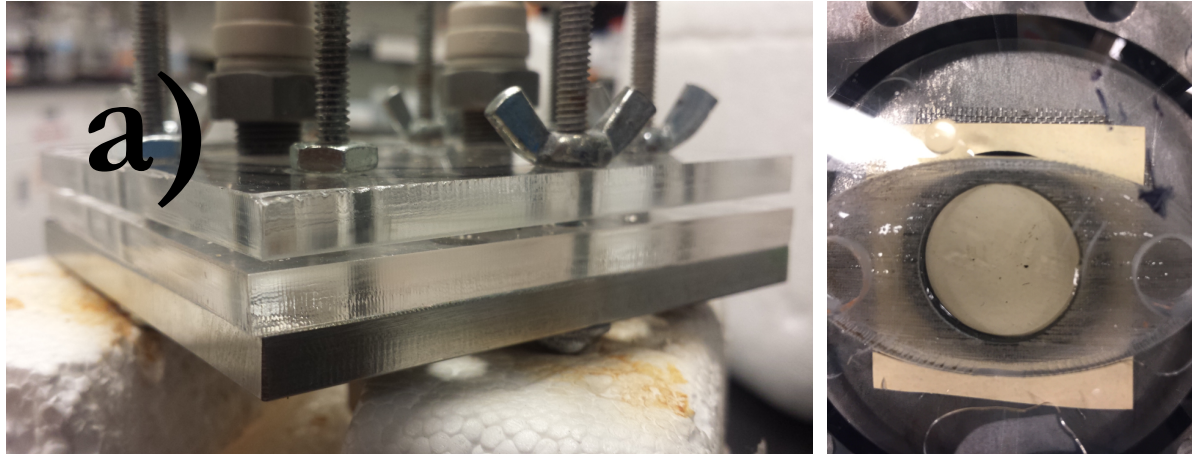
Based on the thermocouple outputs, we observed that at higher temperature, the unsteady flux was due to several reasons. First, at higher temperatures, the feed produces more air bubbles, which get circulated to the membrane surface by the peristaltic pump. This increases the instances of air bubbles on the membrane surface, thus hindering steady permeation. In addition to this, at higher temperatures, after an unwanted temperature drop as highlighted in **Figure 4.8a**, the time required to stabilize the membrane flux is longer compared to lower temperatures. After the temperature drop around 160 minutes, the temperature in the membrane module went back to 60 °C. However, the flux was not recovered until 240 minutes. This shows that the membrane requires a long time to stabilize, and we need to minimize such large temperature drops to ensure stable permeation.



As depicted in **Figure 4.9**, the difference between the first and second iteration of membrane modules were the flow dynamics. In the second iteration, the conic section and feed reservoir were thinner and larger compared to iteration 1. The thinner conic opening of stainless-steel cell is better optimized for cross-flow dynamics compared to the clear acrylic cell. However, we believe having a large reservoir



is not good for cross flow, because under low flow pressures, there is not enough convection to help with concentration polarization. Thus, for the third iteration of the membrane module, the cross-flow dynamics were improved by minimizing the cone and the reservoir volume, while increasing the distance between the feed inlet and outlet, as shown in **Figure 4.9c**.



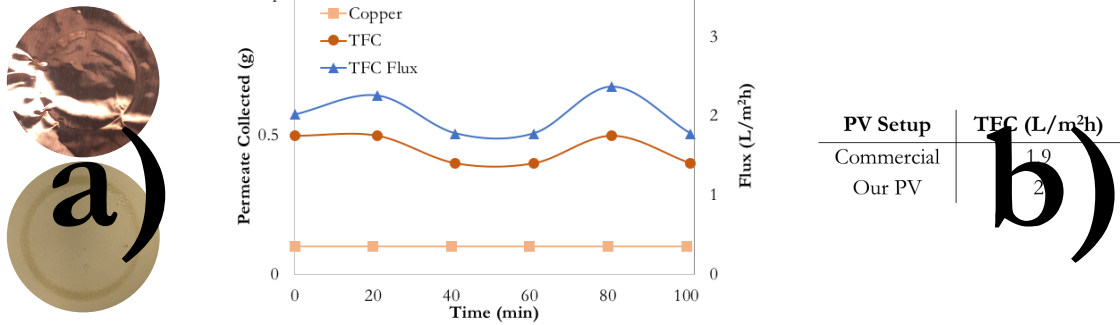
The final iteration of the membrane module consisted of a half stainless steel and half acrylic cell. We reused piece 3 of the stainless-steel module for the permeant side, as shown in **Figure 4.10**. For the feed side, we designed a new piece of acrylic with the new layout for an optimized flow dynamic as shown in **Figure 4.9c**.

We ran the same two validation tests as above, with the copper foil to check for leaks and TFC membrane for comparison of commercial and our PV modules. As shown in **Figure 4.11**, the deviation between the commercial PV and our module is 5%. With this iteration, we observe more convection in the feed flow, which is better for the membrane. However, because of the instability of acrylic at higher temperatures, we are not able to test this module at higher temperatures, thus, we suggest the best thing to do next is to design a similar flow dynamic with the stainless-steel cell.

1

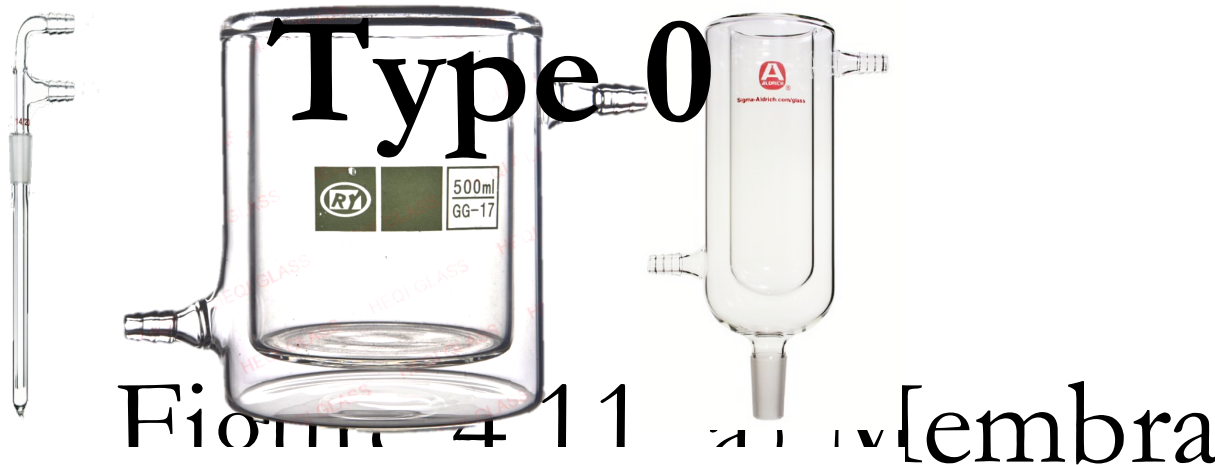
2

3



4.2.2 Permeate Collection Optimization

For lab-scale setups, permeate (i.e. water vapour) can be collected in the condenser via two common ways: using liquid nitrogen (-196 °C) or dry ice (-79 °C) with ethanol. In our setup, the condensers are swapped every 20 minutes for collecting the permeate. This means the liquid reservoir needs to be emptied and transferred. In this process, the loss of liquid nitrogen is much more than the dry ice since the dry ice is not as cold as the liquid nitrogen. The standard type of condensers for these lab-scale experiments are called cold fingers, which are usually immersed in liquid nitrogen and are very small in size, similar to type 0 in **Figure 4.12** [92]. We required condensers that had large reservoirs for dry ice and ethanol. These condensers, types 1 and 2 in **Figure 4.12**, are double walled with a large



amount with respect to membrane and c) tabulat

reservoir for dry ice and a large surface area [93], [94]. All these condensers have two connections, where one side is connected to the vacuum and the other side is connected to the membrane.

To figure out optimal sampling time and condenser capacities, we ran experiments with two condensers in series, one of type 1 and type 2. Condensers A and B were type 1, with different sizes, while condensers C and D were type 2, same size, as shown in **Figure 4.13**. We experimented with different sampling times, ranging from 5 minutes to 120 minutes, and we measured the amount of



overflow (in percentage) of the permeate that was observed in the second condenser in series as a function of first condenser surface area. Surface area of inner reservoirs of each condenser is tabulated below in

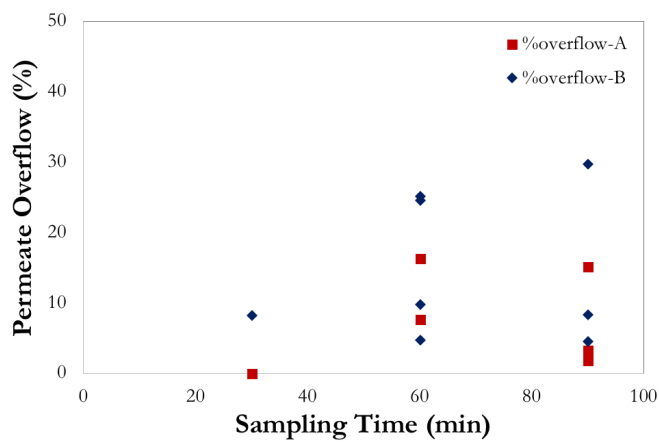
Table 4.1.

Table 4.1: Surface area of condensers in cm²

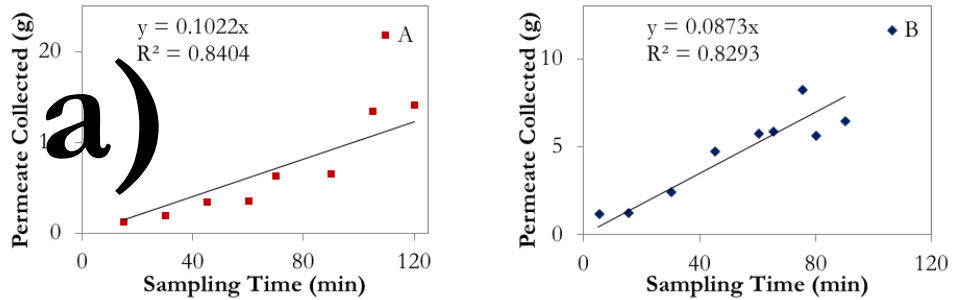
A	B	C	D
389	237	334	334

Figure 4.13: Condensers used where A and B w

We expected that at lower sampling times, the percent overflow of the permeate from condensers A and B into the condenser-in-series would be about the same, while at higher sampling times, the percent overflow from condenser B would be larger than condenser A. Based on **Figure 4.14**, we observed that at 30 minutes of sampling time, the percent overflow of condenser A is 0% and condenser B is about 8%. Following, at 60 minutes and 90 minutes of sampling, the percent overflow of condenser A remains below 16%, while for condenser B, it is about 30%. Based on these results, we concluded that the surface area of condenser A is sufficient to ensure that at a sampling time of 30 minutes or less, there will be no significant loss of permeate. Following these findings, we experimented with 15 and 20 minutes of sampling times, which were both acceptable.



In addition to the percent overflow, we also measured capacity of condensers A and B as a function of sampling times. The capacity is the amount of collected permeate as a function of the surface area available for condensation, which is simply based on the dimensions of the condenser. We expect that the condenser with larger surface area will have a higher capacity. At every sampling time, we averaged the amount of permeate collected and plotted that average with respect to sampling time, as shown in **Figure 4.15**. Based on these results, we are able to see that at any sampling time, the average permeate amount collected is larger in condenser A compared to condenser B. This shows that a higher surface area is required for a higher capacity.



In addition to the sampling time and condenser capacity, an important aspect of permeate collection is a steady vacuum level. The membrane is very sensitive to pressure changes, i.e., if there is an abrupt pressure change when switching condensers, it can cause capillary condensation in the porous membrane support. Once this capillary condensation is initiated, the permeate will continue condensing in the pores until it swells the membrane and causes a leakage. For this reason, we inserted a valve, for a smooth transition when switching between condensers.

In addition to the condenser, the vacuum level is extremely important to ensure high collection efficiency. The vacuum level defines the driving force (i.e. the chemical potential) across the membrane, which affects the transmembrane flux. To maximize this flux, we require an almost-perfect vacuum level, which is 760 mmHg relative to atmospheric pressure (0 mmHg). With our vacuum pump, we achieve a 758.2 mmHg (or 1800 mTorr). With the house vacuum line, we can achieve around 600 mmHg, which has a large impact on the flux. We can use the flux equations for solution-diffusion model as well as pore-flow model to predict the effect of the vacuum. First, looking at the solution-diffusion model, the flux with respect to the vacuum pressure is expressed in Eq. 8, which simplifies to:

$$J_i = \frac{P_i}{l} \left(C_{if} - \frac{p_{ip}}{\gamma_{if} p_i^{sat}} \right) \quad \text{Eq. 14}$$

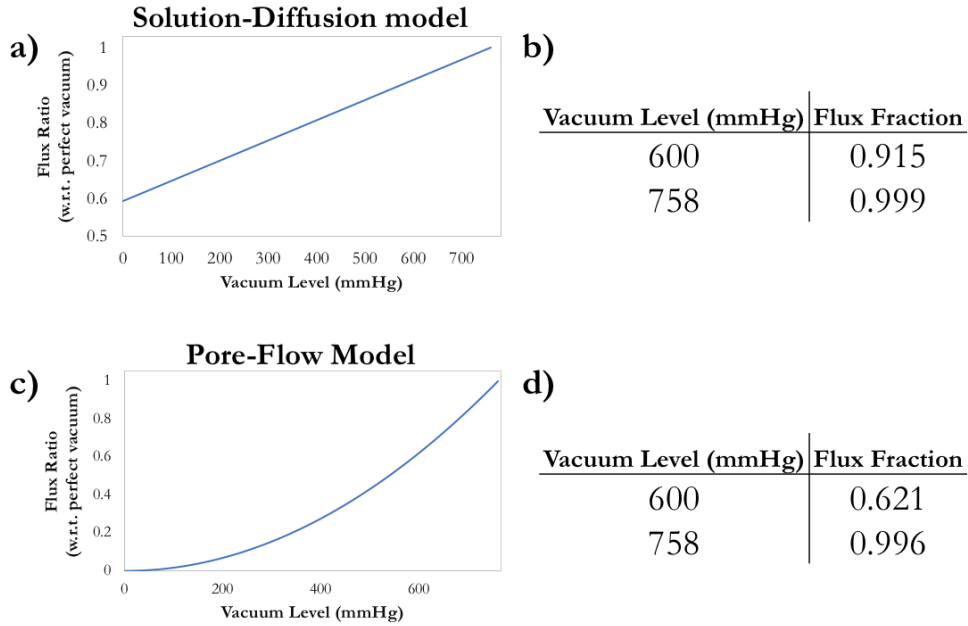
where the variables are the same as before. The pressure on the permeate side (p_{ip}) is dictated by the vacuum level. Since we do not know the permeability coefficient of our membrane, we can understand the effect of the vacuum level by looking at the flux ratio with respect to perfect vacuum. In the simplified case, we can assume that the activity coefficient (γ_{if}) of feed is 1. Based on this simplification, we observe the following relationship between flux and vacuum level, as shown in **Figure 4.16a**. To compare the difference between the vacuum levels, at 600 mmHg, we are

theoretically only collecting 91% of the permeate, while at 758 mmHg, we are collecting almost 100%, as calculated in **Figure 4.16b**. This makes a big difference, especially at higher fluxes.

Second, the permeation flux of the vapor phase in the pore-flow model is expressed by the second term in Eq. 4, which is as follows:

$$Q_{vapor} = \frac{B_i}{yb} (P_{i,*}^2 - P_{i,2}^2) \quad \text{Eq. 15}$$

where the variables are the same as defined before. The pressure on the permeate side ($P_{i,2}$) is dictated by the vacuum level. Similar to the solution-diffusion case, we simply look at the ratio of the flux with respect to perfect vacuum. Based on the above equation, we observe the parabolic nature of the pore-flow model dependency, as shown in **Figure 4.16c**. Our results show that at 600 mmHg, we are theoretically only collecting 62% of the permeate, while at 758 mmHg, we are collecting almost 100%,



as calculated in **Figure 4.16d**. With the pore-flow model, the vacuum level makes a bigger difference. Therefore, we must ensure that the vacuum level is always maintained by sealing the entire PV module properly.

4.2.3 Peripheral Components Optimization

The membrane module and condenser design are extremely important in optimizing the overall pervaporation setup, but they are not the only components. Other important components that required optimization were: the peristaltic pump, vacuum level, and the overall seal.

The peristaltic pump used for the continuous flow of the feed to the membrane was purchased from Fisher Scientific [95]. The two most important aspects of the peristaltic pump for our application was flow speed and compatibility with high temperatures. We observed that at lower speeds, the temperature of the feed was much lower in the membrane module than in the flask. For example, if the feed temperature in the flask was at 35 °C, the feed in the membrane module was only 25 °C. This was due to the heat loss to the environment and tubing. However, this problem was mitigated when faster speeds were used to run the peristaltic pump. In most of the experiments, the peristaltic pump was run at its maximum speed of 85 mL/min. The other factor was compatibility with higher temperatures. This pump has polypropylene fittings and silicone tubing, which can handle temperatures of up to 130 °C and 260 °C, respectively.

4.3 Graphene Oxide Membranes

Vacuum-filtered graphene oxide membranes have been used in RO settings, but it has been widely accepted that these membranes are not stable in the water system without some cross-linking. When the GO membrane was immersed in water in its native state, the membrane very easily disintegrated in water in 30 minutes, as shown in **Figure 4.17a**.



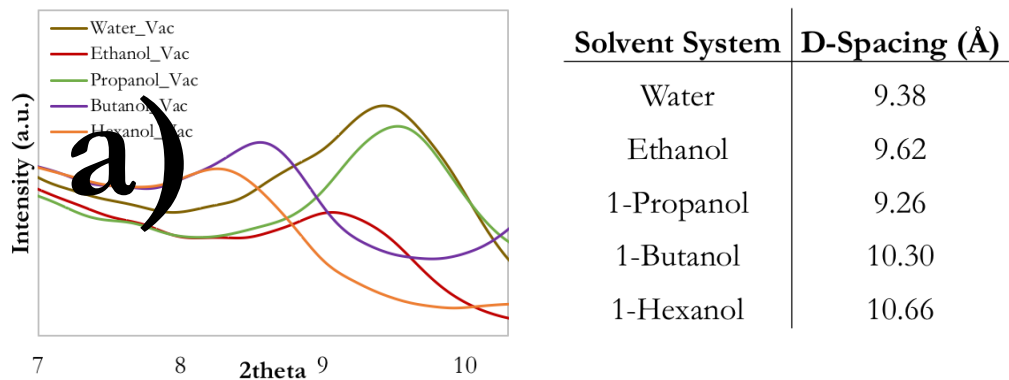
Since in PV, the membrane is not completely immersed in the water system, GO could possibly survive without cross-linking, however, we observed in our experiments that the membrane was not stable for PV in its native state, even at thickness of 8 μm . Based on other works with GO in PV systems, the membrane thicknesses that are required for achieving a reasonable flux are in the range of a few hundred nanometers. Therefore, we looked into cross-linking GO membranes for increased stability at all thickness, especially when the thickness is reduced to a few hundred nanometers. There are various methods of cross-linking that people have looked into. The recent publication by Yeh *et al.* simplified the process [96]. A simple way to cross-link GO is with divalent and trivalent cations, such as Zn^{2+} and Al^{3+} . In our experiments, we tested out Zn^{2+} based on the procedure that was followed in the paper. We prepared a stock of 0.1 M ZnCl_2 at pH 5 and immersed our vacuum-filtered GO membranes in for 24 hours. Consequently, the Zn^{2+} enhanced membranes were dried in the vacuum oven before use. We observed a drastic change in the stability of the membrane. As shown in **Figure 4.17b-c**, at high speeds of mechanical stirring, GO membrane without cross-linking started to flake off, while the Zn^{2+} enhanced GO membrane stayed intact.

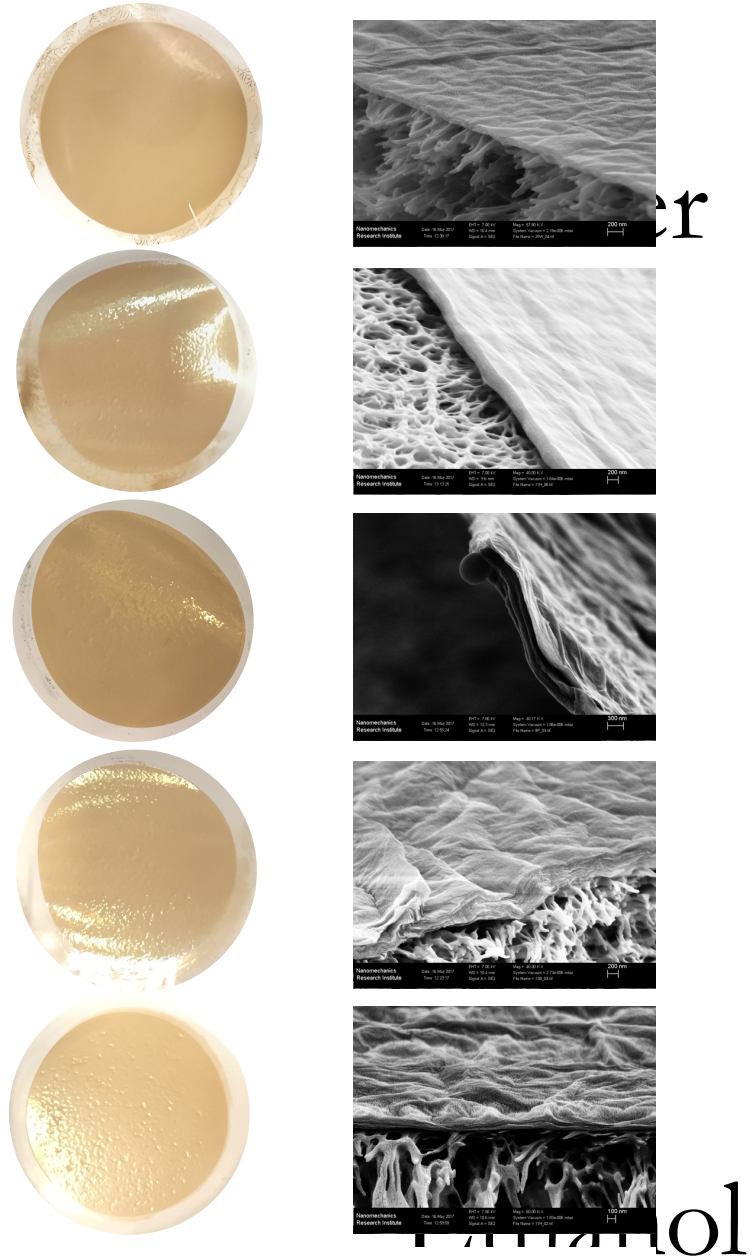
A way to optimize the flux and rejection of the GO membrane is to adjust the interlayer spacing of the GO membrane. Here, we looked at creating vacuum-filtered films from our various 1-alcohol dispersions based on the expectation that the difference in the 1-alcohols length would change the d-spacing between the GO flakes, similar to XRD data presented in **3.3.3.3** with dried GO slurries. As shown below in **Figure 4.18**, we observed a similar trend in the interlayer spacing of the GO vacuum-filtered membranes where the interlayer depended on the length of the solvent molecule. The 1-propanol seemed to be off the trend for some reason, but the others followed the trend. We observed

Figure 4.17: a) Vacuum-filtered GO membrane.

a slightly curved baseline with the vacuum-filtered GO membranes, which was due to thickness of the membrane. These vacuum-filtered films were only 500 nm thick, therefore, some signal from the polymer support was also collected.

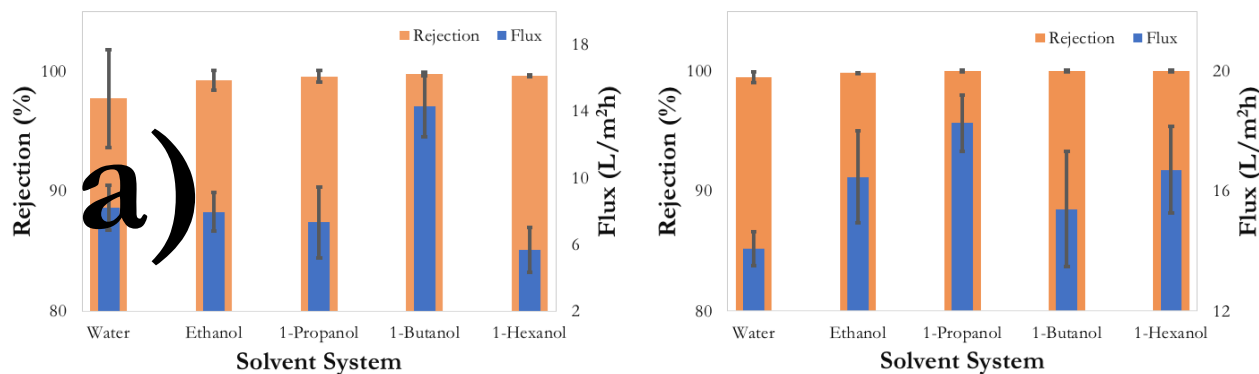
After preparing these membranes and enhancing them with ZnCl₂, we characterized them using our PV module. The vacuum-filtered membranes from each of the dispersions on a commercial polyethersulfone (PES) membrane are depicted in **Figure 4.19**. The vacuum-filtered membrane surfaces from the water stock turn out much smoother than the 1-alcohols. This is also observed under the SEM, where the surface of water and ethanol membranes seem smoother compared to the other 1-alcohol membranes.



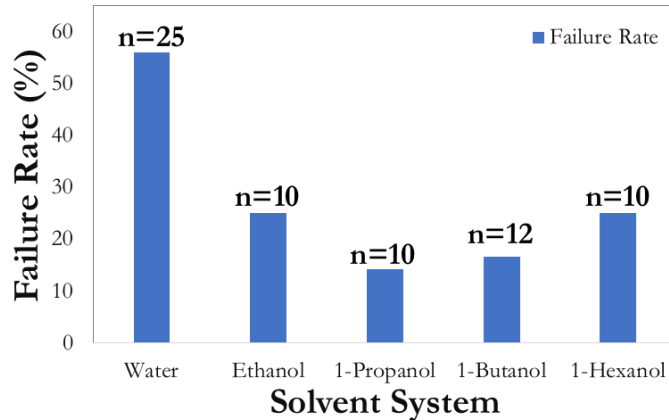


With our solvent systems, the d-spacing of our membranes range from 9 to 11 Å. Using these membranes in our PV system will give us a better understanding of the relationship between flux and rejection relative to GO d-spacing. We expect that the membranes with a larger d-spacing would have a higher flux and lower rejection, because intuitively, a larger d-spacing means a higher permeation of

water as well as salt. With our tests, we can see if there is an optimal d-spacing that increases the flux and simultaneously maintains the rejection at approximately 100%. We compare the flux and rejection of these membranes at two loadings; $160 \mu\text{g}/\text{cm}^2$ (**Figure 4.20a**) and $40 \mu\text{g}/\text{cm}^2$ (**Figure 4.20b**) at 30°C . At $160 \mu\text{g}/\text{cm}^2$, the rejection of the water membrane is the lowest at 97%, while the others are all above 99.5%. The flux, however, is approximately the same for all membranes, except 1-butanol, which has a significantly higher flux. At $40 \mu\text{g}/\text{cm}^2$, we observe that the rejection of all the membranes was maintained at above 99.5%, and the flux had increased for all membranes compared to from the $160 \mu\text{g}/\text{cm}^2$ loading. The highest flux was achieved in the 1-propanol membrane. We observe an improved flux when considering the average flux values, however, when considering the variability in the flux, there may not be a significant difference between the 1-alcohols systems.



The first set of data in **Figure 4.20** was measured in the acrylic PV module while the second set of data was measured in the stainless steel. Looking more closely at the first data set, %CV of the water membrane rejection is much larger than the others, suggesting that there was an issue of either condensation or a leak. This is definitely possible because the GO membranes from the water system seem to perform poorly compared to the 1-alcohol systems. We looked at the failure rate of the membranes with respect to the solvent systems. The failure rate was calculated based on the frequency of membranes observed to leak at the start of the run; this rate does not consider membranes with condensation issues during the run, like the $160 \mu\text{g}/\text{cm}^2$ water membrane from **Figure 4.20a**. As shown in **Figure 4.21**, more than 50% of the water membranes leaked at the start of the PV run, while the failure rate for the 1-alcohols systems is below 25%.



Despite having the smallest d-spacing, the membranes from the water system are more prone to failing. Based on the considerable difference in the membrane performances and failure rates, we believe that there are more differences between the 1-alcohols systems and water than just the d-spacing. From the failure rates, we conclude that the water membranes are either more prone to swelling or are less strong mechanically. The mechanical strength of the membrane dictates how well the stress of the O-rings is distributed throughout the membrane, and the swelling would be a factor of the water intake. It is likely that the solvents not only play a part in changing the d-spacing of the membrane, but also affect the interlayer GO chemistry, which results in the varied performances. We looked at the flux as a function of temperature to characterize the temperature dependence of the membranes, and to quantify the activation energy of each membrane, based on the Arrhenius equation, shown below:

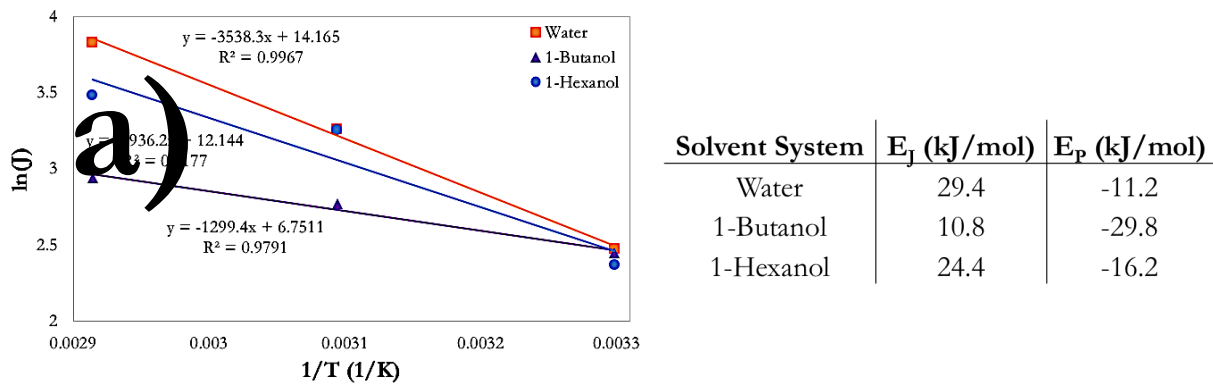
$$J = J_0 \exp(-E_J/RT) \quad \text{Eq. 16}$$

where J is the flux as defined before, E_J [J/mol] is the activation energy of permeation flux, R [J/mol.K] is gas constant and T [K] is temperature. E_J can be evaluated by plotting $\ln J$ vs. $1/T$ and extracting the slope of the line. The Arrhenius equation above is a simplified version of Eq. 12 to use flux instead of permeability coefficient, as it is more easily attainable. The activation energy of permeation, E_P , can be easily calculated by this relationship:

$$E_P = E_J - \Delta H_v \quad \text{Eq. 17}$$

where ΔH_v is the enthalpy of vaporization of water. Measuring E_P directly from Eq. 12 is more complicated, thus finding E_J and then subtracting ΔH_v is used [97]. The Arrhenius plots of water, 1-butanol, and 1-hexanol membranes at a loading of $80 \mu\text{g}/\text{cm}^2$ is shown in **Figure 4.22a**. We observe

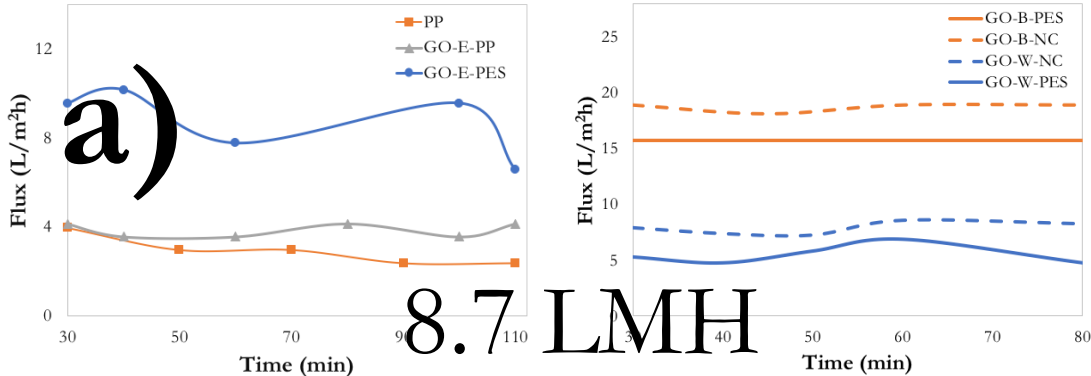
straight lines for each membrane with a different slope, where the slope is E_J . To find E_P , we simply subtract the enthalpy of vaporization of water, which was taken to be 40.65 kJ/mol. The values of each activation energies are provided in **Figure 4.22b**. The negative values of E_P suggest that permeability coefficient of the membrane decreases as the temperature increases, which would imply overall permeation decreases as temperature increases. However, we still observe an increased permeation flux as temperature increases because the effect of the temperature on the saturated vapor pressure is more significant than the temperature effect on the activation energy. The more negative E_P in the case of the 1-butanol suggests that there is a larger energy barrier for the water to overcome in the 1-butanol membrane, which is why we do not observe as much of a flux increase with temperature compared to water and 1-hexanol.



Another interesting observation from **Figure 4.22a** is that at lower temperatures, the flux of all three systems are approximately the same. It is at higher temperatures that the 1-alcohols systems fall behind compared to water. However, at lower loadings such as 40 $\mu\text{g}/\text{cm}^2$, as shown in **Figure 4.20b** in the flux data, the 1-alcohols perform better than the water membrane. Thus, thinner membranes from 1-alcohols systems are more efficient than the water membranes at lower temperatures. The hinderance of permeation at higher temperatures in the 1-alcohols membranes might be due to the negative thermal expansion effect that has been observed in Hummer's GO [98]. You *et al.* observed that with increasing temperature, the interlayer spacing of GO in methanol and ethanol decreases [98], which may explain the bigger activation energies in the cases of 1-alcohols at higher temperatures.

In addition to the active layer (i.e. GO layer), we also observed a flux dependence on the membrane support. Based on the principle of PV, usually the active layer is the only part of the membrane

responsible for the selectivity. However, PV desalination has never been studied in this much detail to understand the differences between the transport mechanism between the polymeric membranes and GO. **Figure 4.23a** shows the effect of the polymer support on the flux, where we compare PV flux of a bare polypropylene (PP) membrane, and GO from ethanol dispersion on PP and PES at a

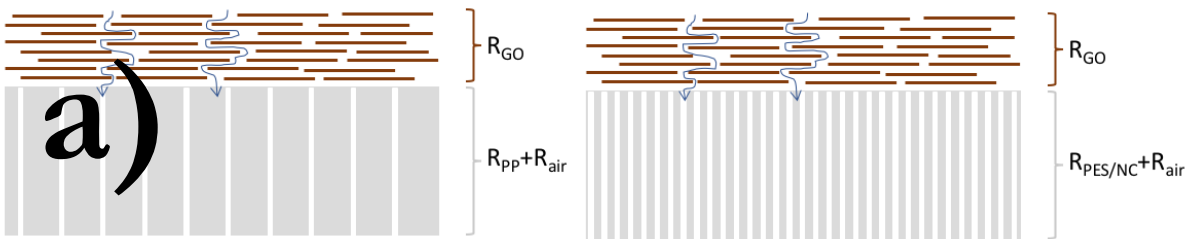


loading of $160 \mu\text{g}/\text{cm}^2$ at 30°C . We observe that bare PP and GO on PP have approximately the same flux, while GO on PES has a much higher flux, similar to performance achieved with membranes in **Figure 4.20a**. PP and PES both have similar hydrophobicity, as depicted by their contact angles of 102° and 100.6° , respectively [99]. The other difference between the two polymer supports are the pore sizes and porosity. PP has asymmetric pores ranging from 50 nm by 10 nm to 200 nm by 50 nm , while PES has more symmetric pores larger than 200 nm . PP has 39% porosity while PES has 75% . Due to the lower porosity and relatively smaller pores, PP does not allow liquid water through the membrane as fast as PES, therefore, the flux across the GO-PP is limited by PP. However, the flux may be completely different in the case of PES with larger pores and higher porosity, we observe a higher flux. In both cases, we still observe an almost perfect salt rejection (i.e. 99.9%). Similar results were achieved with the GO membranes from 1-butanol and water dispersions at 30°C on PES and nitrocellulose (NC) at a loading of $80 \mu\text{g}/\text{cm}^2$ and $160 \mu\text{g}/\text{cm}^2$, respectively [100]. NC is much more hydrophilic compared to PES, with a contact angle of 51° . However, in this case, both the polymer supports have similar pore sizes and porosity. In both cases of GO-butanol and GO-water, as shown in **Figure 4.23b**, we observed a higher flux with the more hydrophilic support, suggesting a difference in transport mechanisms. **Table 4.2** summarizes all the important features of the membranes, which include the material, pore symmetry, pore sizes, porosity and contact angle.

Table 4.2: Summary of properties of support membrane material

Material	Pore Symmetry	Pore Sizes (nm)	Porosity (%)	Contact Angle (°)
PP	Asymmetric	200 nm by 50 nm	39	102
PES	Symmetric	200 nm	75	100.6
NC	Symmetric	220 nm	75	51

Based on our calculations, a larger % difference in flux is observed in the system comparing PP and PES, where the difference in contact angle is minimal, but the difference in porosity is large. As shown in **Figure 4.24**, there are three types of media the water has to permeate through, all of which provide some resistance against the permeation. Presumably, the resistance from the GO layer is dependent on the interlayer distance, the chemistry of the nanochannels, thickness and the tortuosity of the membrane. These factors should be the same in all vacuum-filtered films produced from any solvent. Therefore, the variations in the permeation is due to the support. The porous support membrane has two separate resistance values, one from the dense polymer and one from the pores. Usually diffusion coefficients through the dense polymeric part is extremely slow, therefore the flux changes that we



observe in the membrane may be due to the fraction of the pores available. Therefore, we believe that unlike in the solution-diffusion model, the vapour desorption step also limits flux. The water permeation through the GO layer is fast. However, once the water molecules reach the support membrane, the permeation is limited by the porosity of the membrane. We observe that with high porosity of 75%, the permeation through PES is 230% higher than through PP. However, we observe a lower increase in the case of PES and NC, where the permeation is 120-140% through NC.

Based on these results, we deduce that GO acts as a molecular sieve, where it separates water molecules from hydrated salt ions. Depending on the optimal interlayer spacing, GO allows water molecules through and blocks hydrated ions, but water molecules do not evaporate inside the GO active layer. The water molecules travel across GO as liquid, which then evaporates somewhere in the support

membrane. It is difficult to figure out the exact transport mechanism, but with performing tests with a variety of support membranes, we have gained more insight on the mechanism of transport through GO, which seems to be very different from dense polymeric membranes, at least in the solvents that we tested.

4.4 Conclusions

In this chapter, we have successfully validated and optimized a custom-built PV module. With our experiments, we have learned the effects of feed flow dynamics on the permeation dynamics and concentration polarization effects, as well as the effect of maintaining a steady vacuum pressure on the permeate side. We were able to successfully minimize condensation and leakage issues with proper handling of the vacuum valve and gauge. We also optimized the size of condensers required for complete permeation collection.

In terms of the GO membrane, we successfully showed that with the different solvent systems, we are able to achieve vacuum-filtered membranes with a variable interlayer spacing, which plays a part in the membrane's performance in PV. We observed that the membrane with optimal performance was 1-propanol with the highest flux at 18.6 L/m²h and rejection of >99.8% at 3.5 wt% of NaCl salt solution at 30 °C.

We also showed that the vacuum-filtered GO membranes from the water dispersion have greater than 50% failure rate, either due to a mechanical issue or swelling. The 1-alcohol membranes have a failure rate of less than 25%, despite all the same process, including Zn²⁺ enhancement to improve stability in water. We calculated the activation barrier for permeation for water, 1-butanol and 1-hexanol membranes using the Arrhenius equation, which suggested that water has the lowest activation barrier for permeation compared to the 1-alcohols systems. We concluded based on our analysis that 1-alcohol membranes perform better at lower temperatures and lower thickness, compared to the GO-water system.

In addition to the effects of the GO layer, we also observed a flux dependence due to the membrane support. Based on this data, we hypothesize that the porosity of the membrane has a major effect on the flux. PES with 75% porosity was observed to have a flux 230% compared to PP with a 39%

porosity, with the same thickness GO layer. This gives us more insight into the transport of water across the GO membrane as well as the polymer support membrane, which has not been studied in detail prior to this.

5 Expanding on Graphene Oxide Membrane Preparation

The main technique used currently to prepare graphene oxide membranes for PV are vacuum filtration. This technique suffers from many problems, such as slow throughput, batch to batch variability, inability to make thinner membranes. Expanding on preparation methods that are higher-throughput, more efficient, reliable, and easily scalable are extremely valuable with moving graphene oxide technology forward, not only for PV, but for all applications. Here, we look at two techniques to replace vacuum filtration:

- Casting membranes with the doctor blade, which is easily scalable, reproducible, and high performance
- LB technique to get ultrathin (monolayer) graphene oxide films, with potential for roll-to-roll deposition

5.1 Solution Casting

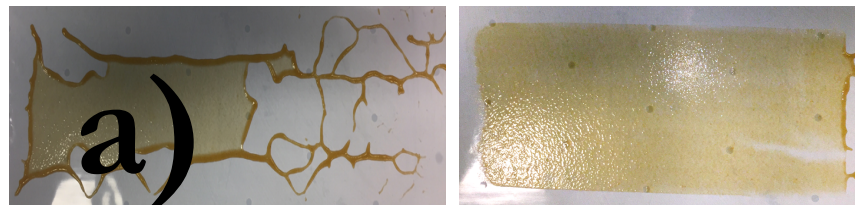
Solution casting has been commonly used in polymer membrane preparation, where an even film of a polymer solution is spread across a flat plate with a casting knife. The casting knife consists of steel blade with two runners, arranged to form a precise gap between the blade and the plate. The extension of this technology from polymers to GO dispersions has been realized by Akbari *et al.*, where they were also able to automate the casting process using a gravure printing machine [101]. With this technology, they were able to achieve highly crystalline membranes for RO purposes.

The technology is capable of forming these cast films, however, the GO dispersions were not optimized. In order to get a good membrane thickness and uniformity, the concentration of the GO ink is extremely crucial. Akbari *et al.* used superabsorbent polymer hydrogel beads to absorb water from aqueous GO dispersions to achieve their desired concentrations. Here, we show that we are able to achieve GO casting solutions that are of the right consistency and concentration for casting GO membranes.

5.2 GO Cast Membranes

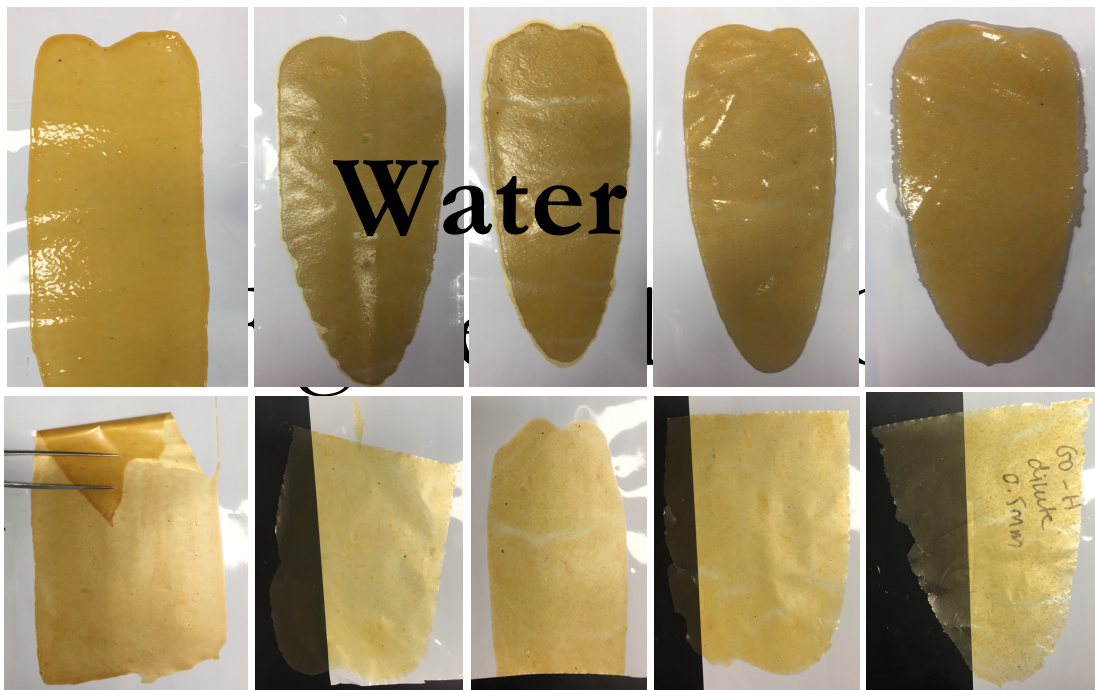
As presented in **Table 3.1** in **3.3.1**, we are able to achieve more than 2 wt% of GO in water and higher than 8 wt% of GO in 1-alcohols simply by centrifugation. The casting substrate is very important to

ensure wettability of GO dispersions. We used PP to cast our membranes. Even though PP is extremely hydrophobic, the 1-alcohols wet the membrane, which allowed GO to form a nice film. However, in the case of aqueous GO, we had to treat the surface with a plasma cleaner to ensure wettability. **Figure 5.1** shows casting of aqueous GO dispersion on non-treated and treated PP surface. Without treating the PP surface, the GO dispersion does not wet the membrane. But with



the surface treatment, we achieved very uniform films with the aqueous dispersion.

As shown in **Figure 5.2** first row, we were able to achieve uniformly cast membranes from all solvent dispersions. With the use of PP, as shown in **Figure 5.2** bottom row, an additional benefit was that after the GO films had dried, they were easily peeled off the PP surface to form a freestanding GO film. As depicted, the dried membranes are freestanding, flexible (as demonstrated by water



membrane), and transparent (as demonstrated by 1-hexanol membrane). We characterized these cast membranes with Raman, XRD, and EDS, which all had similar properties as discussed earlier.

In an attempt to use these cast-GO films and improve PV flux with partial reduction, as suggested by MD simulation results, we performed a simple study to look at the properties of the cast membranes during thermal reduction, at low and high temperatures. We tried a low-temperature reduction process, where the films were placed in the vacuum oven for 16 hours at 75 °C, and a high-temperature reduction process, where a tube furnace was used at 200 °C and 250 °C for 1 hour.

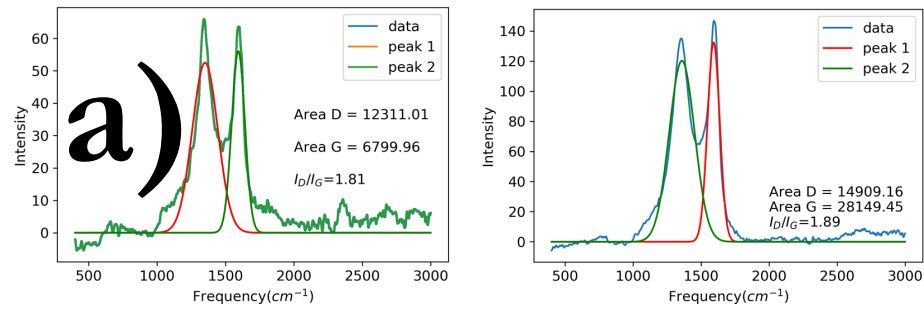
5.2.1 Low-Temperature Reduction

The low-temperature reduction process is not capable of removing all oxygen functionalities, as shown by our thermal stability analysis in **Figure 3.20**, where we observed the loss of labile oxygen functionalities around 180-200 °C. The low-temperature reduction process caused a physical change in the membranes, where the membrane color and flexibility were affected. As shown in **Figure 5.3**, the GO membranes went from light brown to black, which indicates reduction. The flexibility of the membranes was slightly affected but the membranes were still bendable.



The low-temperature reduction of GO membranes were studied with Raman, XRD, and EDS. In the case of GO-ethanol, as shown in Raman spectra in **Figure 5.4**, we used the peak integral method to calculate the I_D/I_G ratios and compare the membranes before and after reduction. We observed that I_D/I_G ratios had slightly increased after reduction. At this temperature, there is minimal reduction, therefore, as shown in **Figure 3.4**, these partially reduced GO films have low L_a values. Therefore,

an increase in the I_D/I_G ratios suggest that there are less structural defects after the 16-hour reduction at 75 °C.



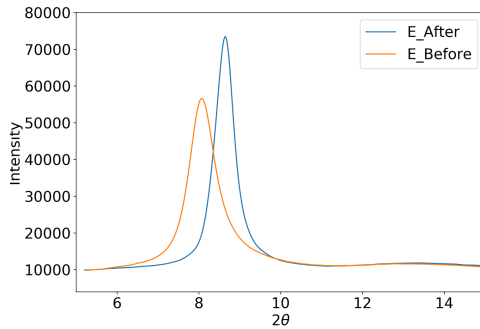
Error! Not a valid bookmark self-reference. presents the I_D/I_G ratios of all GO membranes before and after reduction, with the peak integral method. Based on this, we observed that the I_D/I_G ratios either increased.

Table 5.1: I_D/I_G ratios of GO cast membranes before and after reduction

Solvent	I_D/I_G Ratios (Area Ratio)	
	Before	After
Water	1.63	1.75
Ethanol	1.81	1.89
1-Propanol	1.57	1.74
1-Butanol	1.90	1.91
1-Hexanol	1.60	1.91

XRD results were also in agreement with the Raman findings. As shown in **Figure 5.5**, we observed a more crystalline peak after the reduction, where the GO peak became narrower after reduction. The increase in the I_D/I_G ratio is indicative of a more crystalline nature. There is a shift based on the XRD diffractogram shown, but there are no major signs of reduction.

Figure 5.4: GO-etha



Based on the analysis of our XRD data summarized in **Table 5.2.**, there is a small change observed in the d-spacing as well as the crystallite size of GO cast membranes before and after reduction. In all cases, the d-spacing of the membrane reduced while the crystallite size increases. The increase in the crystallite size suggests that the sp^2 hybridized graphene domains are growing, which suggests that graphitic lattice sizes (L_a) are increasing.

Table 5.2: Summary of XRD data of GO cast membranes before and after reduction at 75 °C

Solvent	Reduction					
	Before			After		
	2θ (°)	D-Spacing (Å)	Crystallite Size (nm)	2θ (°)	D-Spacing (Å)	Crystallite Size (nm)
Water	8.45	10.45	10.06	8.65	10.21	15.75
Ethanol	8.09	10.92	10.53	8.63	10.24	14.67
1-Propanol	7.68	11.50	7.24	8.76	10.09	13.26
1-Butanol	7.57	11.66	8.14	8.86	9.97	14.45
1-Hexanol	7.39	11.96	7.76	8.56	10.32	12.83

Based on EDS data presented in **Table 5.3**, we also observed an increase of C/O ratio on average, however, the increase is not too significant, which is acceptable for a low-temperature reduction.

Table 5.3: C/O ratios of GO cast membranes before and after reduction at 75 °C

Reduction	C/O Ratio				
	Water	Ethanol	1-Propanol	1-Butanol	1-Hexanol
Before	2.03	2.21	2.04	2.03	2.01
After	2.18	2.13	2.23	2.32	2.18

Figure 5.5: XRD di
ethanol cast membran
temperatur

The overall conclusion based on the low-temperature reduction at 75 °C is that this reduction process is sufficient to remove some adsorbed solvent molecules but not for making a completely reduced GO membrane. This may be a good procedure for getting partially reduced GO films that still have a large d-spacing to allow fast water transport for PV.

5.2.2 High-Temperature Reduction

Higher temperature reduction procedures were carried out in a tube furnace in an argon environment using a one-side-open ceramic tube at around 200-250 °C for 1 hour. **Figure 5.6a** shows the result of the reduction at 200 °C for an hour of GO-water membrane and **Figure 5.6b** shows the GO-ethanol membrane before and after reduction at 250 °C for an hour. These films looked almost silver after the high-temperature reduction indicating a more graphitic nature, and they were also brittle. We characterized the GO membranes using FTIR, XRD, and Raman, as shown below. **Figure 5.6c,e,g** pertain to GO-water membrane in **Figure 5.6a** and **Figure 5.6d,f,h** pertain to GO-ethanol membrane in **Figure 5.6b**.

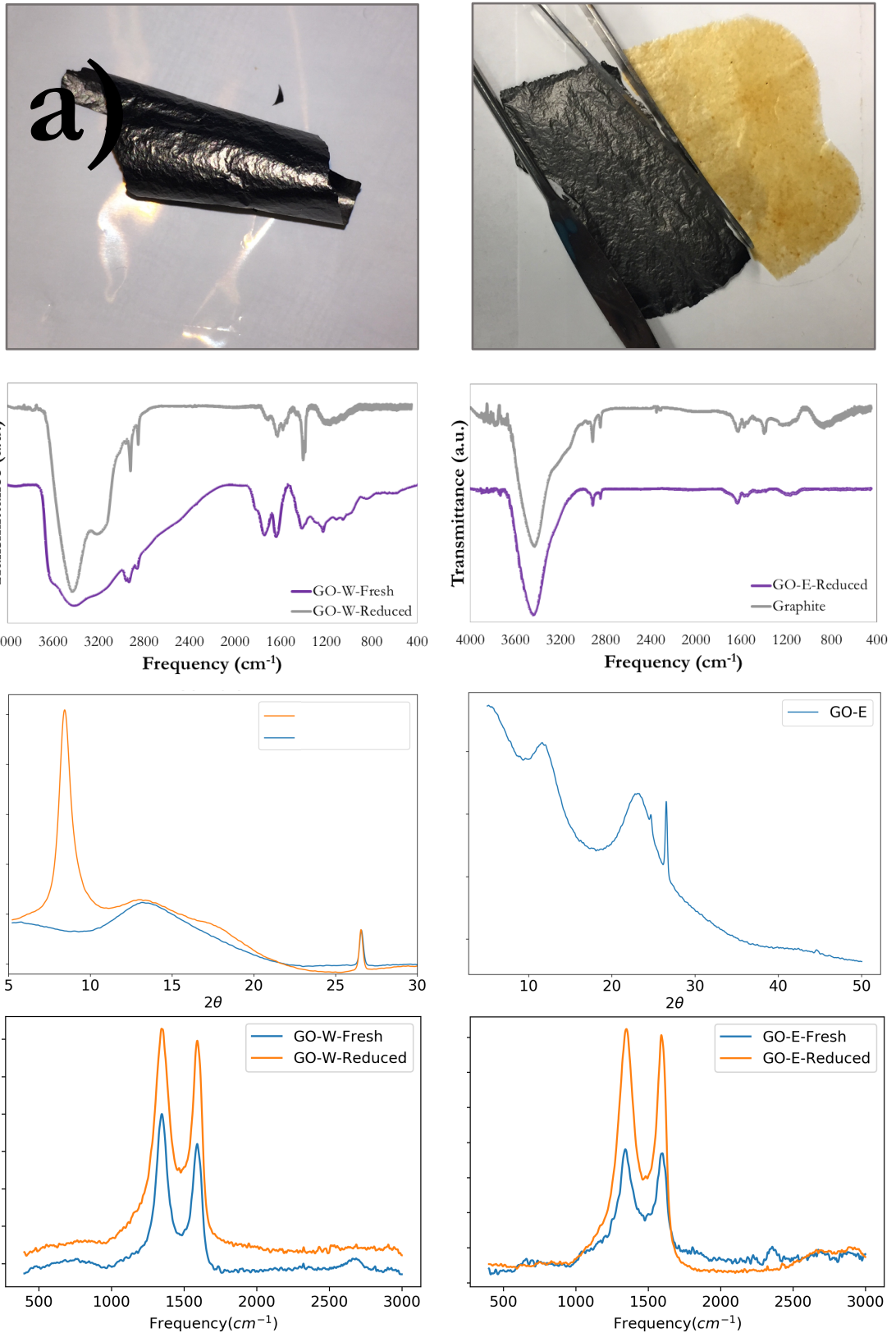
As shown in **Figure 5.6c**, comparing FTIR spectra of GO-water membrane before and after reduction shows a decreased intensity of 1750 cm⁻¹ peak (C=O), which is a primary peak of GO, indicating that significant reduction has taken place. In addition, a stronger 1400 cm⁻¹ peak (C-C-C) indicates presence of more graphene domains. In **Figure 5.6d**, we compared FTIR spectra of reduced GO-ethanol membrane and graphite, where the FTIR spectra of both look similar, indicating very significant reduction. XRD is also indicative of a reduction in both cases. With GO-water membrane, as shown in **Figure 5.6e**, there is a broad peak around 14°, which corresponds to a d-spacing of 6.25 Å. In the case of GO-ethanol membrane, we observed two peaks, one around 12° and another around 24°, which correspond to 7 Å and 3.8 Å, respectively. This suggests that the membrane does not reduce uniformly at those conditions. With the more reduced nature of these GO films based on XRD, we believe that these membranes have a more crystalline carbon lattice after high temperature reduction, therefore we are at higher L_a values. The decrease in the I_D/I_G ratios in both cases of reduction indicate a more graphitic nature. All data is summarized in

Table 5.4.

Table 5.4: Summary of Raman and XRD data of membranes reduced at high temperature

Reduction Parameters		D-Spacing (Å)		I _D /I _G Ratios (Peak Integral)	
Reduction	Membrane	Before	After	Before	After
200 °C for 1 hour	GO-Water	10.45	6.25	2.00	1.83
250 °C for 1 hour	GO-Ethanol	10.92	3.8, 7	1.82	1.73

Based on the XRD analysis of high-temperature reduction process, we observe that the interlayer spacing is not large enough to allow water permeation through GO membrane. Another drawback of the high-temperature reduction is that the membranes also lose mechanical integrity. Therefore, the high-temperature reduction is not optimal for PV. However, the low-temperature process can be further optimized to get ideal interlayer spacing for PV.



5.3 Langmuir-Blodgett Monolayers

The Langmuir-Blodgett (LB) deposition technique has been widely used to deposit a variety of nanomaterials, such as nanoparticles, nanorods, nanowires, nanotubes, and nanosheets [102]. In particular, LB is interesting for graphene oxide nanosheets and other 2D materials due to the potential of these 2D materials in applications such as flexible and transparent electronics, blocking layers, and selectively membranes.

Our initial aim with the LB process was to deposit monolayers of GO on a desired substrate to a desired thickness by controlling the number of depositions. This way, we are able to achieve ultrathin GO membranes that can achieve high flux. Luzhu Xu from our group pioneered the LB work of GO deposition on hard substrates, like mica and silicon. She has also been able to adapt the LB process to do a continuous deposition process, which is extremely valuable for large-scale membrane production [103]. The LB deposition process described below is adapted from Luzhu's work. Here we expand on the solvents used as dispersing media for GO to compare the qualities of the films, as well as extend the deposition to porous substrates for further scalability options.

LB generally requires a dispersion of the desired 2D material in a volatile water-immiscible solvent. This dispersion is spread on the air-water interface, the solvent evaporates, subsequently leaving the 2D materials suspended at the air-water interface. Usually, movable barriers are utilized in compressing the 2D materials at the air-water interface, resulting in a dense film of monolayer thickness. The dispersion is crucial for LB to work well, since the composition of the dispersion dictates the transfer of material on the air-water interface. A dispersion with a water-miscible solvent, once introduced at the air-water interface, results in extensive mixing and in loss of 2D materials to the water sub-phase. As discussed in **1.1.3**, the solvents that host stable dispersions of graphene oxide are water and other polar solvents. Thus, for a successful LB deposition of graphene oxide, the dispersing media needs to be optimized to be a mix of a polar solvent that hosts a stable dispersion of GO, and a highly volatile water-immiscible solvent for easy evaporation.

In our case, the polar solvents that we found to host stable dispersions were ethanol, 1-propanol, 1-butanol, and 1-hexanol. 1,2-Dichloroethane (DCE) has been successfully used as the water-immiscible solvent for LB deposition of graphene oxide. Our optimal mixture involved a 1:13 ratio of polar

solvent to DCE to prevent mixing with the water sub-phase. We ran LB depositions with all four alcohols; ethanol, 1-propanol, 1-butanol, and 1-hexanol, at 1:13 ratio with DCE.

5.3.1 LB Deposition

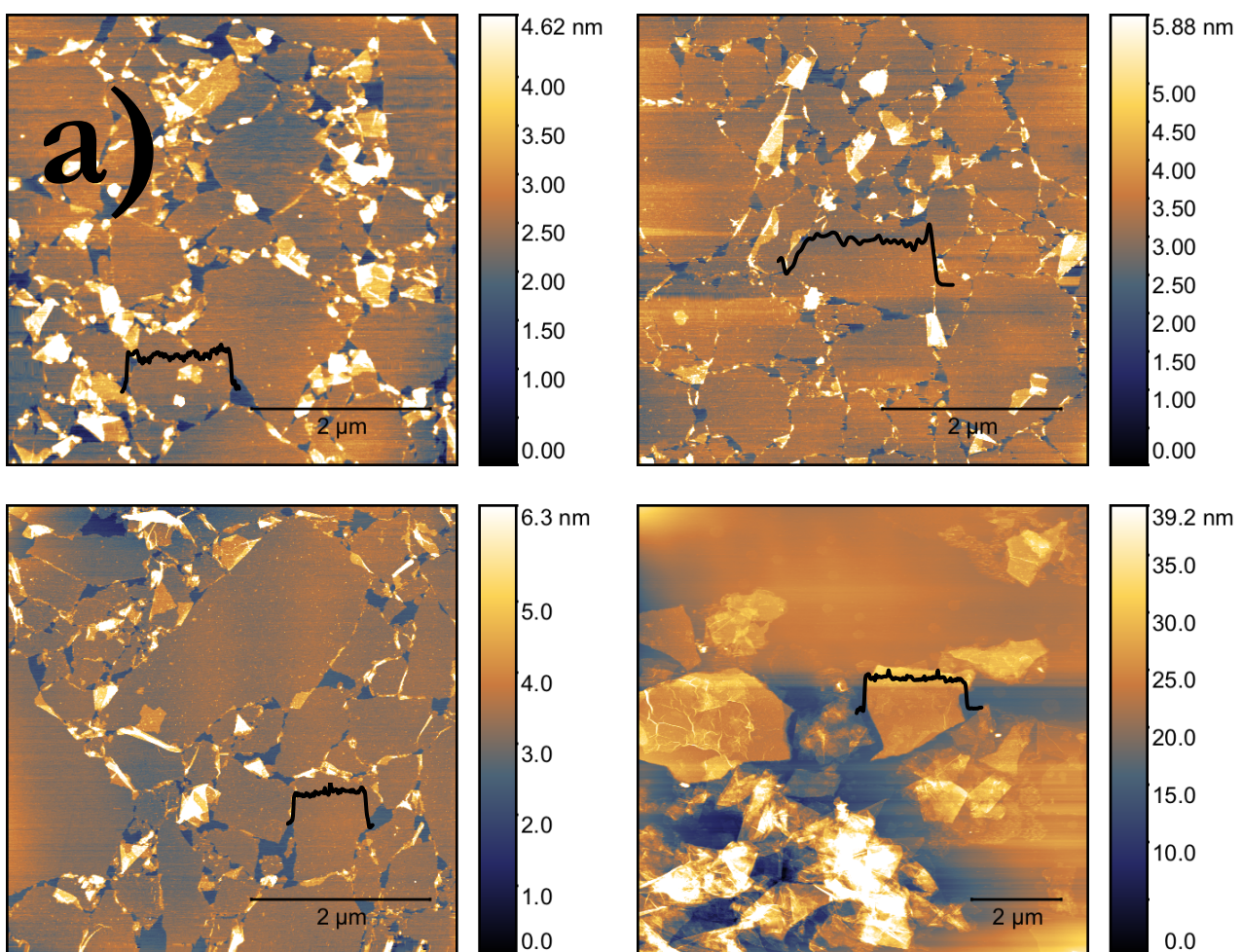
We designed an LB trough from Teflon, with a deposition area of 17 cm by 12 cm, and depth of 5 mm. Before the deposition, the trough is prepared by wiping it clean with DCE and water, filling the trough up with 180 mL of water, and then immersing our substrates (mica and silicon wafers) for deposition. Then we make the solution as described before, with the 1:13 polar solvent to DCE ratio of GO at 0.00625 mg/mL. This concentration was chosen because it makes the most uniform film.

Figure 5.7 shows the deposition setup, the trough loaded with substrates and the syringe position. The syringe needs to be placed only a few millimeters above the water surface, to ensure that the solution drops have enough room to be airborne for some distance. Having the syringe too far up causes the drops to fall too hard, which causes the drop to sink instead of spreading on the water surface.



We tested the LB process with all the 1-alcohol systems at the ratio of 1:13 1-alcohol to DCE at 0.00625 mg/mL of GO dispersion. We have observed that the film formation mechanism is as the drop spreads onto the air-water interface, the solvent evaporates, leaving GO flakes suspended. With each drop, GO flakes are deposited, and pushed out from the center of the trough towards the edges. This is continued until the entire trough surface is full, which is indicated by no further spreading of the solvent. Once the trough is filled with GO flakes, we draw out the water and deposit the GO film onto the substrates. The deposited films are characterized by AFM, as shown in **Figure 5.8**.

GO films prepared from ethanol (**Figure 5.8a**), 1-propanol (**Figure 5.8b**), and 1-butanol (**Figure 5.8c**) were uniformly coated and not aggregated. However, the GO film from 1-hexanol (**Figure 5.8d**) This is probably due to the high boiling point of 1-hexanol, which does not allow 1-hexanol to evaporate from the air-water interface during the deposition, and the GO aggregates as the 1-hexanol evaporates slowly. We compared LB films to spin-coated GO films to see if there was a lateral size selectivity issue with LB or spin-coating. Histograms in **Figure 5.9** show the analysis of the lateral sheet distribution, which were carried out with ImageJ.

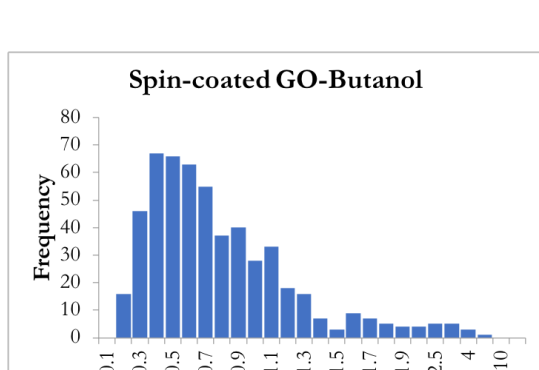
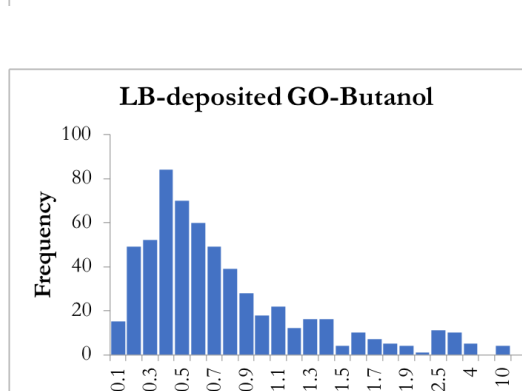
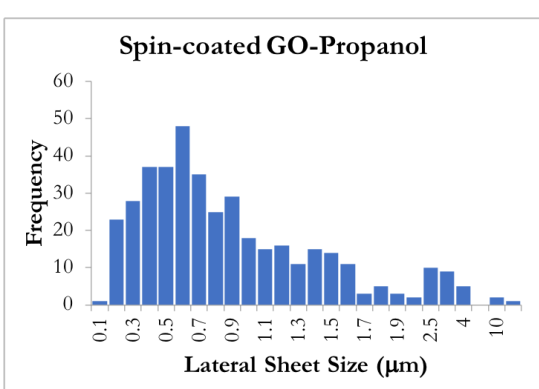
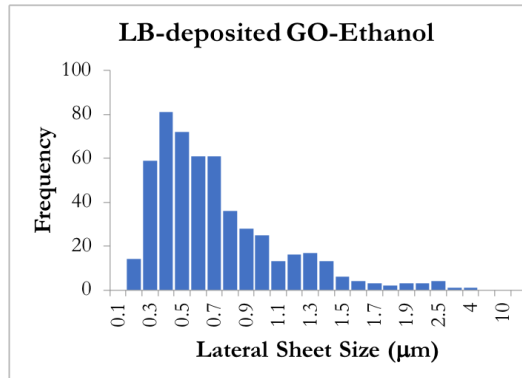
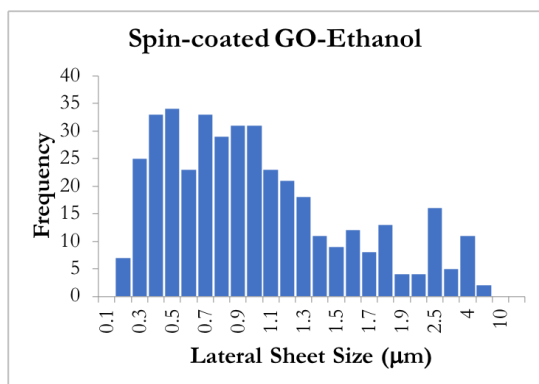
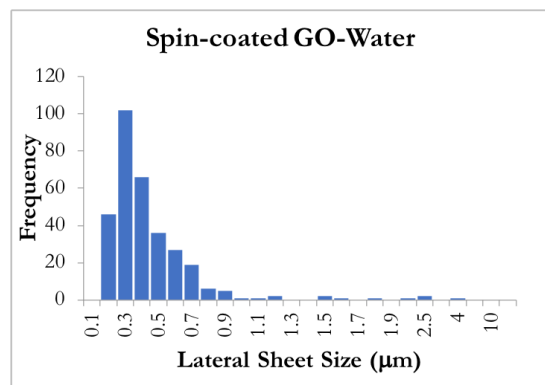


With both LB and spin-coating, we observed a large sheet size distribution in the cases of 1-alcohols. However, the water system did not have as large of a distribution. Also, the average value of the sheet sizes in the water system was notably smaller than the 1-alcohol systems, which agrees with our earlier DLS data and PLM. **Table 5.5** gives the average values and standard deviations of the lateral sheet size distributions in spin-coated and LB-deposited samples. LB deposition cannot be carried out with the water system because water and DCE are immiscible, so the GO dispersion would not be stable. Similarly, 1-hexanol is incompatible with LB due to the low evaporation rate. We were also unable to create spin-coated samples from 1-hexanol because it did not wet the silicon wafers, even with surface treatment.

Table 5.5: Average and standard deviation in the measurement of lateral sheet sizes with spin-coating and LB GO films

Solvent	Spin-coating		LB	
	Average (nm)	Deviation (nm)	Average (nm)	Deviation (nm)
Water	403	334	NA	NA
Ethanol	1010	700	663	411
1-Propanol	891	749	650	501
1-Butanol	751	515	752	780
1-Hexanol	NA	NA	NA	NA

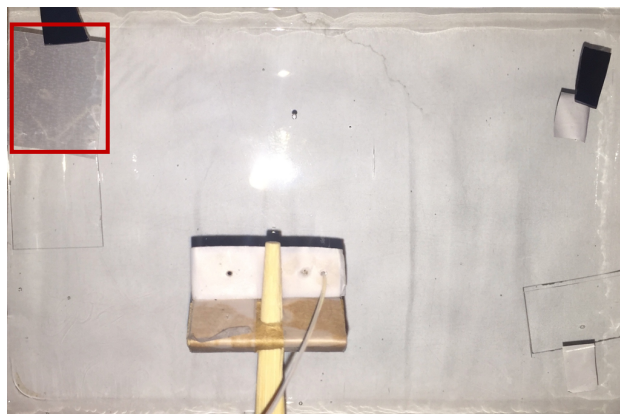
Comparing spin-coating and LB average sheet sizes, we observe that they are in the same range, which suggests that there is no size selectivity with the two techniques.



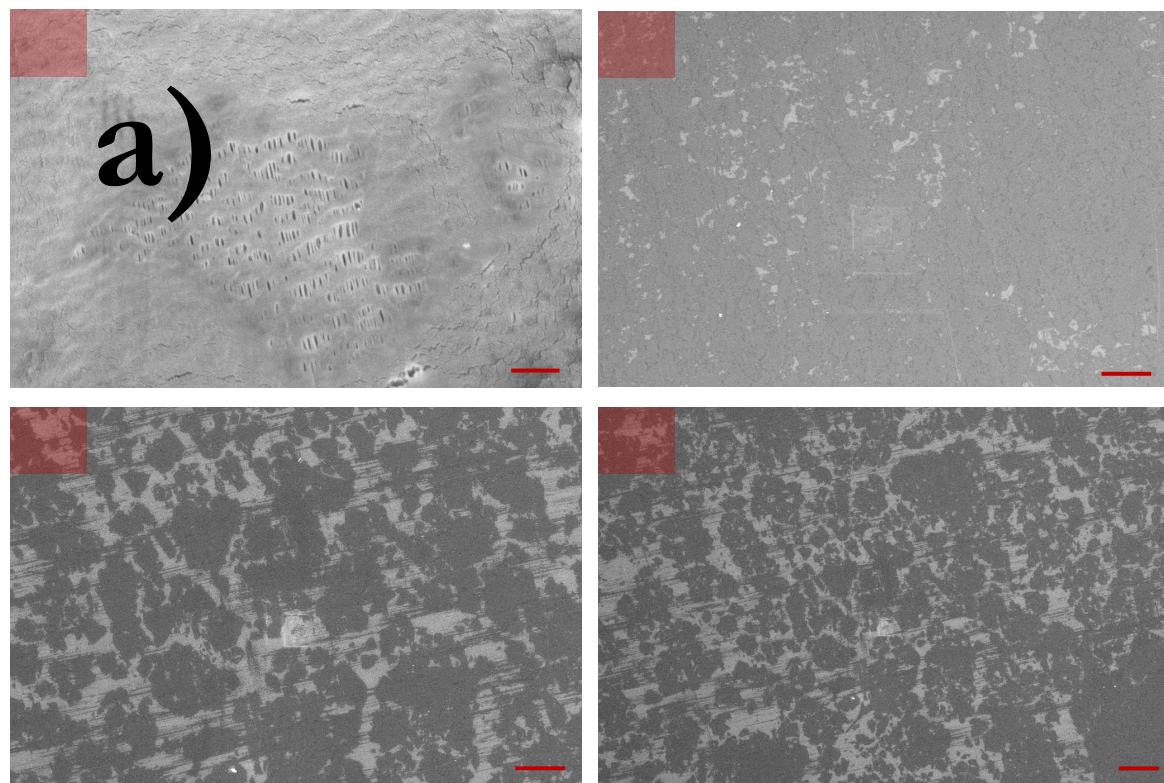
5.3.2 Extending LB Depositions to Polymeric Substrates

As mentioned earlier, depositing on hard substrates such as mica and silicon had been done before, therefore, we wanted to try the LB deposition on porous polymeric substrates to extend the practicality of LB for PV membranes. The LB trough is shown in **Figure 5.10**, loaded with the PP porous membrane used previously in **4.3** in the red rectangle.

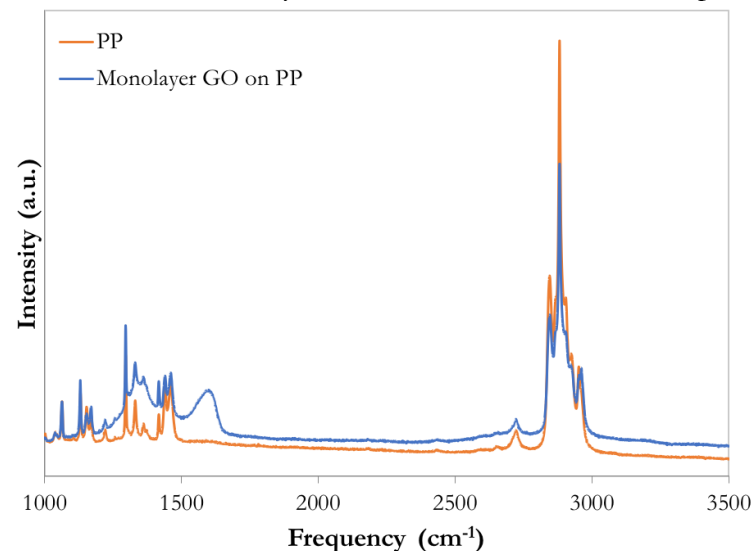
We attempted to deposit a monolayer of GO on porous PP membranes, which are extremely hydrophobic. The hydrophobicity forces the membrane to not stay submerged in the trough, which if not properly pressed down, could float up during the deposition. We could not use any tapes or adhesives because that could contaminate the water surface, affecting the deposition. A simple solution to this problem was to use other substrates to keep the PP immersed. This limited us to use smaller membrane areas to ensure that the PP membrane will not surface during the deposition time.



As we did earlier with the cast films, we could also treat the surface of the PP with the plasma cleaner to make it more hydrophilic during the time of the deposition, to be able to deposit a larger area. **Figure 5.11a-b** are SEM micrographs of the monolayer GO on PP at higher magnification (**Figure 5.11a**) and lower magnification (**Figure 5.11b**), where an almost 100% coverage is observed. **Figure 5.11c-d** are SEM micrographs of reduced GO on PP, which was obtained via a 15-minute chemical reduction with 50 mM NaBH₄ at 50 C. In this case, we observe a decent coverage.



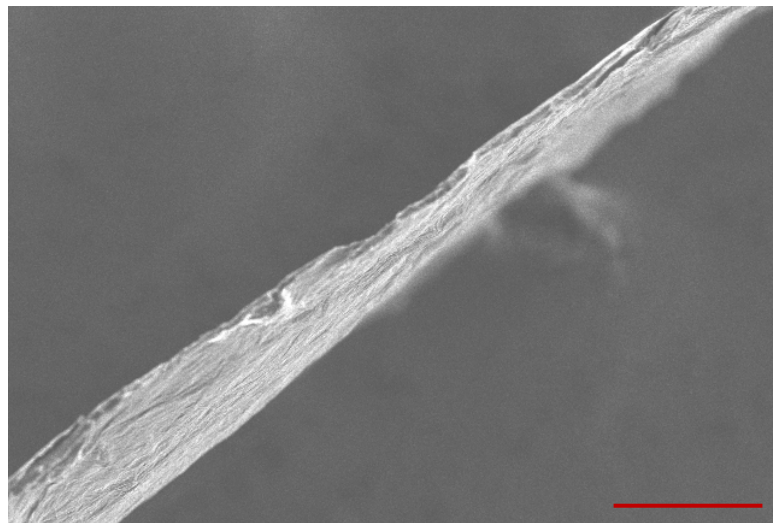
The LB-deposited PP film was quickly tested with Raman spectroscopy. **Figure 5.12** shows the Raman spectra of bare PP and PP with a monolayer of GO. We observed the G peak in the GO sample



c)

around 1600 cm^{-1} , but the D peak is convoluted with the PP peaks. The presence of G peak indicates that we have GO deposited on PP.

Here in this chapter, we have shown that we can successfully cast films from water and 1-alcohol dispersions as well as do an LB-deposition on porous membranes. However, we have not been able to use these membranes for PV. The issue with the cast films is the thickness, as shown in **Figure 5.13**, the cast films thickness ranges from 25-40 μm . The LB deposited films also required a lot of



optimization to properly tune the coverage and the quality of the film. We were not able to tackle all these issues in the time frame required, therefore, these membranes have not been tested with PV to compare the performance of these membrane with the vacuum-filtered GO membranes.

5.4 Conclusions

In this chapter, we have been able to extend solution casting and LB deposition techniques in the cases of the 1-alcohols, which has not been realized before. The cast films deposited on PP turned out to be freestanding, which are extremely valuable for various applications. We characterized the film quality with Raman, XRD, FTIR, and AFM. Based on the XRD results, we observed that the cast films have a different d-spacing based on the solvents, similar to the vacuum-filtered films that were used in PV.

In an attempt to motivate the use of 1-alcohol GO membranes, we examined the effect of thermal and chemical reduction on the membranes. Based on our results, we have been able to achieve two extents of reduction with our thermal reduction process, which may be of interest for different purposes. With the lower temperature reduction, we remove oxygen functionalities but the d-spacing is 6A. This may be useful for better performing RO or PV membranes, where having a more reduced membrane will increase stability of the membrane while still maintaining an appropriate d-spacing for a high flux. With our high-temperature thermal reduction, we achieved a more reduced film, however, we lost the flexibility of the membrane, which may deem the membranes inadequate for most applications. Therefore, we show that with the chemical reduction method, the membrane may be able to maintain its flexibility, which is important.

With our LB deposited films, we show that the quality of the deposition is excellent with ethanol, 1-propanol, and 1-butanol systems. We performed a thorough analysis of the lateral sheet size distribution in each solvent system by comparing LB deposited films to spin-coated samples. Analyzing the AFM micrographs from the spin-coated samples, we observe a much smaller average lateral sheet size for the water system, which is in accordance with our DLS and PLM data. The smaller sheet sizes, again, indicate the effect of the chemical transformation of GO that takes place in water.

On the whole, the motivation for studying cast GO films and LB films was to be able to expand the use of GO in different applications. Cast GO films have improved crystallinity compared to vacuum filtered films, which has been shown improve their performance compared to conventional films. With the LB deposition on porous polymeric substrates, we have facilitated the deposition of controlled thickness of GO films, down to a monolayer.

6 Conclusions and Future Work

6.1 Summary of Main Findings

Through this work, we have been able to show some exciting findings. First of all, with respect to GO dispersions, we have successfully shown that low-molecular-weight 1-alcohols can host stable dispersions of GO. In doing so, we have improved the possibility of solution processing of GO for large-scale commercial applications.

We also thoroughly studied the solvent-dependent properties of GO, in dispersion state and in films. We have found that GO dispersions are sensitive to light and moisture exposure, where light causes a more dramatic chemical transformation compared to moisture. We observed that GO flakes in aqueous dispersions go through the most chemical transformation due to the nucleophilic nature of the water molecules, resulting in GO flakes breakage. The average flake size in GO-water is much smaller than the ones in 1-alcohols, which is not desirable for applications in sensing, electronics, or filtration.

As a result of investigating the colloidal stability of GO dispersions, we came across the property of liquid crystallinity that was observed in the 1-alcohols dispersions for the first time. The property of liquid crystallinity can be utilized to make better-performing membranes, which we used in creating cast films with high crystallinity.

We also showed successful creation of custom-made PV modules with acrylic and stainless steel, both of which performed similar to a commercial PV module. With our vacuum-filtered GO membranes with varying interlayer distance and nanochannel chemistry, the optimal performance was achieved by 1-propanol, which achieved better flux than the state-of-the-art GO membranes in PV.

With our custom-made PV modules, we observed an interesting transport phenomenon across the GO membrane, which had not been discussed before. We observed that water permeation across the membrane not only depended on the GO layer but also on the polymer support layer. Based on our limited results, we were able to point the differences to the porosity and hydrophobicity of the membrane. We observed that porosity was the largest factor in the permeation differences.

We were also able to achieve uniform LB-deposited films from GO dispersions of 1-alcohols for the first time. In addition to the LB deposition on porous polymeric substrates, we have facilitated the deposition of controlled thickness of GO films, down to a monolayer. This enables the possibility of ultrathin membranes for PV, which with the optimal parameters can boost the flux and rejection of PV membranes.

6.2 Recommendations for Future Work

This work serves only as groundwork in the field of 1-alcohols GO dispersions. The dispersion properties suggest that these 1-alcohol solvents will be a necessary replacement for the aqueous dispersion to overcome the chemical transformation, thus minimizing the time and effort required for repetitive synthesis and characterization of GO stocks. An important property that was not studied in this report would be the concentration effect of these dispersions. Based on preliminary observations, there seemed to be a dependence of the dispersion concentration to rate of aging. This may be worth looking into for optimization of storage conditions.

In terms of the GO vacuum-filtered membranes, as seen by the SEM micrographs, these membranes have a very high surface roughness, especially in the cases of 1-alcohols. Using pressure-filtration instead of vacuum filtration, which results in better film crystallinity, has shown improved performance in other applications. Therefore, it may also be worthwhile for PV membranes. Ultimately, we could use the cast membranes, which are highly crystalline. However, the issue with cast membranes is making few-hundred-nanometer thick membranes instead of tens of micron thick. LB should also be explored as a viable option for the possibility of ultrathin GO membranes.

In addition to the crystallinity factor, the interlayer spacing and the level of GO functionality can also be tuned to optimize the PV membrane. As suggested by MD simulation results, partial reduction of GO membranes may result in higher flux. PV module has been improved for better flow dynamics and permeate collection. However, it still remains to be properly optimized for higher temperatures. Therefore, making a stainless-steel membrane cell with similar flow dynamics as iteration 3 may result in steady flux at higher temperatures.

7 References

- [1] A. Khatri, “Overview on Nanotechnology: The Future of Seawater Desalination.”
- [2] A. Shrivastava, S. Rosenberg, and M. Peery, “Energy efficiency breakdown of reverse osmosis and its implications on future innovation roadmap for desalination,” *Desalination*, vol. 368, pp. 181–192, Jul. 2015.
- [3] M. Elimelech and W. A. Phillip, “The future of seawater desalination: energy, technology, and the environment,” *science*, vol. 333, no. 6043, pp. 712–717, 2011.
- [4] “Water Scarcity Index | GRID-Arendal.” [Online]. Available: <http://www.grida.no/resources/5586>. [Accessed: 01-Sep-2017].
- [5] “Desalination by the Numbers | IDA,” *International Desalination Association*. [Online]. Available: <http://idadesal.org/desalination-101/desalination-by-the-numbers/>. [Accessed: 07-Jul-2018].
- [6] “Innovators Are Chasing a Cheaper Future for Desalination.” [Online]. Available: <https://nextcity.org/daily/entry/drought-resilience-desalination-plant-california>. [Accessed: 01-Sep-2017].
- [7] A. Al-Zahrani, J. Orfi, Z. Al-Suhaibani, B. Salim, and H. Al-Ansary, “Thermodynamic Analysis of a Reverse Osmosis Desalination Unit with Energy Recovery System,” *Procedia Engineering*, vol. 33, pp. 404–414, 2012.
- [8] E. L. Cussler and B. K. Dutta, “On separation efficiency,” *AIChE J.*, vol. 58, no. 12, pp. 3825–3831, Dec. 2012.
- [9] K. Mistry and J. Lienhard, “Generalized Least Energy of Separation for Desalination and Other Chemical Separation Processes,” *Entropy*, vol. 15, no. 6, pp. 2046–2080, May 2013.
- [10] C. Liu, K. Rainwater, and L. Song, “Energy analysis and efficiency assessment of reverse osmosis desalination process,” *Desalination*, vol. 276, no. 1–3, pp. 352–358, Aug. 2011.
- [11] “2.2 Desalination by distillation.” [Online]. Available: <https://www.oas.org/dsd/publications/Unit/oea59e/ch21.htm#2.2> desalination by distillation. [Accessed: 01-Sep-2017].
- [12] International Society of Offshore and Polar Engineers, “The proceedings of the eighth (2009) ISOPE Ocean Mining and Gas Hydrates Symposium (OMS 2009): Chennai, India, September 20-24, 2009.” ISOPE, 2009.

- [13] R. Semiat, “Energy Issues in Desalination Processes,” *Environmental Science & Technology*, vol. 42, no. 22, pp. 8193–8201, Nov. 2008.
- [14] H.-C. Huang and R. Xie, “New Osmosis Law and Theory: the New Formula that Replaces van’t Hoff Osmotic Pressure Equation,” *arXiv:1201.0912 [q-bio]*, Jan. 2012.
- [15] J. Imbrogno, J. J. Keating, J. Kilduff, and G. Belfort, “Critical aspects of RO desalination: A combination strategy,” *Desalination*, vol. 401, pp. 68–87, Jan. 2017.
- [16] J. G. Crespo and C. Brazinha, “Fundamentals of pervaporation,” in *Pervaporation, Vapour Permeation and Membrane Distillation*, Elsevier, 2015, pp. 3–17.
- [17] X. Feng and R. Y. Huang, “Liquid separation by membrane pervaporation: a review,” *Industrial & Engineering Chemistry Research*, vol. 36, no. 4, pp. 1048–1066, 1997.
- [18] P. Shao and R. Y. M. Huang, “Polymeric membrane pervaporation,” *Journal of Membrane Science*, vol. 287, no. 2, pp. 162–179, Jan. 2007.
- [19] A. A. Babalou, N. Rafia, and K. Ghasemzadeh, “Integrated systems involving pervaporation and applications,” in *Pervaporation, Vapour Permeation and Membrane Distillation*, Elsevier, 2015, pp. 65–86.
- [20] Q. Wang, N. Li, B. Bolto, M. Hoang, and Z. Xie, “Desalination by pervaporation: A review,” *Desalination*, vol. 387, pp. 46–60, Jun. 2016.
- [21] W. Ho and K. Sirkar, *Membrane Handbook*. Springer US, 1992.
- [22] E. Drioli, A. I. Stankiewicz, and F. Macedonio, “Membrane engineering in process intensification—An overview,” *Journal of Membrane Science*, vol. 380, no. 1–2, pp. 1–8, Sep. 2011.
- [23] S.-J. Park *et al.*, “Aromatic solvent-assisted interfacial polymerization to prepare high performance thin film composite reverse osmosis membranes based on hydrophilic supports,” *Polymer*, vol. 144, pp. 159–167, May 2018.
- [24] Y. You, V. Sahajwalla, M. Yoshimura, and R. K. Joshi, “Graphene and graphene oxide for desalination,” *Nanoscale*, vol. 8, no. 1, pp. 117–119, 2016.
- [25] N. Wei, X. Peng, and Z. Xu, “Understanding Water Permeation in Graphene Oxide Membranes,” *ACS Applied Materials & Interfaces*, vol. 6, no. 8, pp. 5877–5883, Apr. 2014.
- [26] J. R. Werber, C. O. Osuji, and M. Elimelech, “Materials for next-generation desalination and water purification membranes,” *Nature Reviews Materials*, vol. 1, no. 5, p. 16018, Apr. 2016.
- [27] S. Ray, *Applications of Graphene and Graphene-Oxide based Nanomaterials*, 1st ed. 2015.
- [28] M. S. Khan, A. Shakoor, G. T. Khan, S. Sultana, and A. Zia, “A Study of Stable Graphene Oxide Dispersions in Various Solvents.,” *Journal of the Chemical Society of Pakistan*, vol. 37, no. 1, 2015.

- [29] L. Wang, M. S. H. Boutilier, P. R. Kidambi, D. Jang, N. G. Hadjiconstantinou, and R. Karnik, “Fundamental transport mechanisms, fabrication and potential applications of nanoporous atomically thin membranes,” *Nature Nanotechnology*, vol. 12, no. 6, pp. 509–522, Jun. 2017.
- [30] D. Cohen-Tanugi, L.-C. Lin, and J. C. Grossman, “Multilayer Nanoporous Graphene Membranes for Water Desalination,” *Nano Letters*, vol. 16, no. 2, pp. 1027–1033, Feb. 2016.
- [31] A. N. J. Rodgers, M. Velický, and R. A. W. Dryfe, “Electrostatic Stabilization of Graphene in Organic Dispersions,” *Langmuir*, vol. 31, no. 48, pp. 13068–13076, Dec. 2015.
- [32] D. W. Johnson, B. P. Dobson, and K. S. Coleman, “A manufacturing perspective on graphene dispersions,” *Current Opinion in Colloid & Interface Science*, vol. 20, no. 5–6, pp. 367–382, Oct. 2015.
- [33] S. Safaei and R. Tavakoli, “On the design of graphene oxide nanosheets membranes for water desalination,” *Desalination*, vol. 422, pp. 83–90, Nov. 2017.
- [34] J. Zhang, S. Seyedin, Z. Gu, N. Salim, X. Wang, and J. M. Razal, “Liquid Crystals of Graphene Oxide: A Route Towards Solution-Based Processing and Applications,” *Part. Part. Syst. Charact.*, vol. 34, no. 9, p. n/a-n/a, Sep. 2017.
- [35] A. O'Neill, U. Khan, P. N. Nirmalraj, J. Boland, and J. N. Coleman, “Graphene Dispersion and Exfoliation in Low Boiling Point Solvents,” *The Journal of Physical Chemistry C*, vol. 115, no. 13, pp. 5422–5428, Apr. 2011.
- [36] J. I. Paredes, S. Villar-Rodil, A. Martínez-Alonso, and J. M. D. Tascón, “Graphene Oxide Dispersions in Organic Solvents,” *Langmuir*, vol. 24, no. 19, pp. 10560–10564, Oct. 2008.
- [37] J. Texter, “Graphene dispersions,” *Current Opinion in Colloid & Interface Science*, vol. 19, no. 2, pp. 163–174, Apr. 2014.
- [38] D. Konios, M. M. Stylianakis, E. Stratakis, and E. Kymakis, “Dispersion behaviour of graphene oxide and reduced graphene oxide,” *Journal of Colloid and Interface Science*, vol. 430, pp. 108–112, Sep. 2014.
- [39] J. Taha-Tijerina *et al.*, “Quantification of the Particle Size and Stability of Graphene Oxide in a Variety of Solvents,” *Particle & Particle Systems Characterization*, vol. 32, no. 3, pp. 334–339, Mar. 2015.
- [40] M. Liu, Z. Chen, S. Yu, D. Wu, and C. Gao, “Thin-film composite polyamide reverse osmosis membranes with improved acid stability and chlorine resistance by coating N-isopropylacrylamide-co-acrylamide copolymers,” *Desalination*, vol. 270, no. 1–3, pp. 248–257, Apr. 2011.

- [41] W. Xie, G. M. Geise, B. D. Freeman, H.-S. Lee, G. Byun, and J. E. McGrath, “Polyamide interfacial composite membranes prepared from m-phenylene diamine, trimesoyl chloride and a new disulfonated diamine,” *Journal of Membrane Science*, vol. 403–404, pp. 152–161, Jun. 2012.
- [42] D. L. Shaffer, J. R. Werber, H. Jaramillo, S. Lin, and M. Elimelech, “Forward osmosis: Where are we now?,” *Desalination*, vol. 356, pp. 271–284, Jan. 2015.
- [43] P. Li, “Pervaporation: An Emerging Technology for Desalination,” *Polymer science*, vol. 2, no. 1, 2016.
- [44] K. M. Gupta, Z. Qiao, K. Zhang, and J. Jiang, “Seawater Pervaporation through Zeolitic Imidazolate Framework Membranes: Atomistic Simulation Study,” *ACS Applied Materials & Interfaces*, vol. 8, no. 21, pp. 13392–13399, Jun. 2016.
- [45] J. R. Werber, A. Deshmukh, and M. Elimelech, “The Critical Need for Increased Selectivity, Not Increased Water Permeability, for Desalination Membranes,” *Environ. Sci. Technol. Lett.*, vol. 3, no. 4, pp. 112–120, Apr. 2016.
- [46] M. A. Shannon, P. W. Bohn, M. Elimelech, J. G. Georgiadis, B. J. Mariñas, and A. M. Mayes, “Science and technology for water purification in the coming decades,” *Nature*, vol. 452, no. 7185, pp. 301–310, Mar. 2008.
- [47] G. Jyoti, A. Keshav, and J. Anandkumar, “Review on Pervaporation: Theory, Membrane Performance, and Application to Intensification of Esterification Reaction,” *Journal of Engineering*, vol. 2015, pp. 1–24, 2015.
- [48] B. Liang *et al.*, “High performance graphene oxide/polyacrylonitrile composite pervaporation membranes for desalination applications,” *J. Mater. Chem. A*, vol. 3, no. 9, pp. 5140–5147, 2015.
- [49] Q. Wang, N. Li, B. Bolto, M. Hoang, and Z. Xie, “Desalination by pervaporation: A review,” *Desalination*, vol. 387, pp. 46–60, Jun. 2016.
- [50] M. Paulauskas, “Pervaporation Using Graphene Oxide Membranes,” University of Leeds, 2015.
- [51] A. K. Pabby, S. S. H. Rizvi, and A. M. S. Requena, *Handbook of Membrane Separations: Chemical, Pharmaceutical, Food, and Biotechnological Applications*. Taylor & Francis, 2008.
- [52] T. Okada, M. Yoshikawa, and T. Matsuura, “A study on the pervaporation of ethanol/water mixtures on the basis of pore flow model,” *Journal of Membrane Science*, vol. 59, no. 2, pp. 151–168, Jun. 1991.
- [53] T. Okada and T. Matsuura, “A new transport model for pervaporation,” *Journal of Membrane Science*, vol. 59, no. 2, pp. 133–149, Jun. 1991.

- [54] X. Feng and R. Y. Huang, “Liquid separation by membrane pervaporation: a review,” *Industrial & Engineering Chemistry Research*, vol. 36, no. 4, pp. 1048–1066, 1997.
- [55] A. Figoli, S. Santoro, F. Galiano, and A. Basile, “Pervaporation membranes,” in *Pervaporation, Vapour Permeation and Membrane Distillation*, Elsevier, 2015, pp. 19–63.
- [56] J. Y. Chong, B. Wang, and K. Li, “Water transport through graphene oxide membranes: the roles of driving forces,” *Chemical Communications*, vol. 54, no. 20, pp. 2554–2557, 2018.
- [57] A. Sagle and B. Freeman, “Fundamentals of membranes for water treatment,” *the future of desalination in Texas*, vol. 2, pp. 137–154, 2004.
- [58] K. Goh *et al.*, “All-Carbon Nanoarchitectures as High-Performance Separation Membranes with Superior Stability,” *Adv. Funct. Mater.*, vol. 25, no. 47, pp. 7348–7359, Dec. 2015.
- [59] R. Li, L. Zhang, and P. Wang, “Rational design of nanomaterials for water treatment,” *Nanoscale*, vol. 7, no. 41, pp. 17167–17194, 2015.
- [60] J. Yin, E.-S. Kim, J. Yang, and B. Deng, “Fabrication of a novel thin-film nanocomposite (TFN) membrane containing MCM-41 silica nanoparticles (NPs) for water purification,” *Journal of Membrane Science*, vol. 423–424, pp. 238–246, Dec. 2012.
- [61] A. S. Al-Hobaib, K. M. Al-Sheetan, M. R. Shaik, and M. S. Al-Suhybani, “Modification of thin-film polyamide membrane with multi-walled carbon nanotubes by interfacial polymerization,” *Applied Water Science*, Jun. 2017.
- [62] A. M. Dimiev and S. Eigler, *Graphene Oxide: Fundamentals and Applications*. John Wiley & Sons, 2016.
- [63] D. R. Dreyer, S. Park, C. W. Bielawski, and R. S. Ruoff, “The chemistry of graphene oxide,” *Chem. Soc. Rev.*, vol. 39, no. 1, pp. 228–240, 2010.
- [64] A. Dimiev, D. V. Kosynkin, L. B. Alemany, P. Chaguine, and J. M. Tour, “Pristine Graphite Oxide,” *Journal of the American Chemical Society*, vol. 134, no. 5, pp. 2815–2822, Feb. 2012.
- [65] B. Chen, H. Jiang, X. Liu, and X. Hu, “Observation and Analysis of Water Transport through Graphene Oxide Interlamination,” *The Journal of Physical Chemistry C*, vol. 121, no. 2, pp. 1321–1328, Jan. 2017.
- [66] J. Deng, Y. You, H. Bustamante, V. Sahajwalla, and R. K. Joshi, “Mechanism of water transport in graphene oxide laminates,” *Chem. Sci.*, vol. 8, no. 3, pp. 1701–1704, 2017.
- [67] B. Chen, H. Jiang, X. Liu, and X. Hu, “Molecular Insight into Water Desalination across Multilayer Graphene Oxide Membranes,” *ACS Applied Materials & Interfaces*, vol. 9, no. 27, pp. 22826–22836, Jul. 2017.

- [68] M. Hu and B. Mi, “Enabling Graphene Oxide Nanosheets as Water Separation Membranes,” *Environmental Science & Technology*, vol. 47, no. 8, pp. 3715–3723, Apr. 2013.
- [69] J. Abraham *et al.*, “Tunable sieving of ions using graphene oxide membranes,” *Nature Nanotechnology*, vol. 12, no. 6, pp. 546–550, Apr. 2017.
- [70] C. Cheng, L. Shen, X. Yu, Y. Yang, X. Li, and X. Wang, “Robust construction of a graphene oxide barrier layer on a nanofibrous substrate assisted by the flexible poly(vinylalcohol) for efficient pervaporation desalination,” *J. Mater. Chem. A*, 2017.
- [71] F. U. Nigiz and N. D. Hilmioğlu, “Pervaporative desalination of seawater by using composite and blended poly(vinyl alcohol) membranes,” *Desalination and Water Treatment*, vol. 57, no. 11, pp. 4749–4755, Mar. 2016.
- [72] B. Liang, K. Pan, L. Li, E. P. Giannelis, and B. Cao, “High performance hydrophilic pervaporation composite membranes for water desalination,” *Desalination*, vol. 347, pp. 199–206, Aug. 2014.
- [73] L. Chen *et al.*, “High performance graphene oxide nanofiltration membrane prepared by electrospraying for wastewater purification,” *Carbon*, vol. 130, pp. 487–494, Apr. 2018.
- [74] M. M. Gudarzi, M. H. M. Moghadam, and F. Sharif, “Spontaneous exfoliation of graphite oxide in polar aprotic solvents as the route to produce graphene oxide – organic solvents liquid crystals,” *Carbon*, vol. 64, pp. 403–415, Nov. 2013.
- [75] M. M. Gudarzi, “Colloidal Stability of Graphene Oxide: Aggregation in Two Dimensions,” *Langmuir*, vol. 32, no. 20, pp. 5058–5068, May 2016.
- [76] R. T. M. Ahmad, S.-H. Hong, T.-Z. Shen, and J.-K. Song, “Water-assisted stable dispersal of graphene oxide in non-dispersible solvents and skin formation on the GO dispersion,” *Carbon*, vol. 98, pp. 188–194, Mar. 2016.
- [77] A. M. Dimiev, L. B. Alemany, and J. M. Tour, “Graphene Oxide. Origin of Acidity, Its Instability in Water, and a New Dynamic Structural Model,” *ACS Nano*, vol. 7, no. 1, pp. 576–588, Jan. 2013.
- [78] V. V. Neklyudov, N. R. Khafizov, I. A. Sedov, and A. M. Dimiev, “New insights into the solubility of graphene oxide in water and alcohols,” *Physical Chemistry Chemical Physics*, vol. 19, no. 26, pp. 17000–17008, 2017.
- [79] R. Jalili *et al.*, “Organic Solvent-Based Graphene Oxide Liquid Crystals: A Facile Route toward the Next Generation of Self-Assembled Layer-by-Layer Multifunctional 3D Architectures,” *ACS Nano*, vol. 7, no. 5, pp. 3981–3990, May 2013.

- [80] Y. H. Shim, K. E. Lee, T. J. Shin, S. O. Kim, and S. Y. Kim, “Wide concentration liquid crystallinity of graphene oxide aqueous suspensions with interacting polymers,” *Mater. Horiz.*, vol. 4, no. 6, pp. 1157–1164, 2017.
- [81] B. Dobias, X. Qiu, and W. von Rybinski, *Solid - Liquid Dispersions*. CRC Press, 1999.
- [82] “Zeta Potential Measurements of Non-Aqueous Particulate Suspensions,” Malvern Instruments Limited, Application Note AN101104, 2016.
- [83] G. V. Lowry *et al.*, “Guidance to improve the scientific value of zeta-potential measurements in nanoEHS,” *Environmental Science: Nano*, vol. 3, no. 5, pp. 953–965, 2016.
- [84] J. Zhang, S. Seyedin, Z. Gu, N. Salim, X. Wang, and J. M. Razal, “Liquid Crystals of Graphene Oxide: A Route Towards Solution-Based Processing and Applications,” *Particle & Particle Systems Characterization*, vol. 34, no. 9, p. 1600396, Sep. 2017.
- [85] J. C. Ramella-Roman, K. Lee, S. A. Prahl, and S. L. Jacques, “Polarized light imaging with a handheld camera,” 2003, pp. 284–293.
- [86] A. C. Ferrari and J. Robertson, “Interpretation of Raman spectra of disordered and amorphous carbon,” *Physical Review B*, vol. 61, no. 20, pp. 14095–14107, May 2000.
- [87] Z. Xu and C. Gao, “Aqueous Liquid Crystals of Graphene Oxide,” *ACS Nano*, vol. 5, no. 4, pp. 2908–2915, Apr. 2011.
- [88] A. R. Koltonow, C. Luo, J. Luo, and J. Huang, “Graphene Oxide Sheets in Solvents: To Crumple or Not To Crumple?,” *ACS Omega*, vol. 2, no. 11, pp. 8005–8009, Nov. 2017.
- [89] G.-W. Zhou *et al.*, “Facile Spray Drying Route for the Three-Dimensional Graphene-Encapsulated Fe₂O₃ Nanoparticles for Lithium Ion Battery Anodes,” *Industrial & Engineering Chemistry Research*, vol. 52, no. 3, pp. 1197–1204, Jan. 2013.
- [90] U. Khan, A. O’Neill, M. Lotya, S. De, and J. N. Coleman, “High-Concentration Solvent Exfoliation of Graphene,” *Small*, vol. 6, no. 7, pp. 864–871, Apr. 2010.
- [91] “Sterlitech CF042A cross-flow PV cell.” [Online]. Available: <https://www.sterlitech.com/cf042-crossflow-cell-cf042ac.html>.
- [92] “Fisher Scientific Cold Finger Condensers,” *Fisher Scientific*. [Online]. Available: <https://www.fishersci.ca/shop/products/synthware-cold-finger-condensers-drip-tip/p-6666001>.
- [93] “Sigma Aldrich Dry ice trap,” *Sigma Aldrich*. [Online]. Available: <https://www.sigmapel.com/catalog/product/aldrich/z568546?lang=en®ion=CA>.

- [94] “Dry ice trap,” *AliBaba*. [Online]. Available: <https://www.alibaba.com/countrysearch/CN/jacketed-beaker.html>.
- [95] “Peristaltic Pump,” *Fisher Scientific*. [Online]. Available: <https://www.fishersci.ca/shop/products/fisher-scientific-variable-flow-peristaltic-pumps-4/138762#?keyword=true>.
- [96] C.-N. Yeh, K. Raidongia, J. Shao, Q.-H. Yang, and J. Huang, “On the origin of the stability of graphene oxide membranes in water,” *Nature Chemistry*, vol. 7, no. 2, pp. 166–170, Jan. 2015.
- [97] Xianshe Feng and R. Y. M. Huang, “Estimation of activation energy for permeation in pervaporation processes,” *Journal of Membrane Science*, vol. 118, no. 1, pp. 127–131, Sep. 1996.
- [98] S. You, B. Sundqvist, and A. V. Talyzin, “Enormous Lattice Expansion of Hummers Graphite Oxide in Alcohols at Low Temperatures,” *ACS Nano*, vol. 7, no. 2, pp. 1395–1399, Feb. 2013.
- [99] S.-H. Yoon, “Contact Angle,” *OnlineMBR*. [Online]. Available: <http://onlinembr.info/principles/contact-angle/>.
- [100] R. E. Smith, “Surface Energy Data for Nitrocellulose (cellulose nitrate), CAS # 9004-70-0,” p. 1.
- [101] A. Akbari *et al.*, “Large-area graphene-based nanofiltration membranes by shear alignment of discotic nematic liquid crystals of graphene oxide,” *Nature Communications*, vol. 7, p. 10891, Mar. 2016.
- [102] S. Acharya, J. P. Hill, and K. Ariga, “Soft Langmuir-Blodgett Technique for Hard Nanomaterials,” *Advanced Materials*, vol. 21, no. 29, pp. 2959–2981, Aug. 2009.
- [103] L. Xu, “Langmuir Films of Graphene-Based Materials: Towards Large Area Monolayer Deposition.” .